

NO-A179 717

A HIGHLY EXCITED TURBULENT MIXING LAYER(U) TEL-AVIV
UNIV (ISRAEL) DEPT OF FLUID MECHANICS AND HEAT TRANSFER
I WEISBROT ET AL. NOV 84 AE-84-2 AFOSR-TR-87-0546

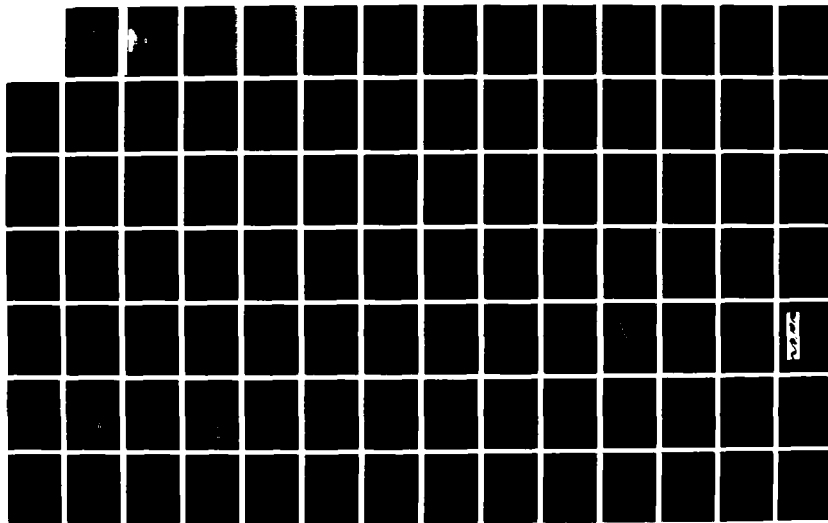
1/2

UNCLASSIFIED

AFOSR-82-0235

F/G 20/4

NL





MI

AD-A179 717

AFOSR Scientific Report

AFOSR 88 - 0235

82

DTIC FILE COPY

4 JAN 1985

(2)

TEL-AVIV UNIVERSITY
Faculty of Engineering
Department of Fluid Mechanics
and Heat Transfer

AFOSR-TN- 87 - 0546

A HIGHLY EXCITED TURBULENT MIXING LAYER

DTIC
ELECTE
S D
APR 27 1987

by

ISRAEL WEIS BROTH

Report AE 84 - 2

Approved for public release;
distribution unlimited.

AIR FORCE OFFICE OF SCIENTIFIC RESEARCH (AFSC)
NOTICE OF TRANSMITTAL TO DTIC
This technical report has been reviewed and is
approved for public release IAW AFR 190-12.
Distribution is unlimited.
MATTHEW J. KERPER
Chief, Technical Information Division

November 84

APPROVED FOR PUBLIC RELEASE; DISTRIBUTION UNLIMITED

87 4 24 048

Unclassified

SECURITY CLASSIFICATION OF THIS PAGE (When Data Entered)

REPORT DOCUMENTATION PAGE		READ INSTRUCTIONS BEFORE COMPLETING FORM
1. REPORT NUMBER AFOSR-TN- 87-0546	2. GOVT ACCESSION NO.	3. RECIPIENT'S CATALOG NUMBER
4. TITLE (and Subtitle) A HIGHLY EXCITED TURBULENT MIXING LAYER		5. TYPE OF REPORT & PERIOD COVERED <i>Final</i>
		6. PERFORMING ORG. REPORT NUMBER
7. AUTHOR(s) I. Weisbrot, I. WYGANSKI, S. EINAV		8. CONTRACT OR GRANT NUMBER(s) AFOSR 82-0235
9. PERFORMING ORGANIZATION NAME AND ADDRESS Tel Aviv University, Ramat Aviv 69978 Dept. of Fluid Mechanics, Israel		10. PROGRAM ELEMENT, PROJECT, TASK AREA & WORK UNIT NUMBERS 61102F 2307 A2
11. CONTROLLING OFFICE NAME AND ADDRESS Air Force Office of Scientific Research Bolling AFB, Washington DC 20330		12. REPORT DATE November 84
		13. NUMBER OF PAGES 116
14. MONITORING AGENCY NAME & ADDRESS (if different from Controlling Office) EOARD/LNV, Box 14 Fpo New York, 09510		15. SECURITY CLASS. (of this report) UNCLASSIFIED
		15a. DECLASSIFICATION/DOWNGRADING SCHEDULE
16. DISTRIBUTION STATEMENT (of this Report) UNCLASSIFIED Unlimited		
17. DISTRIBUTION STATEMENT (of the abstract entered in Block 20, if different from Report)		
18. SUPPLEMENTARY NOTES		
19. KEY WORDS (Continue on reverse side if necessary and identify by block number) Mixing Layer, Hot Wire Anemometry, Turbulence, Stability, Initial conditions Harmonic distortion Pairing		
20. ABSTRACT (Continue on reverse side if necessary and identify by block number) See Reverse Side		

SECTION OF THIS PAGE (When Data Entered)

The flow field in a two-dimensional mixing layer, highly disturbed by a sinusoidally oscillating flap, was mapped. Two velocity components were measured throughout the flow field using a rake of X-wire probes. Streaklines were calculated from the phase-locked measured data, and were compared to smoke pictures, creating a link between flow visualization and experimental results. The phase-locked vorticity field and the Reynolds stresses were calculated from the experimental data.

It was found that fluctuations, locked in phase with the disturbance frequency, were not only responsible for the fast initial growth of the mixing layer but also for its shrinkage further downstream (the occurrence of regions I and II in the parlance of Oster and Wagnanski). The resumption of the growth of the mixing layer further downstream (region III) is no longer controlled by phase-locked oscillations. Although these oscillations still exist in region III they lose energy with increasing distance from the splitter plate. The first subharmonic of the imposed frequency was not detected and the pairing of vortices in regions II or III was not observed.

A comparison was made between the experimental results and calculations based on linear, inviscid stability theory for a slowly diverging plane mixing layer. Good agreement was observed between the cross flow distributions of any predicted quantity and a measured one, however, the theoretically predicted rates of amplification with distance from the splitter plate were higher than the observed ones. The linear theory is, therefore, limited in its ability to model the entire behavior of the disturbed mixing layer.

AFOSR Scientific Report

AFOSR 83 - 0235

82

TEL - AVIV UNIVERSITY
Faculty of Engineering
Department of Fluid Mechanics
and Heat Transfer

A HIGHLY EXCITED TURBULENT MIXING LAYER

by

ISRAEL WEISBROT

Report AE 84 - 2

November 84

APPROVED FOR PUBLIC RELEASE; DISTRIBUTION UNLIMITED

I

ABSTRACT

The flow field in a two-dimensional mixing layer, highly disturbed by a sinusoidally oscillating flap, was mapped. Two velocity components were measured throughout the flow field using a rake of X-wire probes. Streaklines were calculated from the phase-locked measured data, and were compared to smoke pictures, creating a link between flow visualization and experimental results. The phase-locked vorticity field and the Reynolds stresses were calculated from the experimental data.

It was found that fluctuations, locked in phase with the disturbance frequency, were not only responsible for the fast initial growth of the mixing layer but also for its shrinkage further downstream, (the occurrence of regions I and II in the parlance of Oster and Wygnanski). The resumption of the growth of the mixing layer further downstream (region III) is no longer controlled by phase-locked oscillations. Although these oscillations still exist in region III they lose energy with increasing distance from the splitter plate. The first subharmonic of the imposed frequency was not detected and the pairing of vortices in regions II or III was not observed.

A comparison was made between the experimental results and calculations based on linear, inviscid stability theory for a slowly diverging plane mixing layer. Good agreement was observed between the cross flow distributions of any predicted quantity and a measured one, however, the theoretically predicted rates of amplification with distance from the splitter

II

plate were higher than the observed ones. The linear theory is, therefore, limited in its ability to model the entire behavior of the disturbed mixing layer. (Direct)

Accession For	
NTIS CRA&I	<input checked="" type="checkbox"/>
DTIC TAB	<input type="checkbox"/>
Unannounced	<input type="checkbox"/>
Justification	
By	
Distribution/	
Availability Codes	
Dist	Avail and/or special
A-1	

QUALITY
INSPECTED
2

IV

CONTENTS

	Page
ABSTRACT	I
ACKNOWLEDGEMENTS	III
CONTENTS	IV
NOMENCLATURE	1
CHAPTER 1: INTRODUCTION	4
CHAPTER 2: THE EXPERIMENTAL FACILITIES AND EQUIPMENT	10
CHAPTER 3: THE CALIBRATION METHOD	14
CHAPTER 4: DATA ACQUISITION AND NUMERICAL CALCULATIONS	16
4.1 Phase-locked averaged velocity components	17
4.2 Reynolds stress	19
4.3 Energy production	20
4.4 Vorticity field	21
4.5 Streaklines	22
CHAPTER 5: THE DISTURBED MIXING LAYER	26
5.1 Mean flow parameters	26
5.2 Streaklines and vorticity distribution	28
5.3 The intensity of the fluctuations, the Reynolds stress and their respective spectral distributions	31
5.3.1 Region I	32
5.3.2 The first transition region	33
5.3.3 Region II	34

V

5.3.4	The second transition region	36
5.3.5	Region III	
		37
5.3.6	The subharmonic frequency	38
CHAPTER 6: A DETAILED COMPARISON WITH THE LINEAR INVISCID STABILITY THEORY		40
CHAPTER 7: CONCLUDING REMARKS		48
REFERENCES		50
LIST OF FIGURES		52
FIGURES		

NOMENCLATURE

A	Amplitude of the complex stream function.
b	Width of the mixing-layer ; $b \approx Y_{0.95} - Y_{0.10}$.
d	The diameter of the hot wire .
E_1	output voltage of the anemometer, operating wire #1 of an X-wire probe .
E_2	output voltage of the anemometer, operating wire #2 of an X-wire probe .
F	Frequency .
f	Forcing frequency in Hz .
L	Scaling factor for the lateral dimensionless coordinate .
l	The length of the hot wire .
NPP	Number of data points per period of the disturbance .
Q	Magnitude of the velocity vector .
R	Position vector of a particle at $t=0$.
r	Position vector of a particle .
r_0	Position vector of a source point .
S_u^2	Power spectrum of the longitudinal velocity component .
S_{uv}	Cross spectrum of the two velocity components .
S_v^2	Power spectrum of the lateral velocity component .
T	Time period of the disturbance frequency .
t	Time .
t_0	Initial time .
\bar{U}	The mean velocity component in the streamwise direction.
U_1	Free stream velocity on the low velocity side .
U_2	Free stream velocity on the high velocity side .
U_c	Convection velocity of the large eddies. $U_c \equiv (U_2 + U_1)/2$.

u	Instantaneous streamwise velocity component .
$\langle u \rangle$	Phase-locked streamwise velocity component .
u'	Velocity fluctuations in the streamwise direction .
u'_f	Velocity fluctuations in the streamwise direction at the excitation frequency .
u'_{2f}	Velocity fluctuations in the streamwise direction at the harmonic frequency .
\bar{v}	The mean velocity component in the lateral direction .
v	Instantaneous lateral velocity component .
$\langle v \rangle$	Phase-locked lateral velocity component .
v'	Velocity fluctuations in the lateral direction .
v'_f	Velocity fluctuations in the lateral direction at the excitation frequency .
X	Streamwise direction in a cartesian coordinate system .
X_0	Virtual origin of the mixing-layer .
Y	Lateral direction in a cartesian coordinate system .
Y_0	The Y location corresponding to $\bar{U}=0.5(U_2+U_1)$.
$Y_{0.10}$	The Y location corresponding to $\bar{U}-U_1=0.10(U_2-U_1)$.
$Y_{0.50}$	$= Y_0$.
$Y_{0.95}$	The Y location corresponding to $\bar{U}-U_1=0.95(U_2-U_1)$.

Greek letters

α	Yaw angle of the hot wire probe .
γ	Inclination angle of a vortex .
λ	Wave length of the disturbance $\lambda = \frac{U}{f} c$.
Δt	Time interval between samples .
δ_w	Maximum slope thickness : $\delta_w \equiv (U_2 - U_1) \cdot (dU/dY)_{\max}$.
η	Dimensionless lateral coordinate .

Φ	Complex stream eigenfunction .
Φ_0	Initial phase for phase-locked averaging .
Ω	Spanwise vorticity component .
$\langle \Omega \rangle$	Phase-locked spanwise vorticity component .
ω	Frequency in rad/sec .
ω_0	Disturbance frequency in rad/sec : $\omega_0 = 2\pi f$.
Ψ	Complex stream function .
$\bar{\Psi}$	Complex mean stream function .
ρ	Density .
θ	Momentum thickness .
θ_t	Theoretical momentum thickness .
τ	Reynolds stress : $\tau \equiv -\rho \overline{u'v'}$.
$\langle \tau \rangle$	Phase-locked Reynolds stress : $\langle \tau \rangle \equiv -\rho \langle \overline{u'v'} \rangle$.
ξ	Dimensionless coordinate in the direction of streaming .

CHAPTER 1

INTRODUCTION

The turbulent mixing layer between two uniform coflowing streams having a different velocity (Fig. 1.1) has been the subject of many investigations over the past few decades. The vast interest in this simple configuration is undoubtedly triggered by the numerous natural phenomena with which it can be associated and its wide range of applications.

Two approaches are currently used to study turbulent shear flows of this kind. The classical approach views turbulence as a random process which can only be adequately described statistically. The other approach looks for quasi-deterministic vortex structures which are considered to be the main building blocks of such flows. The adoption of the latter approach in the investigation of the two dimensional mixing layer was stimulated by flow visualization experiments of Brown & Roshko (1971,1974) who discovered the presence of large coherent structures in the turbulent mixing layer between two inert gases. Winant & Browand (1974) observed a merger between pairs of adjacent eddy structures to which they attributed the lateral growth of the turbulent mixing layer. This "pairing process" occurs randomly in space and time (Roshko 1976) generating, on the average, a smooth, linearly growing mixing layer. It is now generally accepted that the large eddies play a major role in the growth of the mixing layer by influencing the entrainment process; by amalgamating; and by a mutual destruc-

tion referred to as "tearing" (Dimotakis & Brown 1976).

Reservations regarding the two-dimensionality of the large eddies and their indefinite persistence may, however, still exist. Chandrsuda et al. (1978) suggest, that the two-dimensional eddies represent a relic of the transition process, while the fully developed turbulent flow is highly three-dimensional. They argued that natural transition does not occur whenever the level of the free stream turbulence is high and therefore, large coherent structures can only appear under ideal laboratory conditions. Pui & Garthshore (1979) associated the periodic behaviour of the large eddies with vibrations of the apparatus. The structures observed by them were not even moderately two-dimensional. Wygnanski et al. (1979) introduced strong external disturbances into each of the streams ($u'/U = 3\%$) and found quasi two-dimensional large eddy structures forming irrespectively of the high turbulence level existing in the free streams. Breidenthal (1980) disturbed the flow in the spanwise direction by using a specially designed splitter plate and found that the shear layer quickly forgets the those perturbations and forms the characteristic two-dimensional vortex structures. Nevertheless, streamwise vortices which appear to scale with the spanwise vortices persist under some conditions. (Roshko, private communication)

Observations showing the influence of periodic, two-dimensional excitation on the mixing layer were reported by Oster et al. (1978) and later by Oster & Wygnanski (1982). The rate of growth of the shear layer was significantly altered by the excitation even when the amplitude of the

latter was small. Ho & Huang (1980, 1982) excited the laminar mixing layer at various frequencies and showed that adjacent vortices can either pair with one another or "collective interact". Vortex amalgamations were artificially stimulated by these investigators who prompted the coalescence of any small number, N , of vortices by disturbing the flow with the N^{th} subharmonic of the initially most amplified frequency.

Statistical theories in which the turbulence was considered to be a random process were always impeded by the fact that the number of unknowns exceeded the number of equations. One had to resort to models (e.g. eddy viscosity, mixing length, turbulent rate equation, a relation between Reynolds stress and turbulent intensity etc.) to provide the additional equation required for the solution. The discovery of large coherent structures suggest new ways of averaging and entirely different approaches to modeling. The mixing layer is sometimes replaced by an array of vortices evolving in time (Corcos & Sherman (1976), Acton (1976), Ashurst (1976), Patnaik, Sherman & Corcos (1976), Corcos & Sherman (1984), Corcos & Lin (1984) and Lin & Corcos (1984), to name a few).

With the increased availability of large computers numerical solutions of the equations of motion became feasible using an ever decreasing number of constraints. Large eddy simulations were applied, among others, by Riley & Metcalfe (1980). They found that the presence of the subharmonic frequency which is not in phase with the most unstable linear eigenmode, causes the vortices to pair. Riley & Metcalfe suggested a plausible explanation for some of the observations of Oster et al. (1978) in particular

the discontinuity in the rate of growth of the mixing layer which was accompanied by the appearance of negative Reynolds stresses. They explained the effect by eliminating the subharmonic frequency from their calculations which resulted in the reduction of the turbulent kinetic energy and a concomitant slow-down in the lateral rate of spread of the flow. It was suggested that the elimination of the subharmonic inhibited or even eliminated the pairing process.

Inoue (1983) simulated vortex pairing in turbulent mixing layers by a discrete vortex method. He found two stages in the development of the mixing layer: a stage of clustering where numerous vortices interact with one another and form discrete lumps followed by a pairing stage in which the lumps amalgamated. Inoue compared his calculations with experiment and found reasonable qualitative agreement with available data.

The evolution of the large eddies can also be predicted from hydrodynamic stability theory. In laminar flows, where the mean velocity profile represents the solution of the equations of motion, one may determine the character of the disturbances resulting from the instability of the flow field. Such an analysis was done by Michalke (1964, 1965) who predicted the temporal and spatial growth of perturbations in an inviscid two-dimensional mixing layer. The mean velocity profile for which calculations were performed was represented by a hyperbolic-tangent function. Monkevitz and Huerre (1982) compared the stability of the "tanh" profile with the profile resulting from the solution of the boundary layer equations while studying the influence of the velocity ratio on the spatial

instability of mixing layers. They found that the maximum amplification rate of the perturbation is approximately proportional to the parameter $(U_2 - U_1)/(U_2 + U_1)$ while the shape of the velocity profile was less important.

The application of the stability theory to turbulent flows is not straightforward because there is no steady velocity field in existence upon which a perturbation may be superimposed. One tends to select the mean velocity profile as being representative on the average recognizing the possibility that at any instant in time the actual flow field may be quite different. Nevertheless, knowing that the random changes in the mean velocity occur on a time scale which is short in comparison with the period associated with the large coherent structures and assuming that the kinetic energy exchange between largely disparate scales is negligible, Gaster Kit & Wygnanski (to appear in J.F.M) applied the inviscid linear stability theory with a large measure of success. They modelled the development of normal modes in a slowly divergent turbulent mixing layer by expanding the inviscid equations in multiple-scales in a way similar to the one used by Bouthier (1972) and by Crighton & Gaster (1976). The streamwise velocity component of the computed eigenfunctions agreed well with experiment but the quantitative comparison of the growth rates was poor.

One of the aims of the present work was to extend this comparison to the lateral velocity component, the phase-locked $u'v'$ product and the spanwise vorticity distributions and to determine the limitations of the linear approach by applying relatively high-amplitude disturbances to the flow.

Furthermore, most of the observations related to large coherent structures are based on flow visualization. In some instances the method of visualization represents local conditions (shadowgraph, laser induced fluorescence, chemical reaction etc.) in others it is based on the interpretation of streaklines (hydrogen bubbles, smoke or dye filament etc.). The often used streakline method may be misleading because a congregation of marked particles in one location in the flow may be the outcome of cumulative forces acting over a large distance and may not necessarily represent a local event of dynamical significance. The dynamical significance of vortex pairing is, for the time being, unknown. We therefore tried to calculate streaklines from phase-locked velocity measurements; if the evaluated streaklines agree with those observed by marking fluid particles then the same data can be used for the evaluation of phase-locked vorticity, $u'v'$ product and any other quantity of significance. Therefore, a second aim of the present investigation was to develop a tool which does not rely on qualitative interpretation of marked particles.

CHAPTER 2

THE EXPERIMENTAL FACILITIES AND EQUIPMENT

The mixing layer facility in Tel-Aviv University consists of two independent cascade blower wind tunnels discharging into a common test section (Fig. 2.1). The two tunnels which are a mirror image of one another, are separated initially by a splitter plate which extends upstream through the contraction section and into the settling chamber. The splitter plate ends 20 cms. downstream of the contraction allowing the two streams to become parallel before the initiation of the mixing. The trailing edge of the splitter plate was milled at an included angle of 3° .

Each tunnel consists of an air-supply system, a diffuser, a settling chamber and a nozzle. The air is supplied to each tunnel by a backward facing step blower driven by a separate D.C. motor. One of the motors has a power rating of 15 KW and is manufactured by Elektromotoren Werke Karl-kaiser (Typ GV 132.24S), it is controlled by a DFVLR DMR II digital controller. The other motor is a 5 HP "Kinematic" D.C. motor, controlled by a General Electric "Thymotrol" control system, equipped with a tachometer generator. The air speed of the lower stream can change continuously between 0-13.5 m/sec and in the upper stream between 0-9 m/sec. The two independent blowers enable one to work at any velocity ratio desired, over a wide range of velocities. The blowers were vibration-isolated from the rest of the structure and equipped with filters at their inlet. A small

settling chamber and a gauze are situated between the blower and the diffuser in order to provide resistance and equalize spatially the flow entering the diffuser.

Each diffuser is subdivided into four smaller channels having an equivalent cone angle, that does not exceed 5° . A deep cell honeycomb and 3 turbulence damping screens are installed in the settling chamber. The contraction ratio of each nozzle is 7.3:1 and a representative turbulence level at the exits was measured to be 0.40% in the upper tunnel at 3 m/sec, and 0.27% in the lower tunnel at 5 m/sec.

The test section is 2000 mm long, 500 mm high and 600 mm wide. The side walls which are made of transparent plexiglass sheets are removable for photographic purposes (i.e. avoiding reflections). The top and bottom walls are made of flexible P.V.C. sheets mounted on screw jacks, enabling one to control the streamwise pressure gradient.

The traversing mechanism supporting the measuring sensors has three degrees of freedom:

- a) Translation in the streamwise direction (X-axis), performed manually by a sliding wheel-cart with a resolution of 1 mm.
- b) Translation in the vertical direction (Y-axis), performed by a lead screw having a 4 mm pitch.
- c) Rotation around the Y-axis, performed by a shaft passing through a hollow column of a symmetric airfoil.

Both the lead screw and the shaft are activated by separate Slo-Syn M063FDU6 stepping-motors, having an angular resolution of 1.8° per step, equivalent to translational resolution of 0.02 mm. The stepping-motor rotating the probes about the Y axis is connected to the shaft through a gear having a reduction ratio of 10:1, therefore increasing the angular resolution up to 0.18° .

Both stepping-motors are controlled by a Kapac Electronics 2-axes PSM 151B controller, equipped with manually and externally triggered modes. The external operation mode enables us to computer-control the movements.

A thin flap pivoted at its leading edge generated the required perturbations. The flap is 10 mm and 0.5 mm thick and it spans the entire test section along the trailing edge of the splitter plate. The gap between the splitter plate and the flap was sealed by an adhesive tape. The sinusoidal oscillations were provided by two voice coils connected in parallel, activated by a Krohn-Hyte 5100A function Generator, insuring full control over the frequency and amplitude of the fluctuations. The signal was amplified by a 40 watt Dynaco Stereo 80 power-amplifier. The sine-wave signal was simultaneously processed by a home-made frequency-dividing circuit, creating a synchronized square-wave subharmonic signal used as a trigger-source for the data acquisition process. A rake of 7 X-wires operated at a constant temperature mode was used throughout the investigation. Each wire is made of Tungstan, 5 micron in diameter, welded to a pair of prongs 1 mm apart, creating an angle of 45° with the axis of the probe. The length to diameter ratio of each wire is $l/d = 280$ and the frequency response, as determined

by a square wave method, was approximately 10 KHz. The multi-channel constant temperature anemometers were designed and constructed in the electronics workshop of the Faculty of Engineering in Tel Aviv University. The over-heat ratio was set to be 1.5.

CHAPTER 3

THE CALIBRATION METHOD

The calibration method for an array of X-wire probes described below is only possible with the aid of a computer.

It is assumed that the output voltage of each wire in the X-probe is a function of the modulus of the velocity vector Q and the angle this vector makes with the axis of the probe α :

$$E_1 = E_1(Q, \alpha) \quad \text{and} \quad E_2 = E_2(Q, \alpha).$$

It is also assumed that within the range of calibration, the opposite is also true: for each pair of Q and α , only one pair of voltages is possible, or that a given pair of voltages E_1 and E_2 , determines the velocity uniquely.

$$Q = Q(E_1, E_2) \quad \text{and} \quad \alpha = \alpha(E_1, E_2).$$

The functions Q and α are assumed to be forth-order, two-dimensional polynomials of the form:

$$Q = A_1 E_1^4 + A_2 E_2^4 + A_3 E_1^3 E_2 + A_4 E_1^2 E_2^2 + \dots + A_{15}$$

and a similar expression for α . In order to determine the 15 coefficients for each polynomial, a two-dimensional Least Square Fit (LSFP) procedure was employed. Measurements of the mean voltages E_1 and E_2 were taken at 7 different air velocities and 11 different yaw angles, between $-27^\circ < \alpha < 27^\circ$,

for each velocity. Hence, 77 different pairs of E_1 and E_2 formed the basis for the LSFP procedure.

The operation of the calibration procedure was almost fully computer-controlled. The digital output channel of the computer was used as a trigger-source for activating the stepping-motor controller rotating the probe holder and changing its yaw angle. Data acquisition started right after the movement was completed. The whole calibration procedure, for a rake of 7 X-wire probes, lasted no longer than 5 minutes.

CHAPTER 4

DATA ACQUISITION AND NUMERICAL CALCULATIONS

Data acquisition and numerical analysis were performed on a PDP 11/60 minicomputer equipped with an analog to digital converter which is a part of the LPA11 system. The computer has a total memory of 128K words and is operated by a RSX-11M operating system (version 3.2). The computer is also equipped with two Digital RK07 disc drivers and two Kennedy, Model 9300, magnetic tape drives. The tape drives were used to record in real time the output voltages of the hot-wire anemometers and amplifiers. Since no digital processing was carried out during data acquisition, the experiment was shortened significantly.

The A/D converter resolution is 2.44 millivolts per digit. The sampling frequency was 2.048 KHz per channel and since all 16 A/D channels were occupied (14 hot wire channels + disturbance channel + subharmonic square-wave channel), the sampling frequency of the computer was 32.768 KHz, far below its 80 KHz limitation.

The first step in the numerical computations was to translate the voltages, recorded on the magnetic tape during data acquisition, to the two velocity components, using the calibration coefficients. This procedure produced the instantaneous values of Q and α , and the velocity components u and v were calculated from the following relations:

$$u = Q\cos(\alpha) \quad \text{and} \quad v = Q\sin(\alpha)$$

4.1. Phase-locked averaged velocity components

The phase-locked averaged velocity vectors were calculated from the sampled velocity vectors in order to analyze the periodic flow phenomena having the disturbance frequency, or its first subharmonic.

The numerical representation of the phase-locked averaged signal is:

$\langle u(j) \rangle = \frac{1}{N} \sum_{i=1}^N u(\phi_0 + (j-1)\Delta t + i*NPP)$; Where u is the original vector containing the velocity values sampled;

Δt is the time interval between data points;

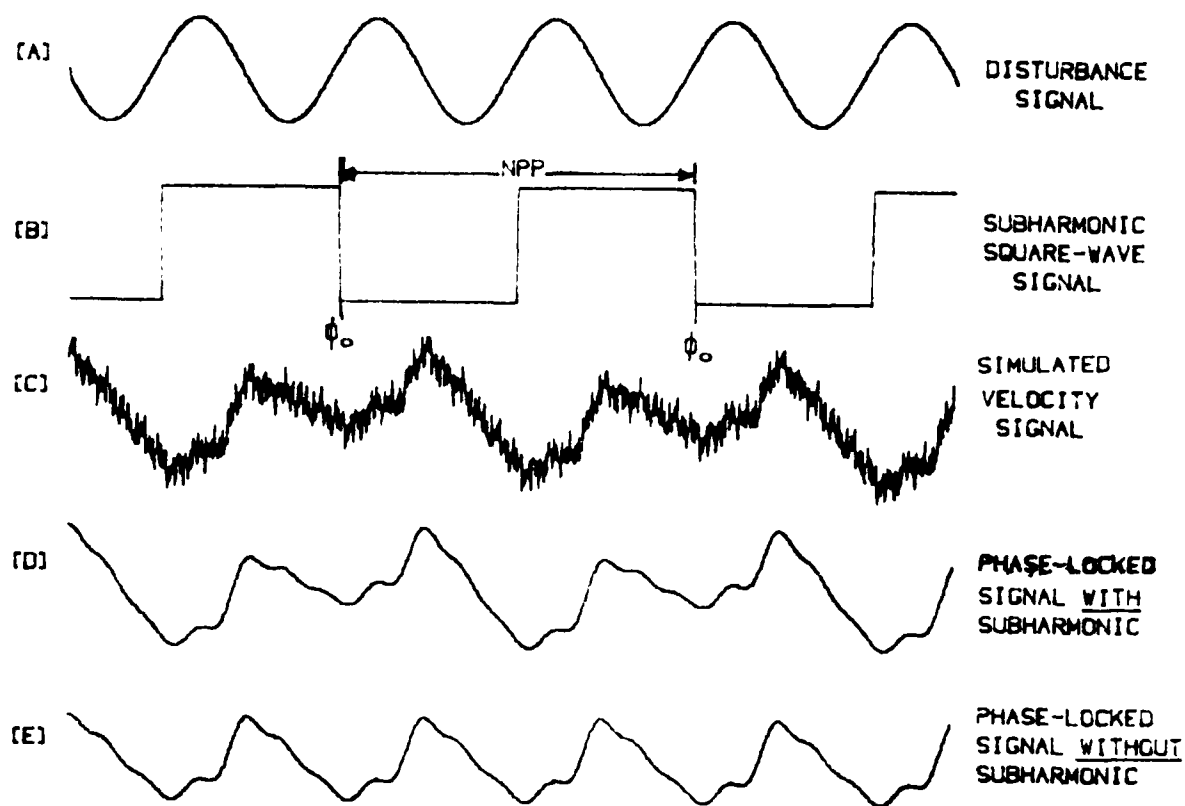
NPP is the number of data points per period (T) of the frequency analyzed (i.e. $NPP = T/\Delta t$);

ϕ_0 is an arbitrary initial phase;

and N is the number of time-periods of the analyzed frequency contained within the original velocity vector.

The determination of ϕ_0 and NPP required the simultaneous sampling and recording of both the sine-wave signal activating the flap, and its first subharmonic signal, produced by the electronic frequency-dividing circuit, designed to produce a synchronized square-wave signal.

The sketch below illustrates the phase-locked averaging method.



The initial phase points ϕ_0 corresponds to a point at which the square-wave crosses zero with a negative slope; NPP was calculated as the mean number of data points between two adjacent initial-phase points (trace [B]).

The result of an averaging process of a signal [C] dominated by a certain frequency (a fundamental frequency) which is phase-locked with its first subharmonic, is a signal [D] containing two consecutive waves of the fundamental superimposed on the subharmonic. All the random high frequency influence (turbulent behaviour) is filtered out. By averaging with respect to the fundamental only one obtains trace [E]. Trace [E] is also obtained whenever the two frequencies (i.e. the fundamental and its subhar-

monic) are not locked in phase.

The length of each sampled velocity vector was 512 points (equivalent to a period of 0.25 sec), and 100 such vectors were acquired. Thus, the average phase-locked to the subharmonic frequency was calculated from 400 events.

Other flow parameters, such as the mean velocity profiles, the R.M.S. values, the Reynolds stresses and the spectra, were calculated from the original time series.

4.2. Reynolds stress

Three different ways of averaging the $-\bar{u}^{\prime}\bar{v}^{\prime}$ product were employed:

a) The Reynolds stress is a temporally averaged product of the two time dependent velocity vectors:

$$\tau(X,Y) = -\rho(u'(X,Y,t)*v'(X,Y,t))$$

where: $u'(X,Y,t)=u(X,Y,t)-\bar{U}(X,Y)$

$$v'(X,Y,t)=v(X,Y,t)-\bar{V}(X,Y)$$

b) The phase-locked ensemble-averaged $-\langle\bar{u}^{\prime}\bar{v}^{\prime}\rangle$ product, producing a value containing the influence of all frequencies which are locked in the phase to the excitation:

$$\langle\tau\rangle = -\rho\langle\bar{u}^{\prime}\bar{v}^{\prime}\rangle$$

c) The spectrum of the Reynolds stress. In order to obtain both the power spectra and the spectra of the $u'v'$ product, we have used a fast Fourier transform operator (FFT). The result was a vector containing both the real and imaginary coefficients of various frequencies for each velocity component.

$$\mathcal{L}(u) = C_1(F) \quad \text{where} \quad C_1(j) = A_1(j) + iB_1(j)$$

$$\mathcal{L}(v) = C_2(F) \quad \text{where} \quad C_2(j) = A_2(j) + iB_2(j)$$

where $A(j)$ and $B(j)$ are the sine and the cosine coefficients of the j^{th} frequency, respectively. The sampling frequency (2.048 KHz), and the length of the vector containing the velocity signal (512 data points), define the lowest frequency measured, and the spectral resolution to be equal to 4 Hz, and the highest frequency to be equal to 1.024 KHz.

The power spectra were calculated by multiplying each of the coefficients in $C_1(F)$ by its complex conjugate $C_1^*(F)$;

$$Su^2(F) = C_1(F) * C_1^*(F) \quad \text{where} \quad Su^2(j) = A_1(j)^2 + B_1(j)^2$$

The Reynolds stress spectra were calculated from the real part of the cross-spectrum of the two velocity signals, i.e. the product of one velocity component with the complex conjugate of the other velocity component:

$$Suv(F) = 0.5 \text{ REAL}[C_1(F) * C_2^*(F)]$$

where

$$Suv(j) = -0.5[A_1(j) * A_2(j) + B_1(j) * B_2(j)].$$

4.3. Energy production

The overall energy production term defined by $-\bar{u}^{\overline{\overline{x}}} \bar{v}^{\overline{\overline{y}}} \frac{d\bar{u}}{dy}$ can be divided

into the phase-locked (or coherent) energy production which is responsible for energy transfer from the mean flow to the phase-locked fluctuations, and the random (or turbulent) energy production. The overall energy production terms were computed by multiplying the mean $-\bar{u}^{\prime}\bar{v}^{\prime}$ product with the local mean velocity gradient, and the phase-locked energy production was calculated applying the same procedure to the phase-locked $-\langle\bar{u}^{\prime}\bar{v}^{\prime}\rangle$ product. The mean velocity profile employed was a modified hyperbolic tangent profile, fitted to the experimental data (for details see chapter 6).

In addition, we have calculated the local integrals of the overall and phase-locked energy production over the cross-section of the flow,

i.e. $\int_{-\infty}^{\infty} (-\bar{u}^{\prime}\bar{v}^{\prime}) \frac{d\bar{U}}{dy} dy$ and $\int_{-\infty}^{\infty} (\langle -\bar{u}^{\prime}\bar{v}^{\prime} \rangle) \frac{d\bar{U}}{dy} dy$, respectively.

4.4. Vorticity field

The phase-locked averaged spanwise vorticity field was computed by numerical differentiation of the phase-locked averaged velocity vectors.

The resulting phase-locked averaged vorticity signal $\langle \omega(X,Y,t) \rangle$ was used, both for plotting the isodynes (isovorticity contours) and for further mathematical operations (i.e. Fourier transformation at the disturbance frequency in order to obtain the vorticity eigenfunctions and compare them with the results of the stability theory).

4.5. Streaklines

A streakline connects, by definition, all fluid particles that have passed through a fixed point in space (a source point), during a given period of time.

In order to establish and draw a streakline from the velocity vectors given in the Eulerian representation, one must transfer it to the Lagrangian representation, i.e. calculate pathlines given by:

$$\mathbf{r} = \mathbf{r}(\mathbf{R}, t)$$

where \mathbf{R} is the position vector of the particle at $t=0$.

Providing the Jacobian of the matrix of the given system of equations has a non-zero value, the following relation can be written:

$$\mathbf{R} = \mathbf{R}(\mathbf{r}, t)$$

A streakline at a given time t^* can be directly calculated by the following expression:

$$\mathbf{r} = \mathbf{r}[\mathbf{R}(\mathbf{r}_0, t_0), t^*]$$

where \mathbf{r}_0 is the position vector of a source point;

t^* is a parameter defining the time at which the streakline is to be plotted;

and t_0 is the time variable $0 < t_0 < t^*$.

Another way of representing a pathline, in a two-dimensional flow field, is:

$$u=dX/dt \quad ; \quad v=dY/dt$$

with $X(t=t_0)=X_0$ and $Y(t=t_0)=Y_0$. X_0 and Y_0 are the space coordinates of a source-point.

We restricted our discussion to a row of source-points, displaced vertically at the first measuring X-location ($X=200$ mm). Thus we can represent the pathlines as :

$$r_1 = r_1(r_0, t_0, t)$$

where r_0 is the position vector of the source-points;

t_0 is the initial time parameter

and t is the time variable.

Since the flow field considered is periodic, with a period T , it follows that:

$$r_1(r_0, t_0, t) = r_1(r_0, t_0 + nT, t) \quad n=1, 2, \dots$$

The pathlines were calculated by numerical integration of the phase-locked averaged velocity vectors.

Each source point r_0 produced NPP pathlines (i.e. the number of data points in the phase-locked averaged velocity vector). The pathline vectors were identified by an index j defined as $j=1+t_0/\Delta t$ where t_0 is the time the particle passed through the source point and Δt is the time interval between data points.

Since Δt is determined by the sampling frequency the integration led us to space coordinates, other than our measuring locations. Interpolation

techniques were employed in order to establish the velocity values at those points. A spline interpolation procedure was first used in the transverse direction (Y- axis), and a linear interpolation method was then applied in the streamwise direction (X-axis). Since the period T corresponds to NPP data points, all time considerations reduce to a proper indexing of the points in the phase-locked averaged velocity vectors.

The function r_1 describes the position of all particles that had passed through a source point. Writing :

$$r_1 = r_1(r_0, t_0, t^*)$$

where r_0 and t^* are now the parameters of the source position and the plotting time, respectively, and t_0 is the variable, ($0 < t_0 < t^*$), we thus represent the desired streaklines. The periodic flow field demands that:

$$r_1(r_0, t_0, t^*) = r_1(r_0, t_0, t^* + nT) \quad n=1, 2, \dots$$

Thus, the computation of streaklines is reduced to a selection procedure of data points from the pathlines.

If, for example, the streakline at the time corresponding to the i^{th} point of the phase-locked averaged vector is to be plotted (i.e. $t^* = i \Delta t$), the following points are to be picked up from the pathline vector indexed $j=1$:

$$i^{\text{th}}, (NPP+1)^{\text{th}}, (2*NPP+1)^{\text{th}}, \dots, (n*NPP+1)^{\text{th}},$$

from the pathline indexed $j=2$ the following points are to be picked up:

$$(i-1)^{\text{th}}, (NPP+i-1)^{\text{th}}, (2*NPP+i-1)^{\text{th}}, \dots, (n*NPP+i-1)^{\text{th}},$$

from the pathline indexed $j=j$ the following points are to be picked up:

$$(i-j+1)^{\text{th}}, (NPP+i-j+1)^{\text{th}}, (2*NPP+i-j+1)^{\text{th}}, \dots, (n*NPP+i-j+1)^{\text{th}},$$

and from the pathline indexed $j=1$:

$1^{st}, N_{pp}^{th}, 2*N_{pp}^{th}, \dots, n*N_{pp}^{th},$

etc.

CHAPTER 5

THE DISTURBED MIXING LAYER

5.1. Mean flow parameters

"By introducing a periodic disturbance to the mixing layer, one can change dramatically the mean velocity, as well as the turbulent properties of the flow" (Oster and Wagnanski 1982).

The velocity ratio between the two streams in the present experiment was maintained at 0.6, the velocity of the slower stream was $U_1=6$ m/sec and the velocity of the faster stream was $U_2=10$ m/sec. The flow was disturbed by a flap oscillating at the frequency of $f=44.5$ Hz, and an amplitude of 1.5 mm. At each cross section the mean velocity profile was measured, and from it the mixing layer width, b , was estimated as follows:

$$b=(Y_{0.95}-Y_{0.10})$$

where $Y_{0.95}$ and $Y_{0.10}$ are the lateral coordinates at which $(\bar{U}-U_1)/(U_2-U_1)=0.95$ and 0.10 respectively. The momentum thickness θ :

$$\theta=(U_2-U_1)^{-2} \int_0^{\infty} (U_2-\bar{U})(\bar{U}-U_1) dY$$

was also computed. Both quantities are plotted against the streamwise coordinate X in Fig. 5.1.1. The dimensional streamwise coordinate X is presented to avoid ambiguity resulting from the dependence of θ on X . $Y_{0.95}$, $Y_{0.50}$ and $Y_{0.10}$ are plotted against X in Fig. 5.1.2. A dense grid of data points (80 in the streamwise direction) was necessary to achieve

sufficient resolution for the calculation of streaklines. Unlike the undisturbed mixing layer, the excited mixing layer does not spread linearly with X . Three distinct regions can be recognized in this case :

Region I, ($X < 560$ mm), in which the momentum thickness grows with increasing distance from the splitter plate. Part of region I ($X < 500$ mm) is characterized by a linear growth of the momentum thickness with a slope of $d\theta/dX = 0.0265$.

Region II, ($560 < X < 840$ mm), in which the width of the mixing layer actually decreases.

Region III, ($X > 840$ mm), in which the mixing layer resumes its linear growth, but at a slower rate ($d\theta/dX = 0.0071$).

Two transition subregions, discussed later, separate these clearly defined regions. This behaviour is characteristic of a strongly disturbed mixing layer (Oster and Wygnanski 1982).

The mean velocity profiles scaled by the momentum thickness are similar in both regions I and III. The actual shape of the profiles changes from region to region, particularly on the low-speed side of the flow (Fig. 5.1.3) where $(\frac{1}{\theta} \frac{d\bar{U}}{dY})_{\text{region I}} > (\frac{1}{\theta} \frac{d\bar{U}}{dY})_{\text{region III}}$. The difference in the shape of the mean velocity profiles can not be attributed to an error and must stem from the dynamics of the energy containing eddies. It should be noted that some definitions of mixing layer width such as the maximum-slope (or vorticity) thickness $\delta_w = (U_2 - U_1) / (dU/dY)_{\text{max}}$ used by Brown and Roshko (1974), are not sensitive to these variations in the shape of the mean velocity profiles.

5.2. Streaklines and vorticity distribution

One of the main objectives of this work was to compare streaklines computed from phase-locked components of measured velocity, with conventional flow visualization techniques. Such a comparison could provide a link between qualitative observations and quantitative data and may serve as a tool for analyzing the dynamic significance of the pairing of vortices, observed visually by Winant and Browand (1974).

A comparison between a streakline pattern and a smoke picture is presented in Fig. 5.2.1, and the resemblance between the two is obvious. In order to take the photograph, a smoke-filament was introduced near the trailing edge of the splitter-plate, while the test-section was illuminated by a stroboscope synchronized with the frequency of the flap. The exposure time was 0.8 seconds and, therefore, the photograph represents a phase-locked superposition of 36 events. The data used for calculating streaklines was also used for calculating the velocity and vorticity fields, the distribution of Reynolds stresses, the transfer of energy from the mean motion and the scales of the large coherent structures. The corresponding phase-locked vorticity field is also presented in this figure.

A pattern of 4 streaklines, each originating from a different source-point, vertically displaced at the first measuring-station ($X=200$ mm) is shown at the top of Fig. 5.2.2, while the corresponding phase-locked vorticity field, described by isodynes (iso-vorticity contours), is presented at the bottom. Each lumpy structure coincides with a

concentration of vorticity and, therefore, is loosely referred to as a vortex.

The three regions discussed in conjunction with the spreading rates of the shear layer can also be distinguished by the manner in which vorticity is distributed. Vorticity in region I is concentrated in two cores, displaced both longitudinally and laterally (Fig. 5.2.3(b)). The longitudinal displacement of these cores diminishes with increasing distance downstream, until it vanishes at the beginning of region II, forming a circular lump. This description agrees with predictions based on 'inviscid linear stability theory and will be discussed later in this work.

Region I, which is marked by a rapid growth of the shear layer, can be characterized by the amplification of disturbances in the lateral direction. Its length is equal to the distance required for the vortex sheet to roll into a lump. A lump is formed at a cross section at which the streakline pattern folds over backwards. Fig. 5.2.3(a) describes streaklines in region I.

The lateral dimension of the vortex lumps in region II remains unchanged (Fig. 5.2.4(a)) , but their inclination to the flow axis is altered; it crosses the vertical inclination angle $\pi/2$ at the beginning of region II (Fig. 5.2.3(a)). The thin vortex sheet which separates adjacent lumps, and sometimes is referred to as the "braid", is stretched in the process, as can be seen from the calculated streaklines. The spatial resolution of the measurements may be insufficient to detect the vorticity

associated with the braid. Each vortex in region II appears to contain a single core (Fig. 5.2.4(b)), as predicted by linear stability analysis.

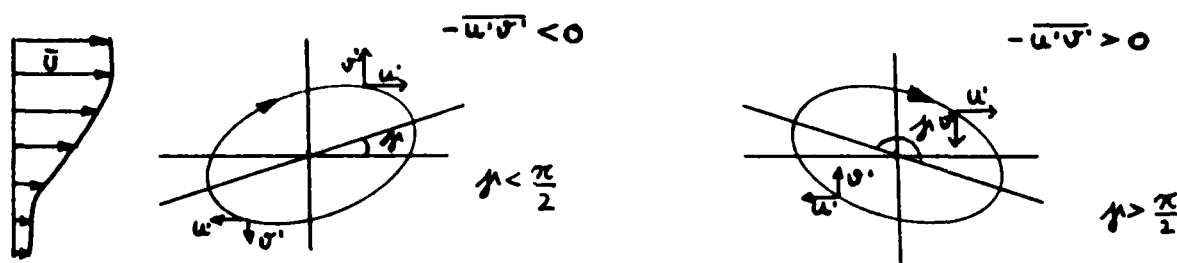
The vortex lumps in region III are leaning downstream on the high velocity side of the shear layer (upper-stream side of Fig. 5.2.5(a)), their inclination angle to the axis of the flow continuously decreases with increasing distance from the splitter plate. The elongation of the vortex lumps and the change in their inclination angle causes one lump to overlap another. It seems that a second vorticity core reappears in the interior of each vortex (Fig. 5.2.5(b)) in region III.

Neither the phase-locked streaklines nor the photographs produced by stroboscopic illumination show the existence of pairing. Therefore one must conclude that pairing, if it exists, is not locked in phase to the excitation fluctuations and it does not occur very often in a forced mixing layer.

Fig. 5.2.6 shows a sequence of streaklines plotted at time intervals equivalent to $1/4$ period of the forced oscillations between them. One can therefore observe the temporal development in the inclination angle of the structures while moving from region I to region II and the stretching of the structures in region III. The corresponding vorticity field is presented in Fig. 5.2.7. The concentration of vorticity phase-locked to the frequency of excitation, decreases with increasing X .

5.3. The intensity of the fluctuations, the Reynolds stress and their respective spectral distributions

The inclination angle of the large vortex lump to the direction of the free stream is related to the sign of the Reynolds stress as schematically sketched below (Browand 1980). When the inclination angle of the eddy θ is greater than $\pi/2$ the associated Reynolds stress is positive; when it is less than $\pi/2$ the Reynolds stress changes sign and becomes negative.



The phase-locked vortices in region I have an elliptical shape with an inclination angle greater than $\pi/2$. It is expected, therefore, that the phase-locked $-\langle \bar{u}'\bar{v}' \rangle$ product in this region would be positive. The opposite is true for regions II and III where the inclination angle of the vortices to the mean flow is less than $\pi/2$ and $-\langle \bar{u}'\bar{v}' \rangle$ is expected to be negative there. The change of sign occurs in the transition between regions I and II.

The Reynolds stress $\tau = -\rho \overline{u'v'}$ is linked to the mean momentum equation and to the mean kinetic energy equation; therefore, changes in the distribution of $-\overline{u'v'}$ are associated with changes in the momentum thickness θ and with the flow of energy to or from the turbulent motion. The overall energy production term can be subdivided into a phase-locked (coherent) term and a

random (turbulent) term. The reader is referred to Hussain's article (1983) discussing the governing equations of the flow, using what is generally referred to as the triple decomposition.

The production of energy integrated across the flow is shown in Fig. 5.3.1 as a function of the streamwise distance. The overall production term (marked by crosses) and the phase-locked production term (obtained by $-\langle \bar{u} \bar{v} \rangle \frac{d\bar{u}}{dy}$ and marked by triangles) are plotted together because one may relate the energy production and the Reynolds stress to the rate of spread of the shear layer.

5.3.1. Region I

Transverse distributions of Reynolds stress measured at four X locations in the portion of region I, in which $d\theta/dx$ is constant (i.e. $X < 500$ mm), are shown in Fig. 5.3.2). The data is compared with the phase-locked $-\langle \bar{u} \bar{v} \rangle$ product, marked by triangles on the same figure, which accounts for most of the Reynolds stress. Temporally averaged and phase-locked energy production terms behave in a similar manner (Fig. 5.3.3), suggesting that the flow is governed by the phase-locked fluctuations. Most of the energy (about 75%) is transferred from the mean motion to the phase-locked fluctuations that dominate the flow in this region. Graphs representing the cross-spectra at identical X locations (Fig. 5.3.4), show that the disturbance frequency dominates the flow, in spite of the fact that the first harmonic may also be detected. Higher harmonics do appear in the power spectra of the longitudinal and lateral velocity components (Figs. 5.3.5

and 5.3.6, respectively) but they are not sufficiently correlated to influence the Reynolds stress.

The harmonic distortion, defined as the ratio between the spectral peak of the harmonic frequency to the excitation frequency, may be deduced from figures 5.3.5 and 5.3.6. The harmonic distortion of the streamwise component of velocity increased by approximately an order of magnitude between $X=200$ mm and $X=400$ mm at the outer peripheries of the shear layer but it did not increase at $(Y-Y_0)/\theta=0$; the harmonic distortion of the lateral velocity component increased by a factor of 2 over the same distance and did so, uniformly, across the shear layer. The increase in the harmonic distortion with downstream distance suggests the ever increasing importance of the non linear terms in the equation of motion with increasing X .

5.3.2 The first transition subregion

The first transition subregion ($500 < X < 640$ mm) is defined as the region in which $d\theta/dx$ changes from its constant positive value in region I to a constant negative value in region II. A local maximum of the momentum thickness is attained at $X=560$ mm, where the overall turbulent energy production vanishes (Fig. 5.3.1) while the end of this transition subregion, is marked by a minimum of the overall production ($X=640$ mm).

The distributions of $-\overline{u'v'}$ and $\langle -\overline{u'v'} \rangle$ as well as the corresponding energy production terms resemble each other in this subregion (figs. 5.3.7 and 5.3.8) as might have been expected from Fig. 5.3.1. The flow contin-

ues, therefore, to be dominated by the excitation frequency. The Reynolds stresses and the concomitant production terms change sign to become negative. The change is initially observed on the high velocity side of the flow and is associated with the increased inclination of the large vortices resulting from the comparatively larger phase velocity in this region (see Fig. 5-4 in Gaster, Kit & Wagnanski).

The first harmonic of the cross spectrum, which has a magnitude comparable to the amplitude of the imposed frequency, changes its sign first and the imposed frequency follows (Fig. 5.3.9). The interaction between the imposed fluctuations and their first harmonic frequency appears to be a dominant factor responsible for the contraction of the mixing layer with downstream distance and will be discussed later. (Fig 5.3.9).

The power spectra of the two velocity components in the first transition region are shown in Figs. 5.3.10 and 5.3.11. The harmonic distortion of both velocity components diminishes in this region particularly on the high velocity side of the mixing layer. It is interesting to note that the streamwise component of velocity at the excitation frequency is amplified between $X=520$ mm and $X=640$ mm while the same component at the harmonic frequency decays; the opposite trend is noticeable for the transverse velocity component.

5.3.3 Region II

In region II ($640 < X < 840$ mm) the momentum thickness of the mixing layer

decreases. The overall energy production is negative (Fig. 5.3.1) and the inclination angle of the vortices on the high-speed-side of the flow decreases. The phase-locked oscillations still dominate the flow (as can be seen in Figs. 5.3.12 and 5.3.13) and the phase-locked energy production throughout the region is negative (Fig. 5.3.1).

The fluctuating velocity components in this region are dominated by the large vortices which are perfectly locked to the phase of the flap motion (see also Oster & Wygnanski). Although the product of $\langle -\bar{u}'\bar{v}' \rangle \frac{d\bar{U}}{dY}$ is negative (Fig. 5.3.13) suggesting that energy might be lost by these large eddies to the mean motion the actual energy contained at the frequency of excitation does not diminish between $660 < X < 840$ mm (Fig. 5.3.15) the harmonic component however (whose frequency is $2f$) loses most of its energy between $440 < X < 840$ mm. The harmonic distortion which is 0.5 at $X=440$ mm and $(Y-Y_0)/\theta=2$ (Fig. 5.3.5) is reduced to 0.05 at a corresponding lateral location at $X=840$ mm (Fig. 5.3.15). The second harmonic ($F=3f$) which is significant in region I disappears completely in region II and most of the random fluctuations are shifted towards frequencies which are lower than the excitation frequency. At $X=200$ mm the background spectra of u'^2 in the range between 0-200 Hz is flat while the spectrum of v'^2 slopes upwards towards higher frequencies. At $X=440$ mm this spectrum of v'^2 has a broadband maximum around the harmonic frequency $2f$ (Fig. 5.3.6); at $X=640$ mm this maximum shifts towards the excitation frequency and remains there till the end of region II (Fig. 5.3.16). The $u'v'$ spectrum has two negative peaks at the excitation frequency and at its first harmonic between $600 < X < 800$ mm. The relative importance of the $-\bar{u}'\bar{v}'$ product at $2f$ decreases with increas-

ing X in this region until it vanishes across the entire mixing layer at $X=840$ mm (Figs. 5.3.9 and 5.3.14); the $\langle -\bar{u}'\bar{v}' \rangle$ product at the excitation frequency becomes negative at $X=600$ mm and remains negative until $X=900$ mm).

5.3.4 The second transition region

The transition from region II to III ($840 < X < 1080$ mm) is marked by a renewed growth of the momentum thickness with increasing X and a positive overall production of turbulent energy.

In this region we observe, for the first time, that the phase-locked $\langle -\bar{u}'\bar{v}' \rangle$ product and the associated production of energy deviate from the time-averaged $\langle -\bar{u}'\bar{v}' \rangle$ product and overall energy production (Figs. 5.3.17 and 5.3.18); while the overall production is positive, the phase-locked production of energy is negligibly small. Positive values do appear in the phase-locked $\langle -\bar{u}'\bar{v}' \rangle$ product and $\langle -\bar{u}'\bar{v}' \rangle \frac{d\bar{u}}{dy}$ in the central region of the mixing layer, but their influence is offset by the negative values at the peripheries. Positive peaks in the cross spectra appear in both the disturbance frequency and its first harmonic in the vicinity of $(Y-Y_0)/\theta=0$. (Fig 5.3.19).

The spectral distributions of u^{-2} and v^{-2} do not change appreciably between $880 < X < 1080$ mm; the harmonic distortion coefficient remains constant and the background turbulence of the v^{-2} fluctuations has a broadband maximum around the excitation frequency (Figs 5.3.20 and 5.3.21).

Since the momentum thickness in this region is smaller than the maximum Θ attained at the end of region I, the mixing layer may return to be linearly unstable to the excitation frequency. This may be the reason for the reappearance of positive phase-locked $-\langle \bar{u} \bar{v} \rangle$ and the corresponding production terms.

5.3.5 Region III

In region III ($X > 1080$ mm) the mixing layer resumes its linear rate of spread with X . The growth rate, however, is approximately equal one half of the growth rate in region I. The overall energy production in this region is positive everywhere (Fig. 5.3.1), and both $-\bar{u} \bar{v}$ product and overall energy production profiles are positive (Figs. 5.3.22 and 5.3.23, respectively). On the other hand, the phase-locked $-\langle \bar{u} \bar{v} \rangle$ and $-\langle \bar{u} \bar{v} \rangle \frac{d\bar{U}}{dY}$ distributions are negative in this region, consequently $\int -\langle \bar{u} \bar{v} \rangle \frac{d\bar{U}}{dY} dY$ is negative (Fig. 5.3.1).

The growth of the mixing layer does not appear to be controlled by the external excitation, since the phase-locked vortices are losing energy through the $-\langle \bar{u} \bar{v} \rangle \frac{d\bar{U}}{dY}$ product. The observation is reinforced by the negative cross spectral peaks occurring at the excitation frequency (Fig. 5.3.24), however, a broad band of positive $-\bar{u} \bar{v}$ product appears at frequencies which are lower than the imposed frequency. In fact, the intensity of the fluctuations at the excitation frequency decreases very slowly with downstream distance for $X > 1100$ mm but the background low frequencies increase by a factor of 5 between $1100 < X < 1700$ mm (Figs. 5.3.25 and

5.3.26). Therefore, eddies which are larger than the eddies associated with the excitation frequency dominate this region. These eddies are not locked in phase to the imposed oscillations and are presumably responsible for the resumed growth of the shear-layer.

5.3.6 The subharmonic frequency

Anticipating that the resumed growth of the mixing layer in region III stems from vortex pairing special attention was paid to this process and to the generation of the subharmonic frequencies. Since the large eddies passing through region II were locked to the phase of the excitation it was assumed that the pairing process will follow suit and therefore, the phase averaging was done at the subharmonic frequency as described in chapter 4. A comparison between the data phase locked to the excitation signal or its subharmonic could not be distinguished suggesting that the process, if it exists, occurs randomly in time or space. Power spectra of u^{-2} and v^{-2} reveal interesting exchanges between the excitation frequency and its harmonic component ($F=2f$) in regions I and II and a good portion of region III (up to $X=1300$ mm) but they do not show a clear appearance of a subharmonic frequency ($F=f/2$) as was initially expected (Fig 5.3.26). Comparing, say, the last spectrum shown in Fig. 5.3.16 (taken at $X=840$ mm and $(Y-Y_0)/\theta=2$) to a corresponding spectrum in Fig. 5.3.26 ($X=1700$ mm) one notices the following (i) disappearance of peaks at the harmonic frequency at $X=1700$ mm (ii) the disappearance of side bands (i.e. the broadening of the spectrum) at the excitation frequency (iii) the decay of the peak at the peak at the excitation frequency (iv) the increase in the background level of all fre-

quencies that $F < f$ by approximately an order of magnitude.

Cross spectra shown in Fig. 5.3.24, smoke pictures illuminated at the subharmonic frequency, phase-locked streakline patterns and vorticity contours did not show any noticeable activity associated with pairing. It was therefore concluded that high amplitude excitation might have inhibited the pairing process, as we understood it. We are, therefore, continuing with experiments in which the flow is excited by two frequencies which are phase-locked to one another hoping to lock onto the pairing process.

CHAPTER 6

A DETAILED COMPARISON WITH THE LINEAR INVISCID STABILITY THEORY

The inviscid stability theory provides a powerful tool in modeling the development of slightly disturbed flows. Gaster, Kit and Wygnanski (to be published in J.F.M.) applied this model to a turbulent, slowly diverging, mixing layer and compared the theoretical calculations for the streamwise velocity component with experimental results. Although the lateral distributions of normalized amplitudes and phases showed a good agreement with the model, the predicted amplification rate exceeded the experimental observations. A partial purpose of this experiment was to increase the excitation level until a harmonic distortion occurs and observe the shortcomings of the linear theory. The measurements were also extended to include two velocity components from which phase-locked vorticity and $-\bar{u}'v'$ product were calculated. All measurements were compared with the theoretical calculations.

The inviscid equation of motion describing the vorticity of a two-dimensional flow can be written as follows:

$$(6.1) \quad \frac{D\Omega}{Dt} = \frac{\partial \Omega}{\partial t} + u \frac{\partial \Omega}{\partial \xi} + v \frac{\partial \Omega}{\partial \eta} = 0$$

where $\Omega = \nabla^2 \bar{\Psi} + \nabla^2 \Psi$;

$\bar{\Psi}(\xi, \eta)$ is a complex two-dimensional mean stream function;

$\Psi(\xi, \eta, t)$ is a complex time-dependent stream function;

ξ and η being the dimensionless longitudinal and lateral coordinates, res-

pectively.

It is assumed that ψ varies slowly with ξ and therefore $\psi(\xi, \eta, t)$ may be represented by:

$$(6.2) \quad \psi(\xi, \eta, t) = A(\xi) \phi(\xi, \eta) e^{i[\int_0^\xi \alpha(x) dx - \omega t]}$$

where the slow variation with ξ is taken up by the amplitude $A(\xi)$ and the eigenfunction $\phi(\xi, \eta)$ (i.e. their first derivatives with respect to ξ are of order ϵ). Substituting (6.2) into (6.1) and omitting higher order terms (i.e. second derivatives of ϕ and A with respect to ξ or cross-products of first order derivatives), one obtains after some manipulation two equations: (i) the local inviscid Orr-Sommerfeld equation for the equivalent parallel flow, involving the local mean velocity profile for order 1:

$$(6.3) \quad iA\{(\phi'' - \alpha^2 \phi)(\bar{U}_\alpha - \omega) - \bar{U}''' \phi \alpha\} = 0$$

and (ii) an equation for order ϵ , from which the amplitude $A(\xi)$ can be calculated:

$$A(\xi) = \exp\left[-\int_0^\xi \frac{N(x)}{M(x)} dx\right]$$

where $N(\xi)$ and $M(\xi)$ are the following integrals:

$$\begin{aligned} M(\xi) &= \int_0^\infty \{2\alpha\omega\phi + \bar{U}[\phi'' - 3\alpha^2\phi] - \bar{U}''' \phi\} \delta\eta \\ N(\xi) &= \int_0^\infty \{\omega[\phi(\partial\alpha/\partial\xi) + 2\alpha(\partial\phi/\partial\xi)] + \bar{U}[(\partial\phi''/\partial\xi) - 3\alpha^2(\partial\phi/\partial\xi) - 3\alpha\phi(\partial\alpha/\partial\xi)] \\ &\quad + \phi'(\partial\bar{U}'/\partial\xi) - \bar{U}'''(\partial\phi/\partial\xi) + \bar{V}[\phi''' - \alpha^2\phi']\} \delta\eta \end{aligned}$$

The notation $'$, $''$, $'''$, represents the first, second and third derivatives with respect to η , respectively. This equation stems from a condition described by Ince (1956): "A necessary and sufficient condition that a non-homogeneous linear system with homogeneous boundary conditions may

have a solution is that every solution of the homogeneous adjoint system (homogeneous equation and boundary conditions) satisfies the relation:"

$$\int_{-\infty}^{\infty} g \phi d\eta = 0$$

This condition is commonly referred to as the solvability condition. The function ϕ is the eigenfunction corresponding to an eigenvalue of the adjoint Orr-Sommerfeld system and has the form:

$$\phi = \psi / (\bar{U} - \omega / \alpha)$$

The shape of the mean velocity profile used for the solution of the problem was a fit based upon the hyperbolic tangent profile and its derivatives (suggested by Prof. R. E. Kaplan from the University of Southern California):

$$U(\eta/\xi) = 0.5 \{1 + \tanh(\eta/\xi) [1 - C/\cosh^2(\eta/\xi)]\}$$

The constant C was chosen to be -0.67. This profile fits the experimental data better than the hyperbolic tangent profile commonly used in the literature. The chosen analytical expression is marked by dots in Fig. 6.1, while the experimental profiles are marked by a variety of symbols.

The method for calculating the theoretical eigenfunctions is described in detail by Crighton & Gaster (1976) and by Gaster, Kit & Wagnanski. The dimensionless coordinates for the experimental results were calculated by:

$$\xi = (X - X_0) \frac{d\theta}{dX} / \theta_t / L$$

$$\frac{\eta}{\xi} = \theta_t (Y - Y_0) / \theta$$

where θ_t represents the theoretical momentum thickness at $\alpha_1 = 1$ ($\theta_t = 0.2467$); X_0 is the virtual origin of the flow where the momentum thickness vanishes $\frac{d\theta}{dX}$ yields the growth-rate of the experimental momentum thickness;

y_0 is the lateral coordinate corresponding to the location at which

$$\bar{U} = 0.5(U_1 + U_2);$$

θ is the local experimental momentum thickness.

The definition of L is: $L = (U_2 - U_1)C_0 / 2\pi f$;

where C_0 is a constant chosen to be 3 in order to ensure that $\alpha_1 = 0$ at the end of the calculation domain;

f is the experimental excitation frequency in Hz

$(U_2 - U_1)$ is the difference between the mean free-stream velocities in mm/sec.

The two components of the oscillatory motion described by amplitude and phase were calculated by Fourier representation of the velocity signals locked to the disturbance frequency. Two coefficients were calculated for each phase-locked signal:

$$A = \frac{2}{T} \int_0^T (u(t) \sin(\omega_0 t)) dt \quad \text{and} \quad B = \frac{2}{T} \int_0^T (u(t) \cos(\omega_0 t)) dt$$

(where ω_0 is the frequency of the fluctuations), or using the numerical scheme:

$$A = \sum_{j=1}^{NPP} \langle u(j) \rangle \sin[(j-1)*2\pi/NPP] \quad \text{and} \quad B = \sum_{j=1}^{NPP} \langle u(j) \rangle \cos[(j-1)*2\pi/NPP]$$

The amplitude and phase of each velocity signal were derived by:

$$C = \sqrt{A^2 + B^2} \quad \text{and} \quad \phi = \arctan(A/B)$$

The $-\bar{u}^* \bar{v}^*$ product amplitude is by definition:

$$T = C_1 * C_2 * \cos(\phi_1 - \phi_2)$$

where the subscripts 1 and 2 stand for the longitudinal and lateral directions, respectively.

The amplitude and the phase distributions of the spanwise vorticity component, were computed by numerical differentiation of neighboring phase-locked velocity vectors, which were then Fourier transformed.

The comparison between the experimental results and the theoretical calculations is divided into two categories:

A comparison between normalized lateral distributions of the following functions:

- a) The amplitude of the longitudinal velocity component
(Figs. 6.2(a),(b)).
- b) The phase of the longitudinal velocity component
(Figs. 6.3(a),(b)).
- c) The amplitude of the transverse velocity component
(Figs. 6.4(a),(b)).
- d) The phase of the transverse velocity component
(Figs. 6.5(a),(b)).
- e) The amplitude of the vorticity (Figs. 6.6(a),(b))
- f) The phase of the vorticity (Figs. 6.7(a),(b))
- g) The amplitude of $-\bar{u}\bar{v}$ product (Figs. 6.8(a),(b))

The triangles in all the figures represent experimental results while the theoretical predictions at corresponding ξ stations are marked by solid curves. Both the dimensionless coordinate ξ and the corresponding stream-wise distance from the virtual origin appear above each curve.

The amplitude distribution of any quantity Q in Figs. 6.2-6.8 was normalized by the local integral $\int_{-\infty}^{\infty} |Q| d\eta$. The phase distributions were matched at a single arbitrary point, namely at $\eta=0$.

The good agreement between all the calculated and measured quantities indicates that the linear inviscid theory serves as a good first step in predicting the growth of the disturbances in region I of a turbulent mixing layer.

The overall amplification of the longitudinal velocity in the streamwise direction which is represented by $\int_{-\infty}^{\infty} |u_f|^2 d\eta$ is shown in Fig. 6.9, the corresponding integral for lateral velocity component is plotted in Fig. 6.10 while the spanwise vorticity and $|\bar{u}^2 \bar{v}^2|$ product are shown in Figs. 6.11 and 6.12, respectively. All the figures are plotted on semi-logarithmic coordinates in which the abscissa is the dimensionless streamwise coordinate and the ordinate is the local value of the integral normalized by its value at the first station. The triangles represent the experimental data while the theoretical values are plotted by solid curves.

All four integrals calculated theoretically increase with X , the measured amplitudes of the two velocity components also increase with X , but at considerably slower rate. The experimental and the theoretical integrals of the fluctuations in the lateral direction increase much more rapidly with X than the streamwise component of the fluctuations (cf. Fig. 6.9 with Fig. 6.10). The integral of the experimental longitudinal velocity component tends to decrease towards the end of the domain of comparison.

The vorticity amplitude, integrated across the flow, decreases with X , and the integrated $-\bar{u}'v'$ product remains constant over most of the domain of comparison and decreases towards the end of this domain. The discrepancy between the high amplification rates predicted by the linear model and the relatively low amplification rates realized in the experiment deserves special attention in view of the excellent agreement between the shapes of the theoretical and experimental eigenfunctions.

The linear model used assumes that the flow departs a little from the parallel flow geometry, and a weak modification in the parallel stability theory is sufficient to describe the resulting solution. The small scale turbulence was not accounted for by the linear model, but its existence may contribute somewhat to the above-mentioned discrepancy between theory and experiment. The turbulent energy production in region I accounts for 25% of the total (Fig. 5.3.1), while the remaining 75% is attributed to the phase-locked fluctuations at the disturbance frequency and its first harmonic. The contribution of the first harmonic was not accounted for in the analysis of the data but it is not insignificant (Fig. 6.13)

Another aspect that must be considered when applying a linear model is the level of the fluctuation. The displacement amplitude of the oscillating flap in the experiment described by Gaster, Kit & Wygnanski was much smaller than the amplitude in the present experiment. In spite of it, they found that 45% of the overall energy at $\xi=0.786$ occurred at the imposed frequency, while the maximum level of the streamwise fluctuations at this point was 0.18. These fluctuation levels are not small and it is not at

all obvious that the linearization of the equations of motion is justified.

CHAPTER 7

CONCLUDING REMARKS

The strongly excited turbulent mixing layer was examined in great detail, nevertheless, many questions remain to be answered. For example:

- (1) Can the big initial growth-rate of the shear layer be predicted?
- (2) What causes the momentum thickness to level off at the end of region I and what is the cause for the resumption of growth in region III?
- (3) Why does the shear layer actually shrink in region II when the level of excitation is high?
- (4) Why do the predicted shapes of the eigenfunctions agree so well with experiment and the rates of amplification do not?

We believe that some of the answers can be provided by expanding the linear calculations to account for the nonlinear processes. The perturbations introduced by the flap have a sizeable harmonic component (at a frequency $F=2f$) which is initially amplified with X more swiftly than the excitation frequency itself. As the mean flow broadens and becomes neutrally stable to the harmonic frequency, on the basis of the inviscid linear model, the amplitude of the harmonic fluctuations diminishes. The process starts to occur around $X=500$ mm in this case, where the $-\bar{u}''\bar{v}''$ product of $F=2f$ becomes negative (Fig. 5.3.9) nevertheless remnants of the harmonic frequency are still noticeable at $X=1300$ mm. The slow decay of the harmonic amplitude may be attributed to a contribution from the fundamental fre-

quency through a nonlinear process. The exchange of energy between the two frequencies is currently investigated in a fully controlled experiment.

The $-\overline{u'v'}$ product at the excitation frequency changes sign at $X \approx 560$ mm corresponding to $f\theta/U_c = 0.030$ which is the neutrally stable Strouhal number for the local mean velocity profile. The subharmonic frequency at this location was insignificant and could not sustain the amplitude of the of the fundamental frequency by nonlinear means; some exchange could have taken place, however, between the harmonic, the fundamental and the mean. The negative $-\overline{u'v'}$ product at the fundamental frequency (Fig. 5.3.9) affected the mean flow field causing an actual shrinkage of the shear layer. This observation is consistent with the observations of Oster & Wygnanski (1982, Fig. 12) who also noticed that a high amplitude oscillation produced $\frac{d\theta}{dx} < 0$ in region II. At the end of region II (at $900 < X < 1100$ mm) the shear layer became sufficiently narrow and the shape of the mean velocity was sufficiently altered (Fig 5.1.3) that the shear layer became again unstable to the fundamental frequency (Fig. 5.3.19). At this location, the amplitudes of the random fluctuations at low frequencies became much larger and the shear layer resumed its slow growth.

The explanation put forward for the growth of the mixing layer is based on the premise that waves interacting in a nonlinear manner produce the observed behaviour of the excited shear layer. It may serve as an alternative explanation to the pairing process provided it will be proven rigorously and supplemented by additional experimental verification.

REFERENCES

1. ACTON, E.: 1976, J. Fluid Mech., 76, 651.
2. ASHURST, W.T.:
1976, Bulletin of the Amer. Phy. Soc., Ser. II, V.20,
1428.
3. BREIDENTHAL, R.: 1980, Phys. of Fluids, 23(10), 1929.
4. BROWAND, F.K. & TROUTT, T.: 1980, J. Fluid Mech. 97, 772.
5. BROWN, G.L. & ROSHKO, A.:
1971, Turbulent Shear Flows, AGARD-CP-93, 23-1.
6. BROWN, G.L. & ROSHKO, A.: 1974, J. Fluid Mech. 64, part 4, 775.
7. CHANDRSUDA, C., MEHTA, R.D., WEIR, A.D., & BRADSHAW, P.:
1978, J. Fluid Mech. 85, part 4, 693.
8. CORCOS, G.M. & LIN S.J.: 1984, J. Fluid Mech., 139, 67.
9. CORCOS, G.M. & SHERMAN, F.S.: 1976, J. Fluid Mech., 73, 241.
10. CORCOS, G.M. & SHERMAN, F.S.: 1984: J. Fluid Mech., 139, 29.
11. CRIGHTON, D.G. & GASTER, M.: 1976, J. Fluid Mech. 77, 397
12. DIMOTAKIS, P.E. & BROWN, G.L.:
1976, J. Fluid Mech. 78, part 3, 535.
13. GASTER, M., WYGNANSKI, I. & KIT, E:
Large Scale Structures in a Forced Turbulent Mixing Layer
(to be published in J. Fluid Mech.).
14. HO, C.M. & HUANG, L.S.:
1978, Bulletin of the Amer. Phys. Soc., Ser II., vol. 23,
1007.
15. HO, C.M. & HUANG, L.S.:
1982, J. Fluid Mech., 119, 443.
16. HUSSAIN, A.K.M.F.: 1983, Phys. Fluids 26, 2816
17. INOUE, O.: 1983, ISAS Research note 228.
18. MICHALKE, A.: 1964, J. Fluid Mech. 19, 543
19. MICHALKE, A.: 1965, J. Fluid Mech. 23, 521
20. MONKEWITZ, P.A. & HUERRE, P.:
1982, Phys. of Fluids, 25(7), 1137.

21. OSTER, D. & WYGNANSKI, I.: 1982, J. Fluid Mech. 123, 91
22. OSTER, D., WYGNANSKI, I., & FIEDLER, H.:
1977, Turbulence in Internal Flows, 67, hemisphere Press,
Washington, D.C.
23. OSTER, D., WYGNANSKI, I., DZIOMBA, B. & FIEDLER, H.:
1978, Lecture Notes in Physics 75, 48, Structures
and Mechanisms in Turbulence I, H. Fiedler (ed.),
Springer-Verlag, Berlin.
24. PATNAIK P.C., SHERMAN, F.S. & CORCOS G.M.: 1976, J. Fluid Mech.
73, 215.
25. PUI, N.K. & GARTSHORE, I.: 1979, J. Fluid Mech. 91, part 1, 111.
26. RILEY, J.J. & METCALFE, R.W.: 1980, AIAA Paper No. 80-0274.
27. ROSHKO, A.; 1976, AIAA Journal, 10, 1349.
28. WINANT, C.D. & BROWAND, F.K.:
1974, J. Fluid Mech. 63, part 2, 237.
29. WYGNANSKI, I., OSTER, D., FIEDLER, H. & DZIOMBA B.:
1979, J. Fluid Mech. 93, part 2, 325.

LIST OF FIGURES

Figure

- 1.1 Schematic sketch of the two-dimensional mixing layer.
- 2.1 The wind tunnel.
- 5.1.1 The variation of the momentum thickness, θ , and the width of the mixing layer, b , with distance from the splitter plate.
- 5.1.2 The variation of $Y_{0.10}$, $Y_{0.50}$ and $Y_{0.95}$ with distance from the splitter plate.
- 5.1.3 A comparison between the normalized mean velocity profiles in regions I and III.
- 5.2.1 The phase-locked structures: (a) A smoke picture with illuminated stroboscopically. Exposure time = 0.8 sec. (b) Calculated streaklines. (c) Calculated isodynes.
- 5.2.2 The phase-locked structures: (a) Calculated streaklines. (b) Calculated isodynes.
- 5.2.3 The phase-locked structures in region I: (a) Calculated streaklines. (b) Calculated isodynes.
- 5.2.4 The phase-locked structures in region II: (a) Calculated streaklines. (b) Calculated isodynes.
- 5.2.5 The phase-locked structures in region III: (a) Calculated streaklines. (b) Calculated isodynes.
- 5.2.6 Temporal evolution of streaklines.
- 5.2.7 Temporal evolution of isodynes.
- 5.3.1 The variation of laterally integrated overall and phase-locked energy production with X .
- 5.3.2 The distribution of $-\bar{u}^2\bar{v}^2/(U_2-U_1)^2$ and $-\langle\bar{u}^2\bar{v}^2\rangle/(U_2-U_1)^2$ in region I.
- 5.3.3 The distribution of $-\bar{u}^2\bar{v}^2\frac{dU}{dY}/(U_2-U_1)^3$ and $-\langle\bar{u}^2\bar{v}^2\rangle\frac{dU}{dY}/(U_2-U_1)^3$ in region I.
- 5.3.4 The cross spectra of u' and v' in region I.
- 5.3.5 The power spectra of the streamwise velocity component in region I.
- 5.3.6 The power spectra of the lateral velocity component in region I.

- 5.3.7 The distribution of $\overline{u'v'}/(U_2-U_1)^2$ and $-\langle\overline{u'v'}\rangle/(U_2-U_1)^2$ in the first transition region.
- 5.3.8 The distribution of $\overline{u'v'}\frac{dU}{dY}/(U_2-U_1)^3$ and $-\langle\overline{u'v'}\rangle\frac{dU}{dY}/(U_2-U_1)^3$ in the first transition region.
- 5.3.9 The cross spectra of u' and v' in the first transition region.
- 5.3.10 The power spectra of the streamwise velocity component in the first transition region.
- 5.3.11 The power spectra of the lateral velocity component in the first transition region.
- 5.3.12 The distribution of $\overline{u'v'}/(U_2-U_1)^2$ and $-\langle\overline{u'v'}\rangle/(U_2-U_1)^2$ in region II.
- 5.3.13 The distribution of $\overline{u'v'}\frac{dU}{dY}/(U_2-U_1)^3$ and $-\langle\overline{u'v'}\rangle\frac{dU}{dY}/(U_2-U_1)^3$ in region II.
- 5.3.14 The cross spectra of u' and v' in region II.
- 5.3.15 The power spectra of the streamwise velocity component in region II.
- 5.3.16 The power spectra of the lateral velocity component in region II.
- 5.3.17 The distribution of $\overline{u'v'}/(U_2-U_1)^2$ and $-\langle\overline{u'v'}\rangle/(U_2-U_1)^2$ in the second transition region.
- 5.3.18 The distribution of $\overline{u'v'}\frac{dU}{dY}/(U_2-U_1)^3$ and $-\langle\overline{u'v'}\rangle\frac{dU}{dY}/(U_2-U_1)^3$ in the second transition region.
- 5.3.19 The cross spectra of u' and v' in the second transition region.
- 5.3.20 The power spectra of the streamwise velocity component in the second transition region.
- 5.3.21 The power spectra of the lateral velocity component in the second transition region.
- 5.3.22 The distribution of $\overline{u'v'}/(U_2-U_1)^2$ and $-\langle\overline{u'v'}\rangle/(U_2-U_1)^2$ in region III.
- 5.3.23 The distribution of $\overline{u'v'}\frac{dU}{dY}/(U_2-U_1)^3$ and $-\langle\overline{u'v'}\rangle\frac{dU}{dY}/(U_2-U_1)^3$ in region III.
- 5.3.24 The cross spectra of u' and v' in region III.
- 5.3.25 The power spectra of the streamwise velocity component in

region III.

- 5.3.26 The power spectra of the lateral velocity component in region III.
- 6.1 The normalized mean velocity profiles in region I.
- 6.2 The lateral distribution of the amplitudes of u'_f at various streamwise locations.
- 6.3 The lateral distribution of the phase angles of u'_f at various streamwise locations.
- 6.4 The lateral distribution of the amplitudes of v'_f at various streamwise locations.
- 6.5 The lateral distribution of the phase angles of v'_f at various streamwise locations.
- 6.6 The lateral distribution of the amplitudes of the spanwise vorticity component at the excitation frequency at various streamwise locations.
- 6.7 The lateral distribution of the phase angles of the spanwise vorticity component at various streamwise locations.
- 6.8 The lateral distribution of amplitudes of $-\langle \vec{u}' \vec{v}' \rangle$ at the excitation frequency at various streamwise locations.
- 6.9 The amplification of the laterally integrated longitudinal disturbances with distance from the splitter plate.
- 6.10 The amplification of the laterally integrated lateral disturbances with distance from the splitter plate.
- 6.11 The amplification of the laterally integrated spanwise vorticity component with distance from the splitter plate.
- 6.12 The amplification of the laterally integrated $-u'v'$ product with distance from the splitter plate.
- 6.13 The variation of $\int_{-\infty}^{\infty} |u'_f| dY$ and $\int_{-\infty}^{\infty} |u'_{2f}| dY$ with downstream distance..

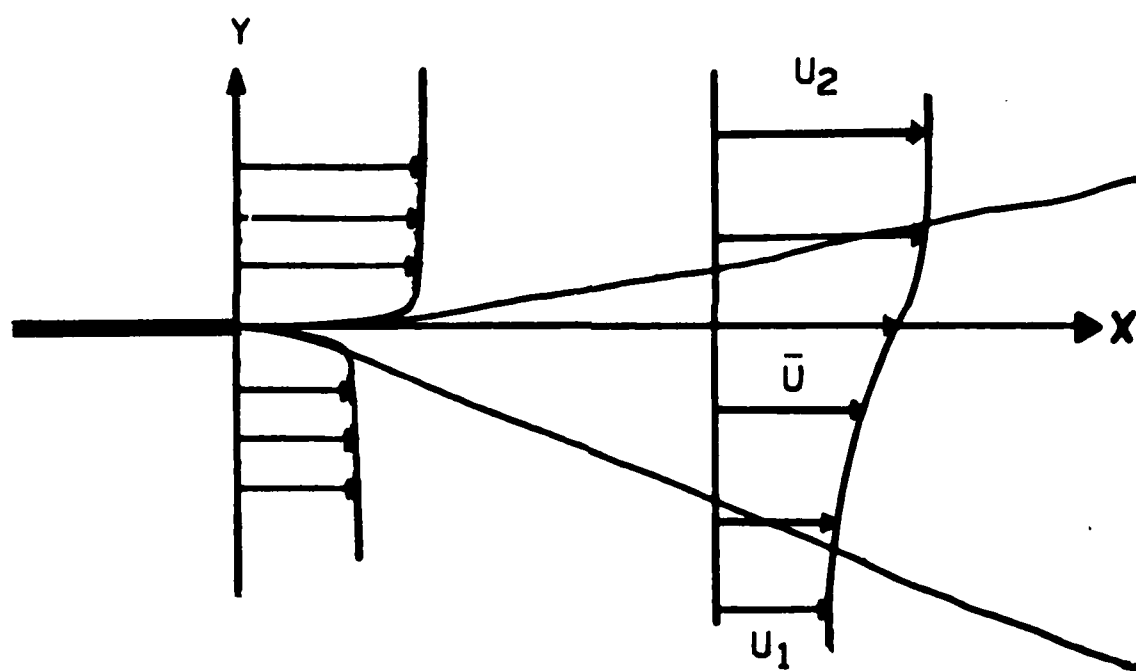


Fig. 1.1

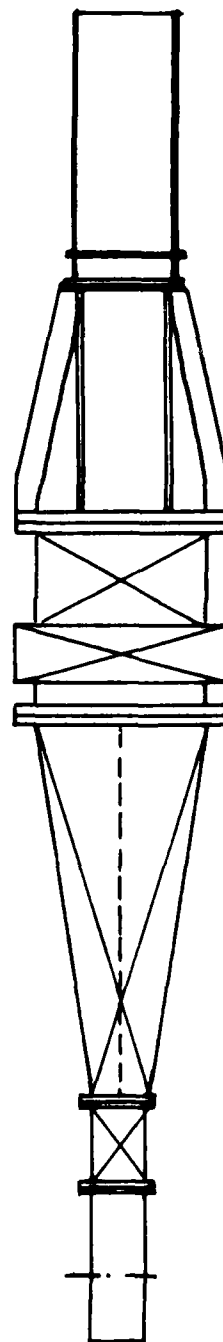
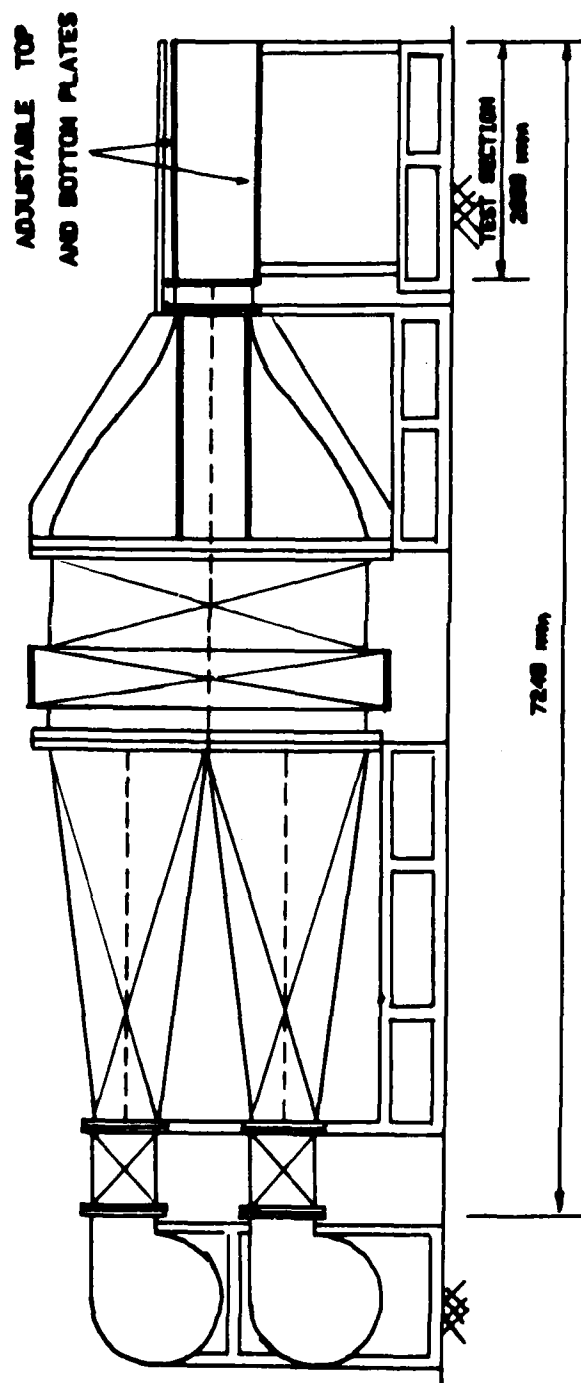


Fig. 2.1

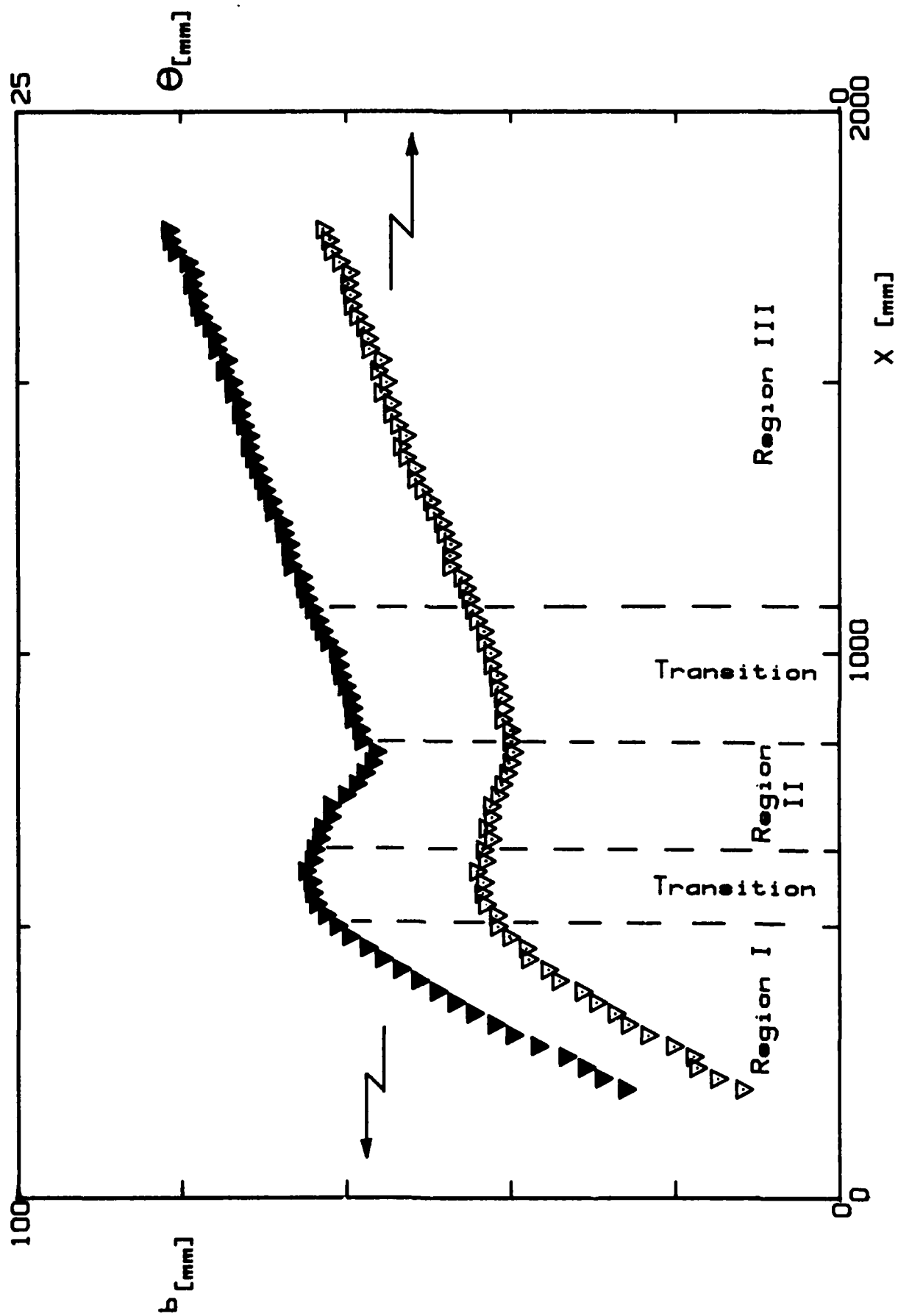


Fig. 5.1.1.1

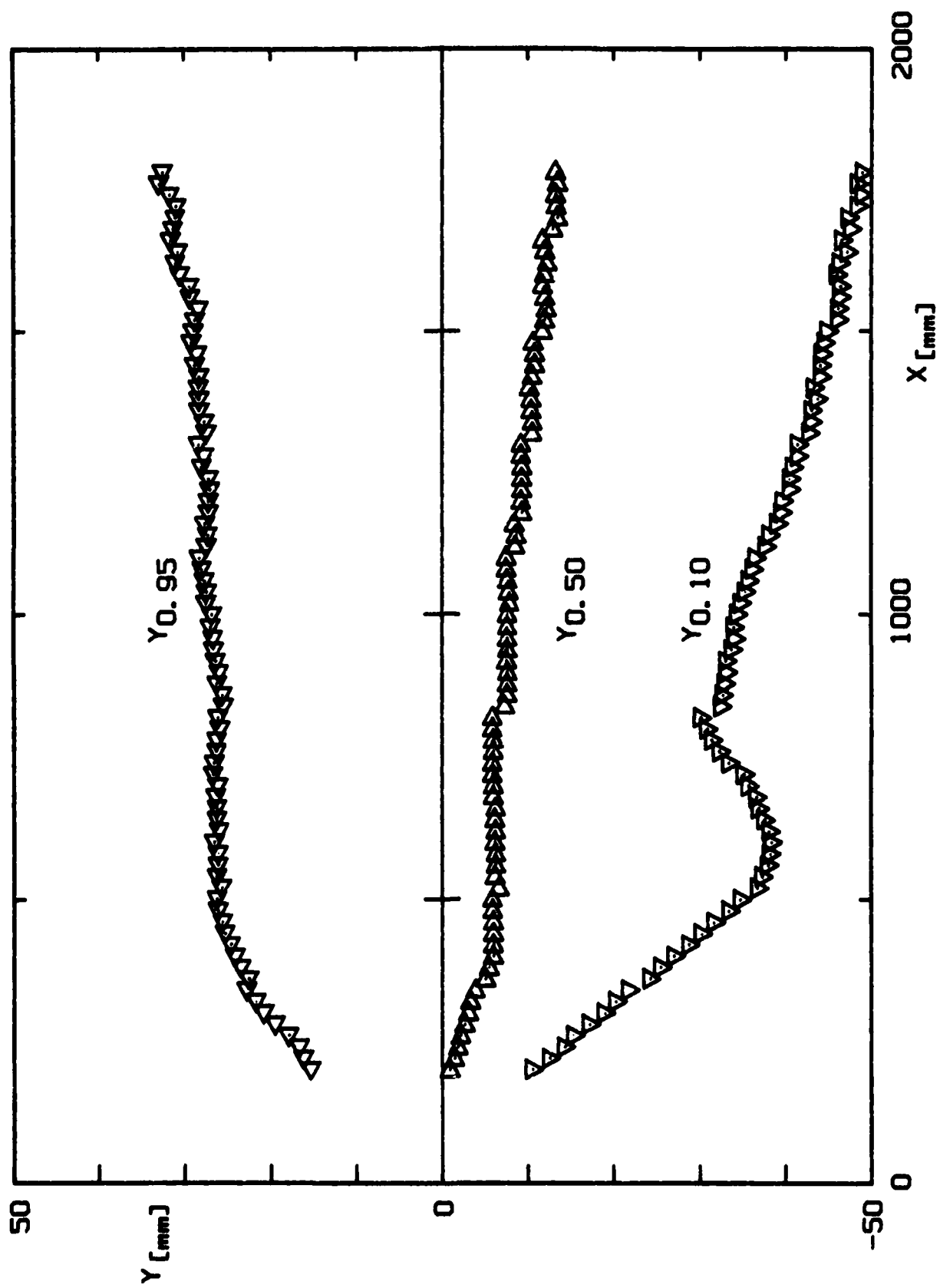


Fig. 5.1.2

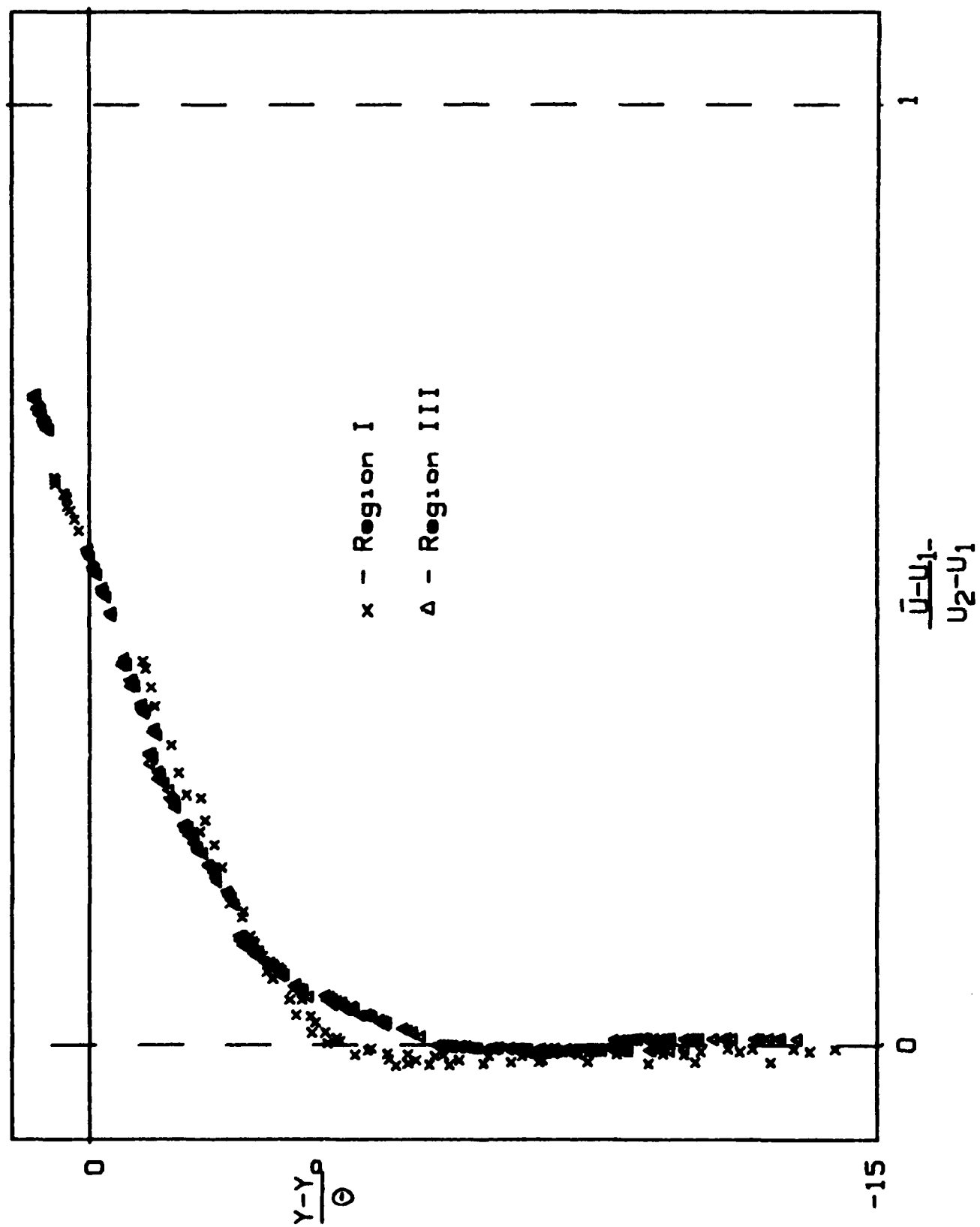


Fig. 5.1.3

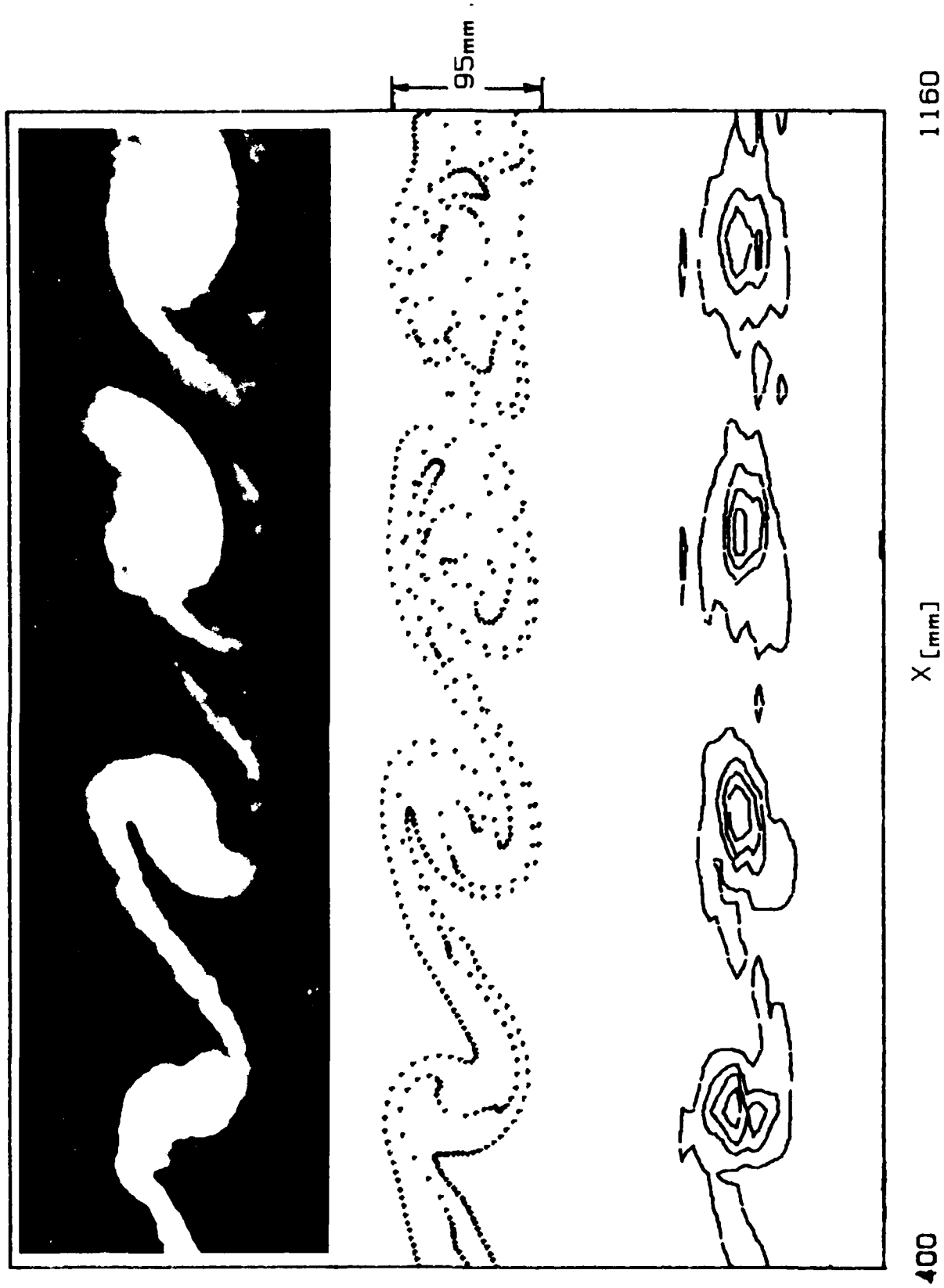
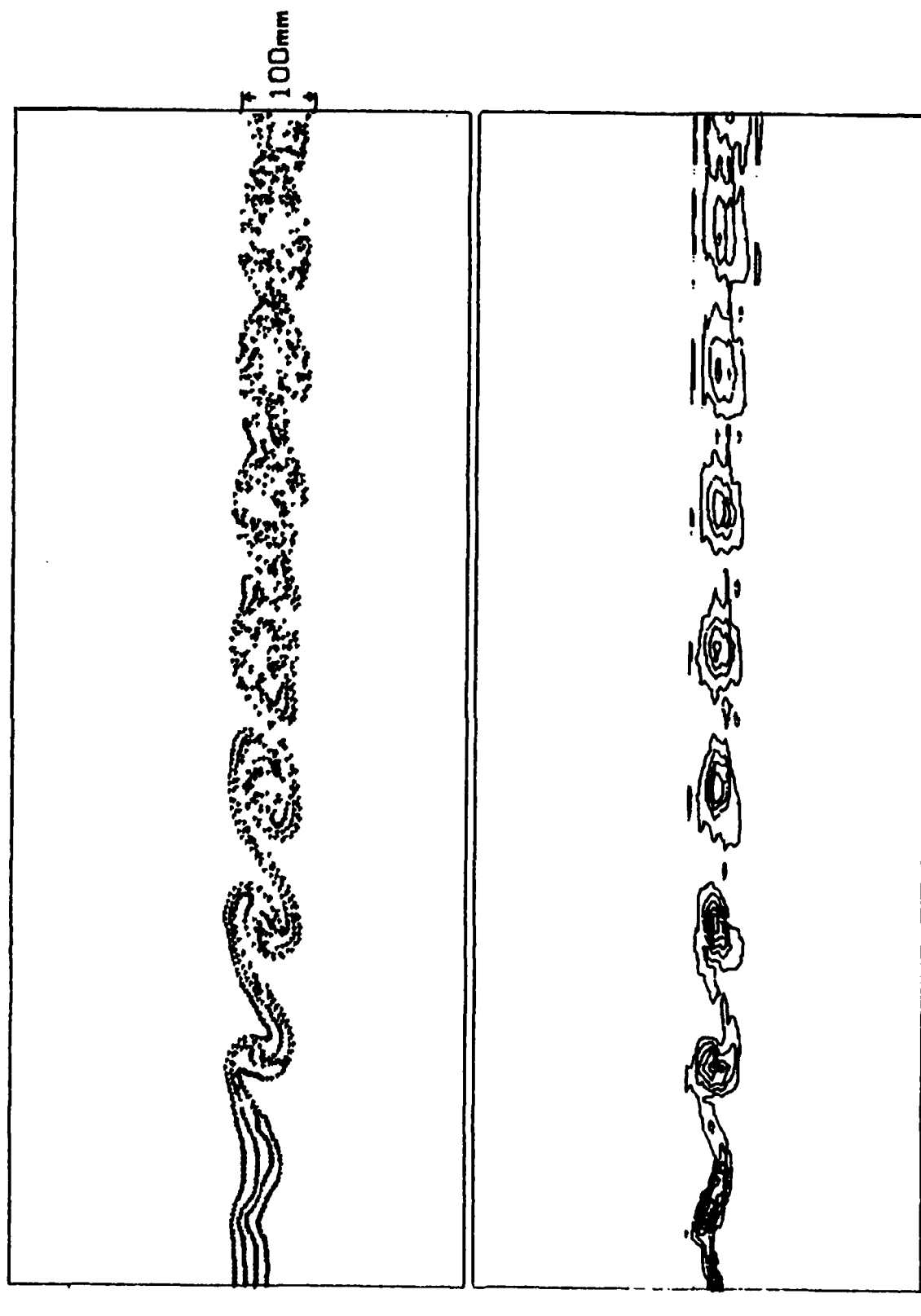


Fig. 5.2.1



200

1780

X [mm]

Fig. 5.2.2

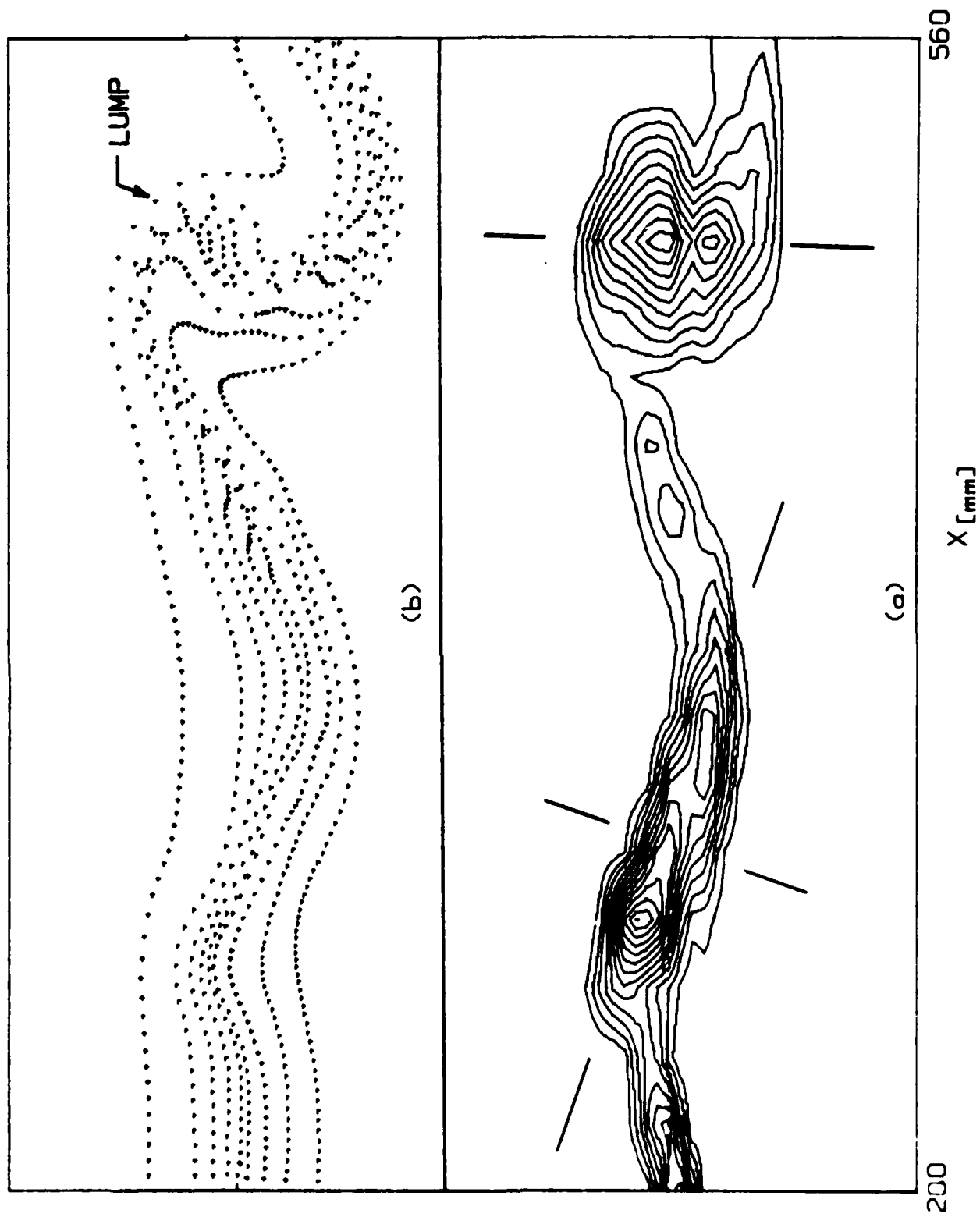


Fig. 5.2.3

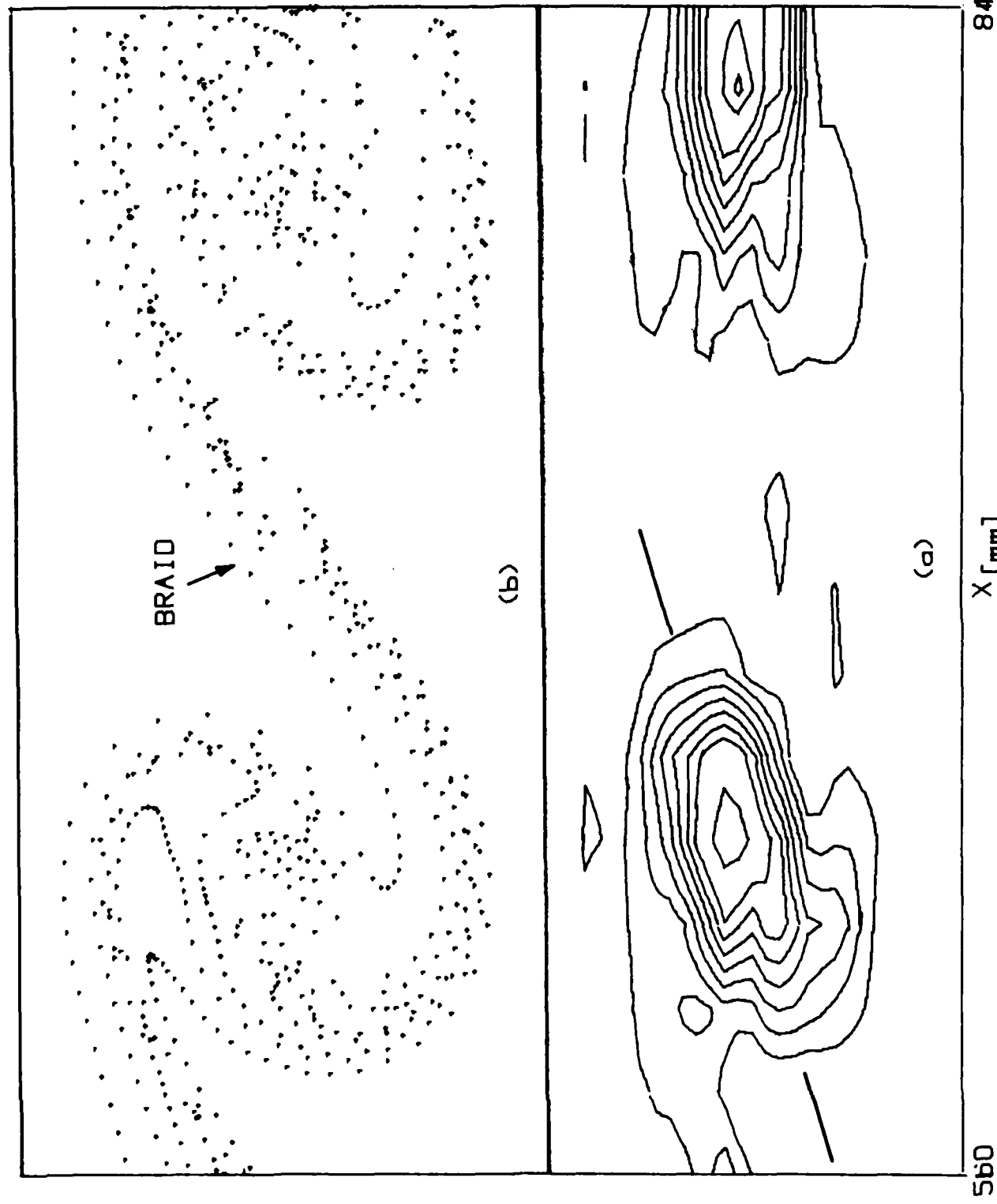
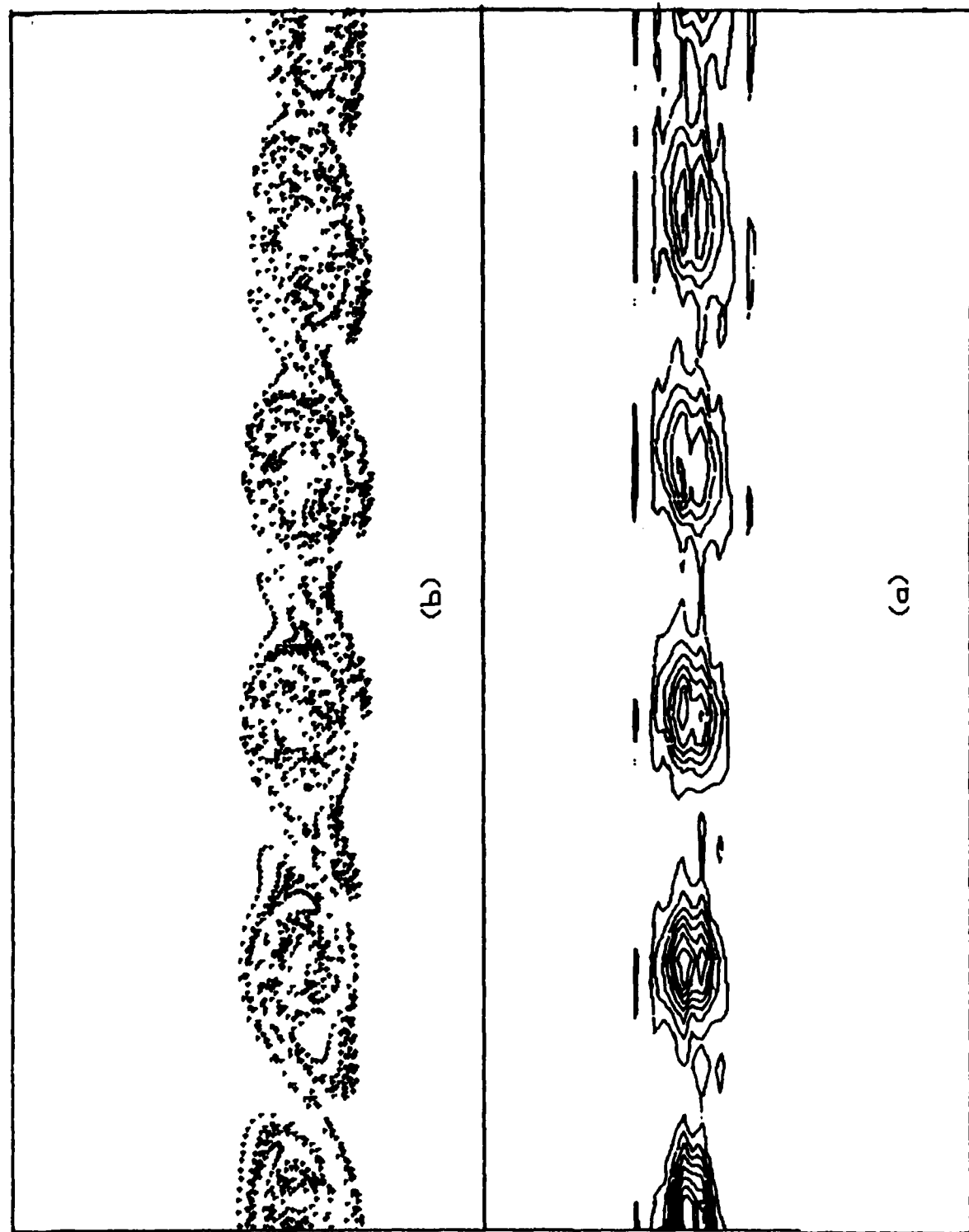
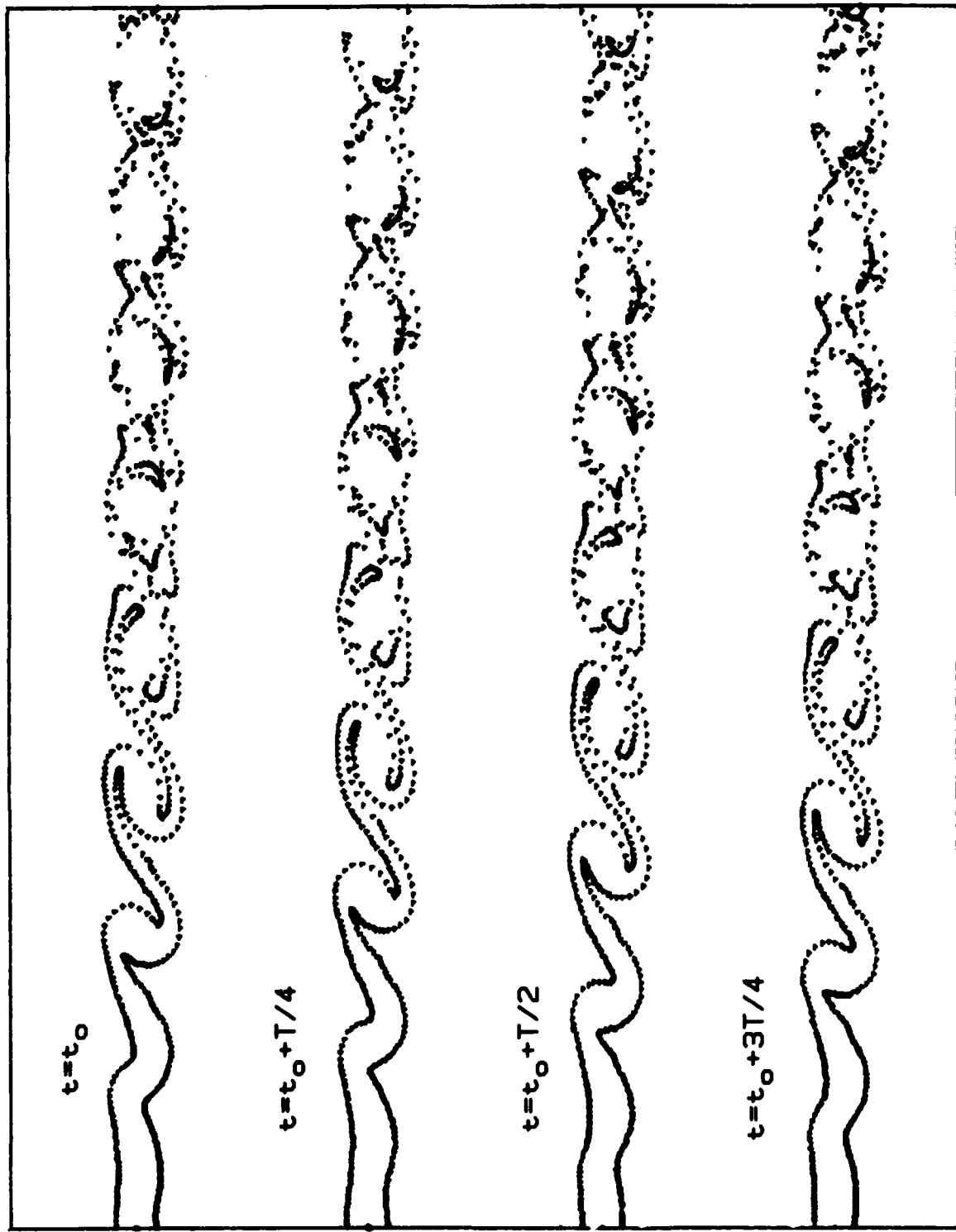


Fig. 5.2.4



X [mm]

Fig. 5.2.5

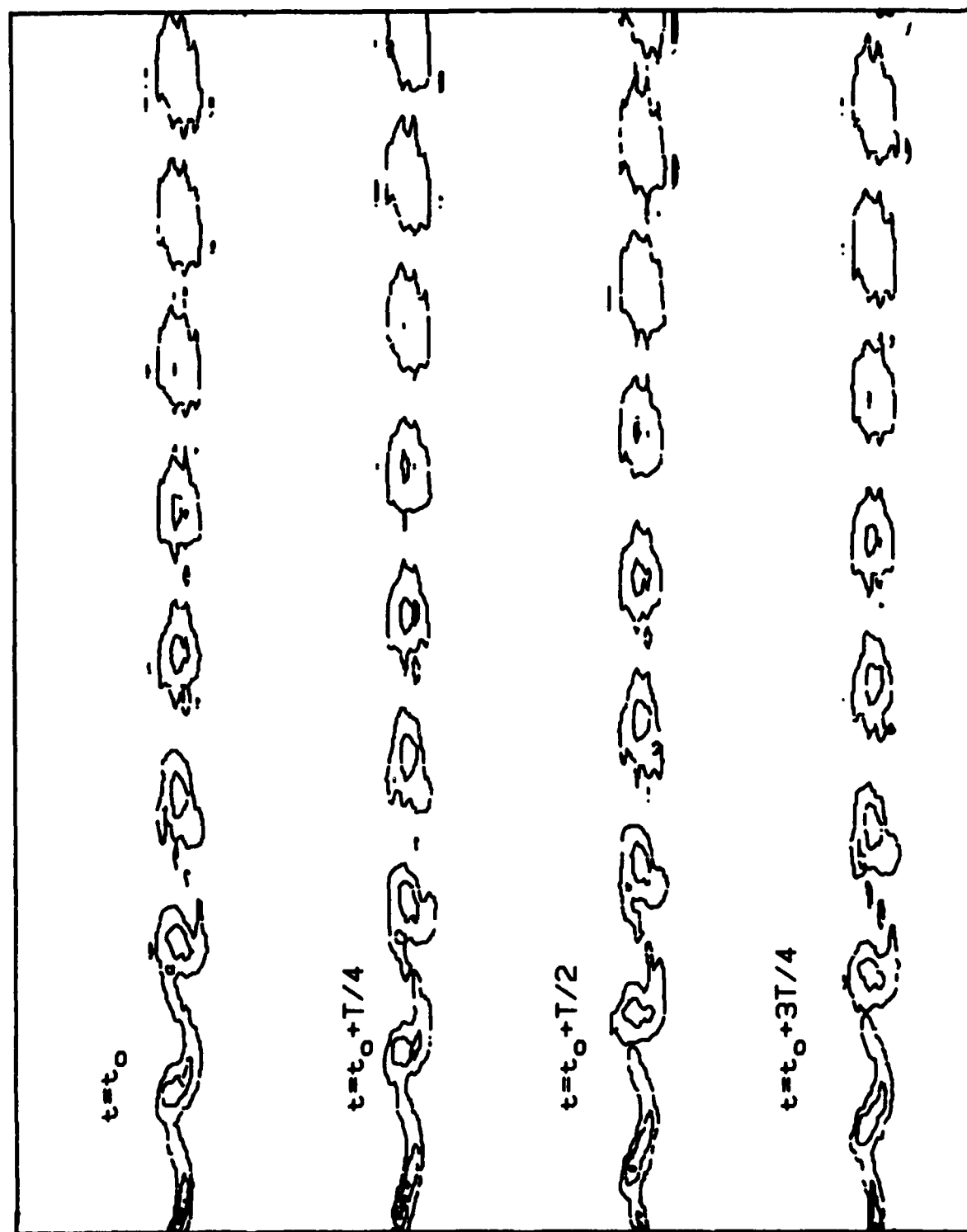


200

1780

X [mm]

Fig. 5.2.6



200

1780

X [mm]

Fig. 5.2.7

3.85
x10⁻²

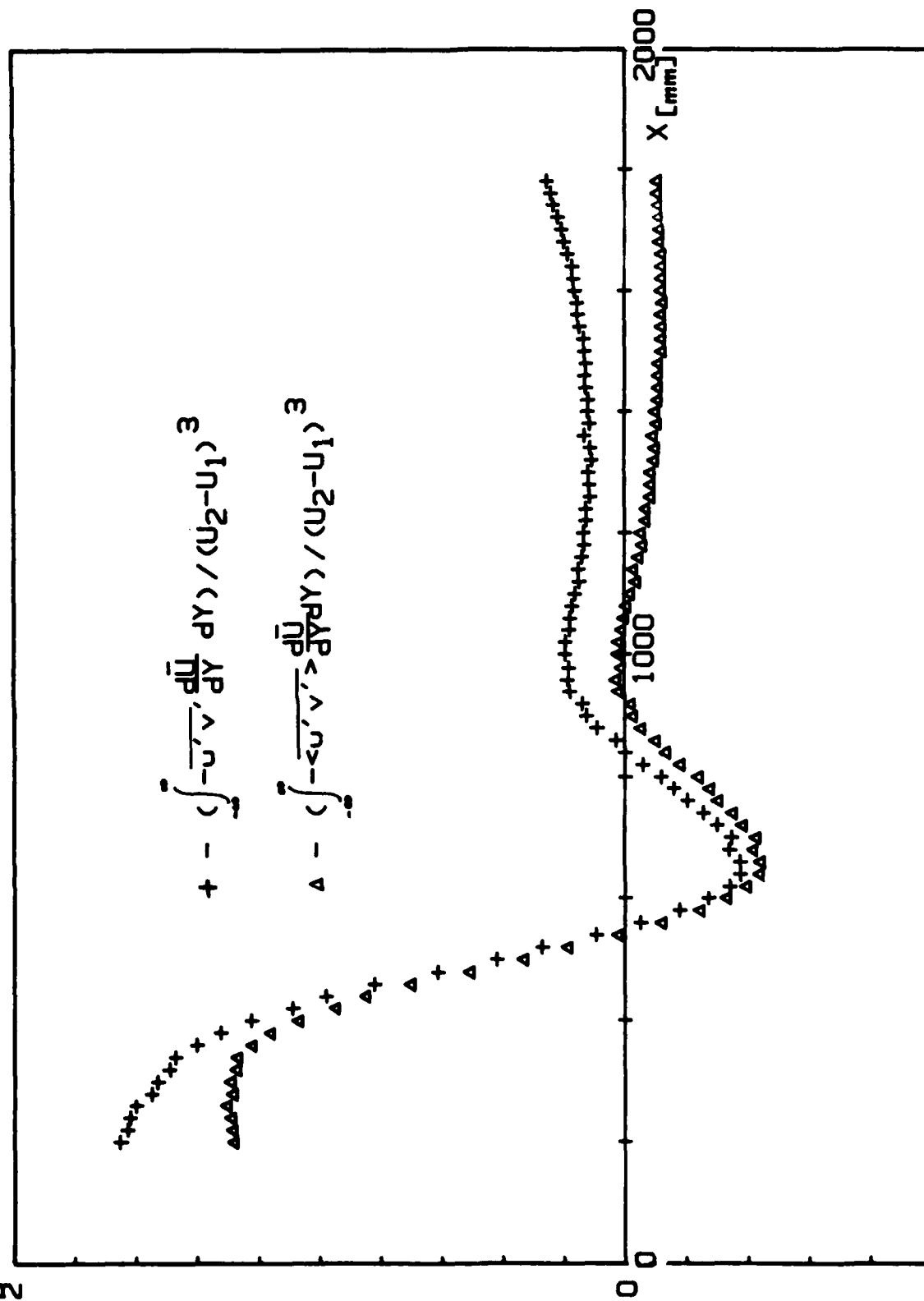


Fig. 5.3.1

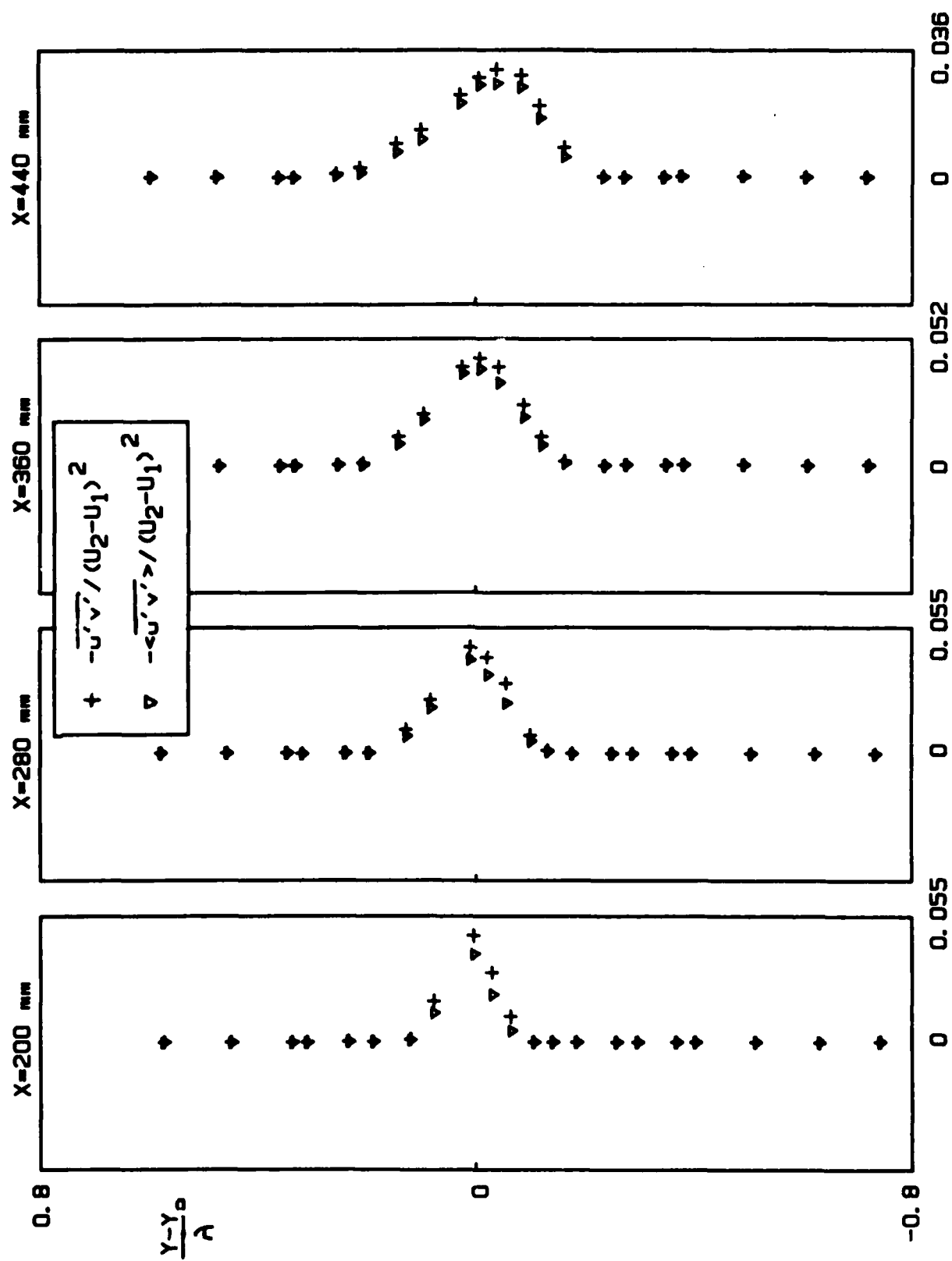


Fig. 5.3.2

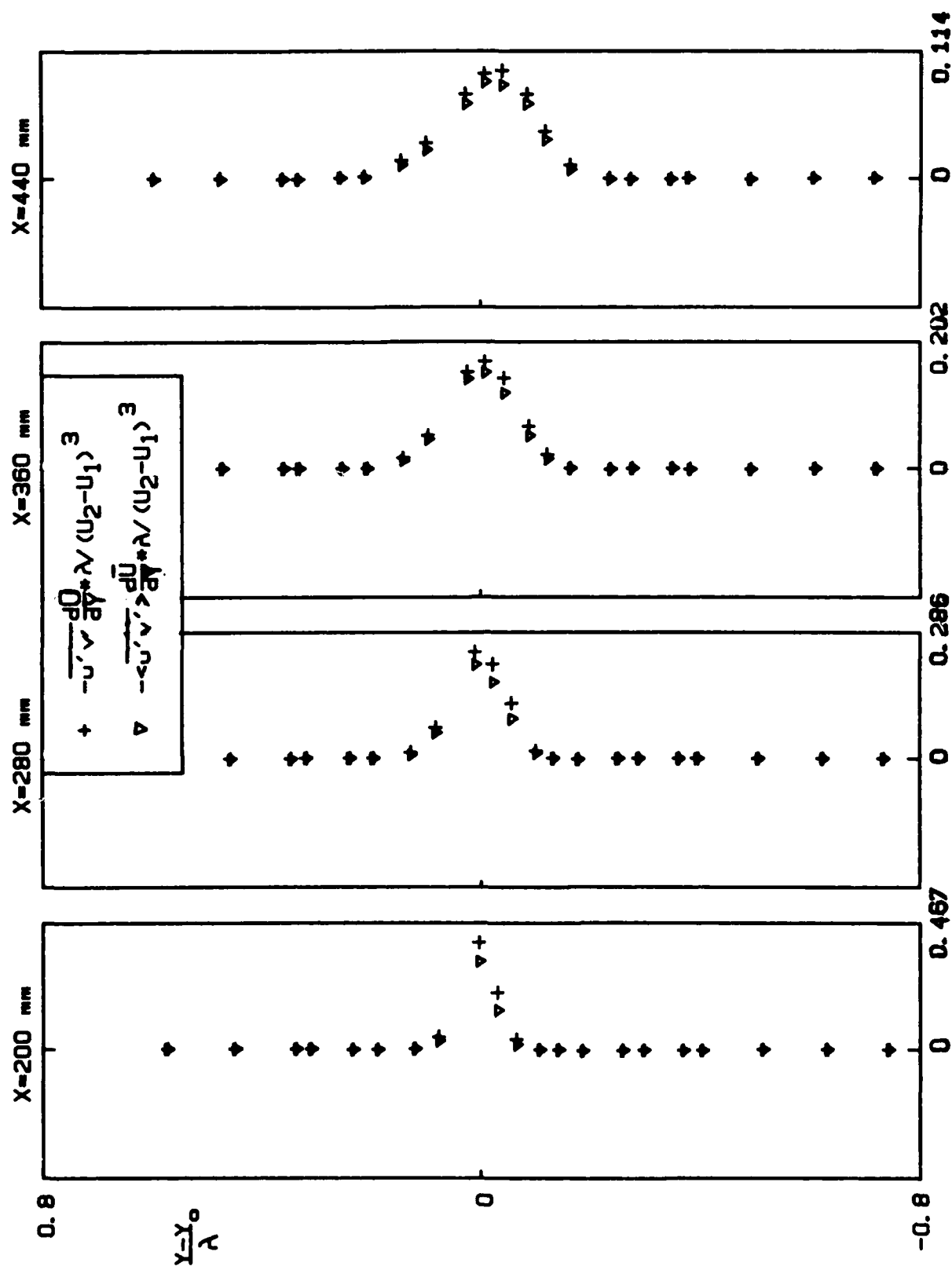


Fig. 5.3.3

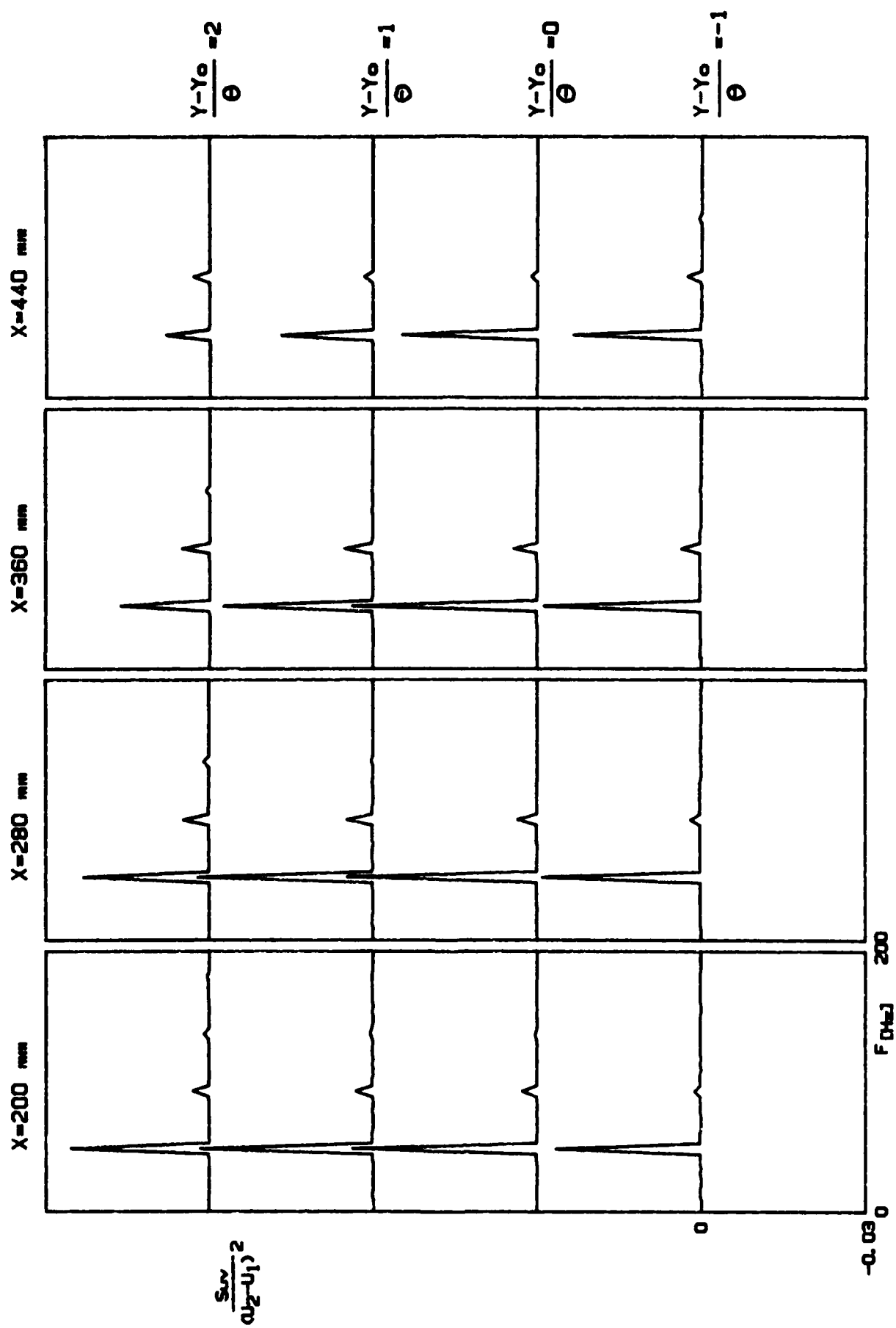


Fig. 5.3.4

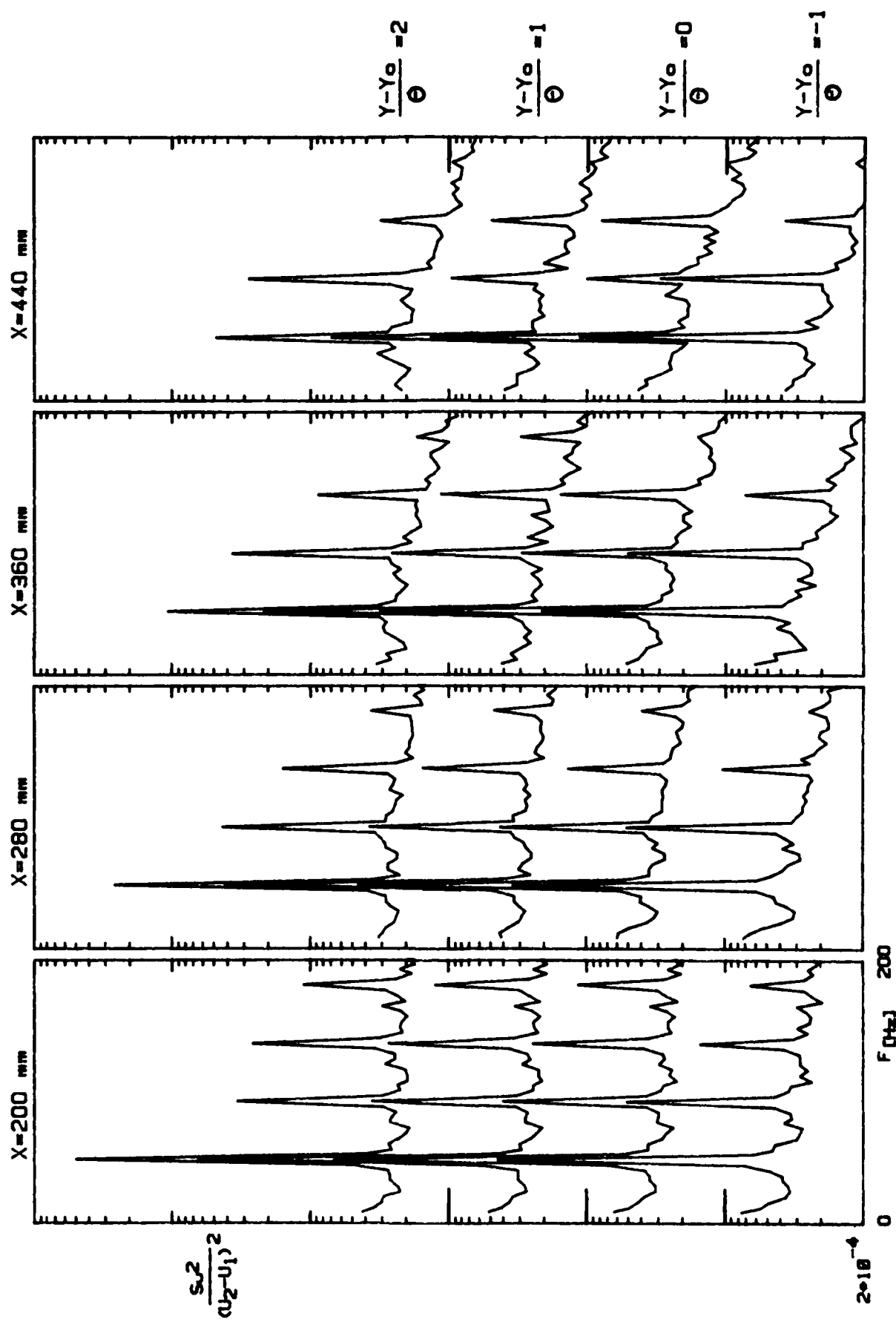


Fig. 5.3.5

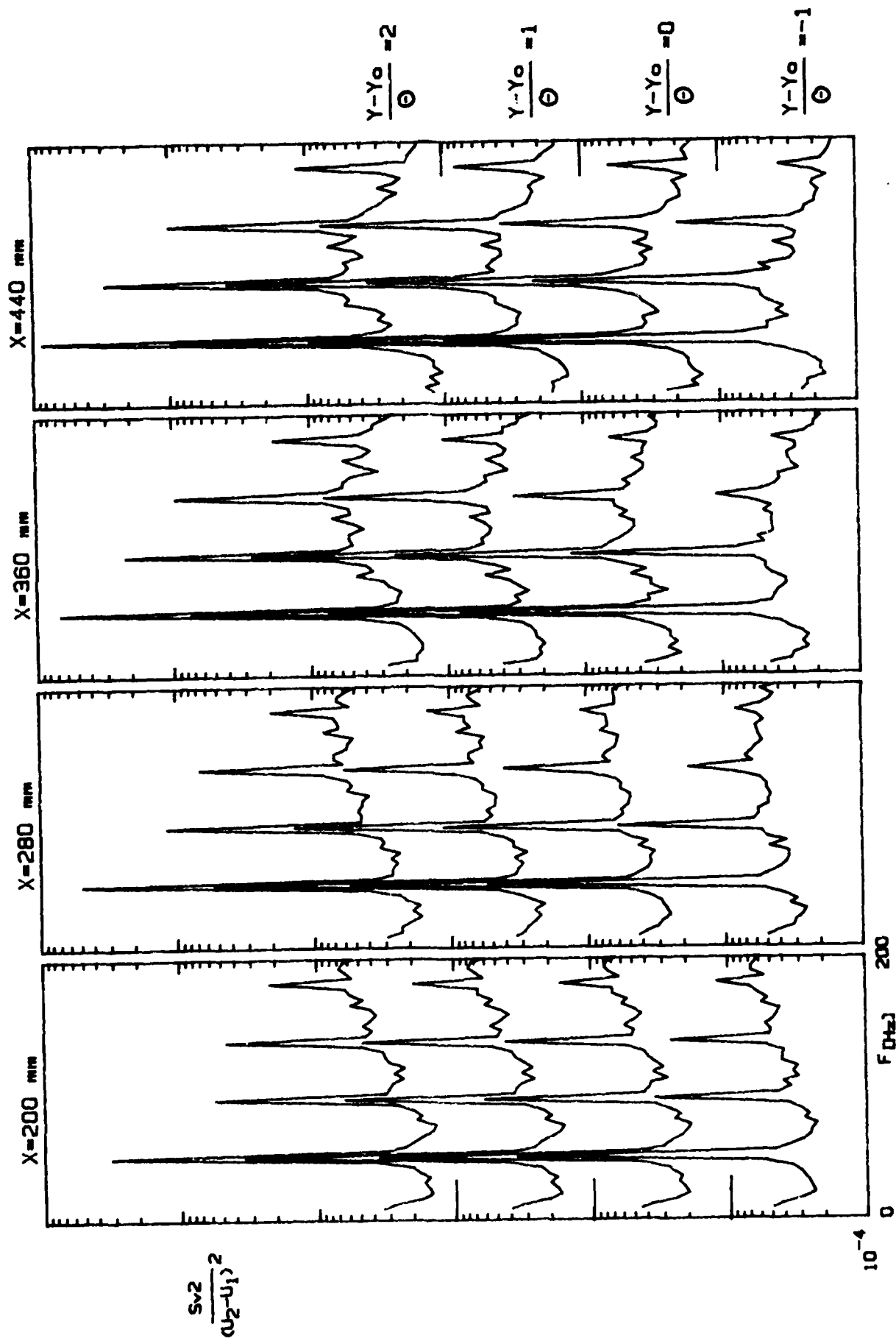


Fig. 5.3.6

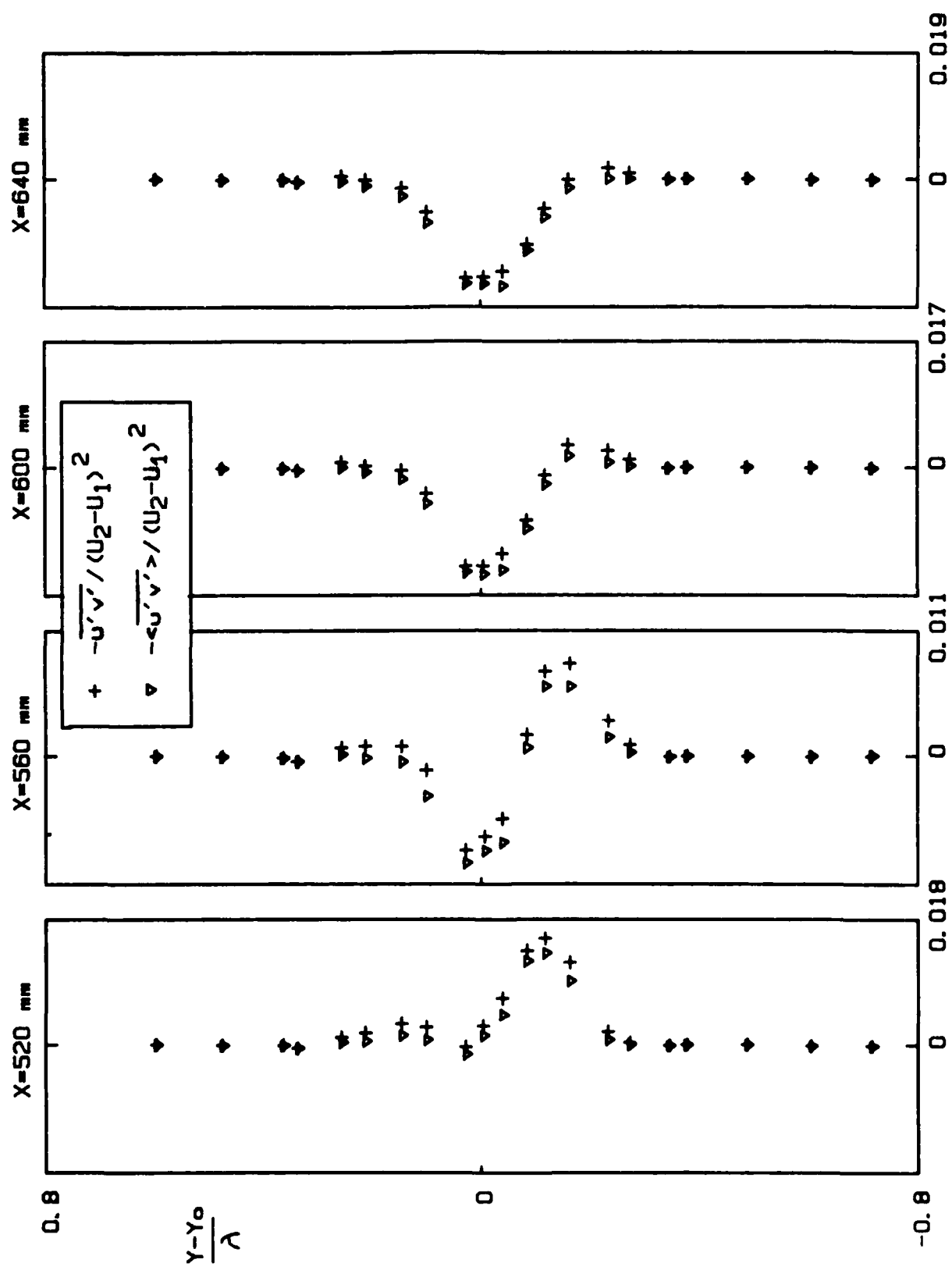


Fig. 5.3.7

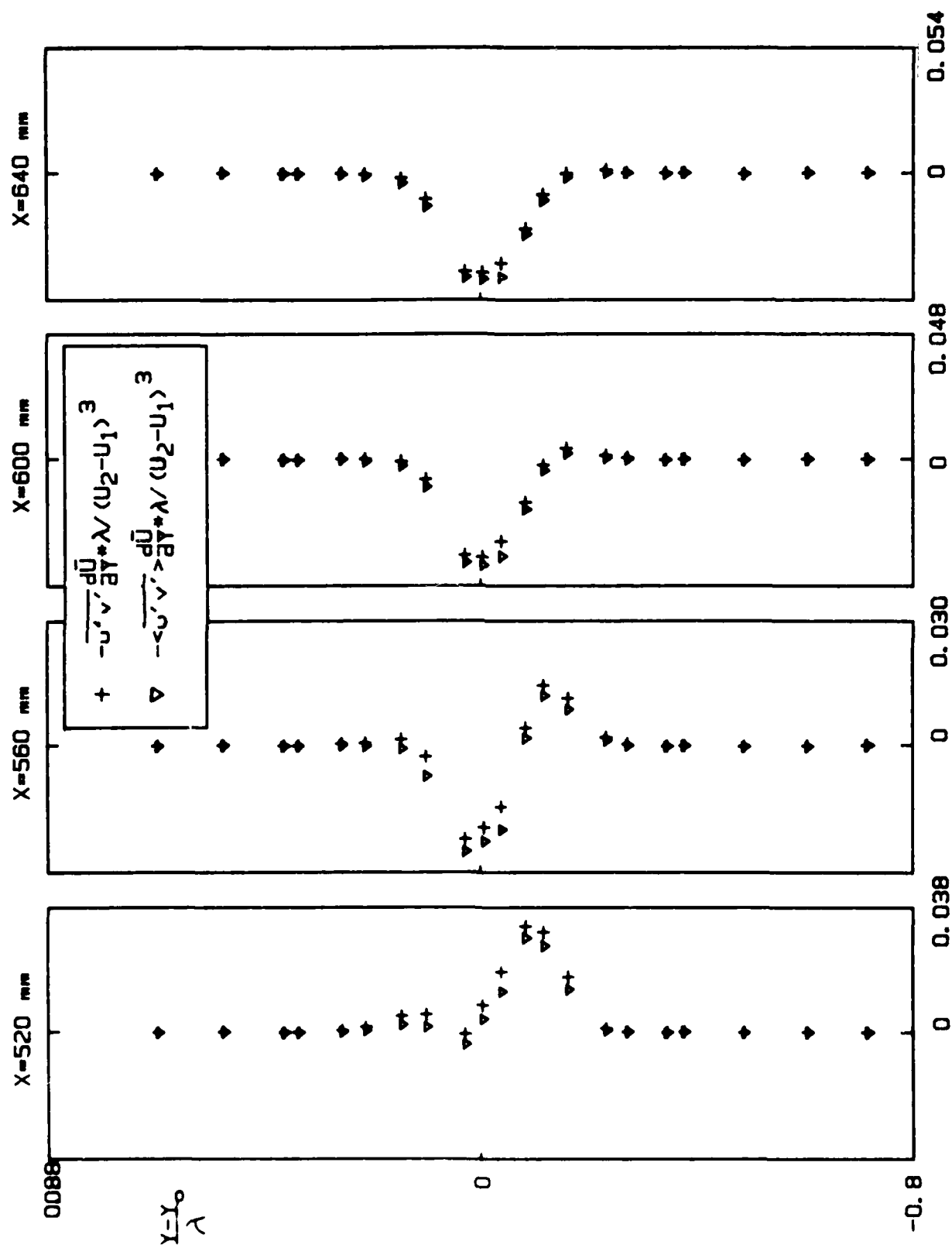


Fig. 5.3.8

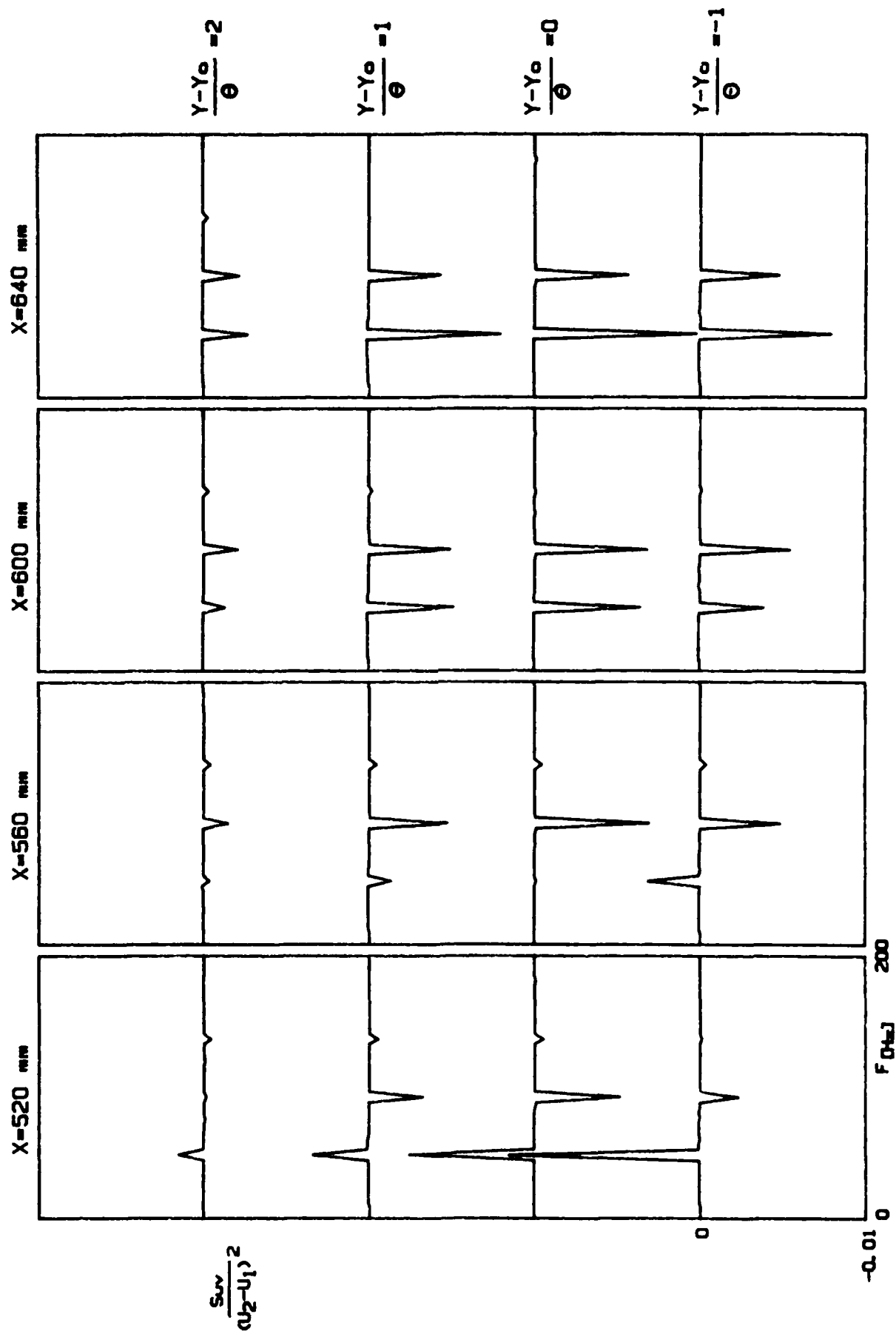


Fig. 5.3.9

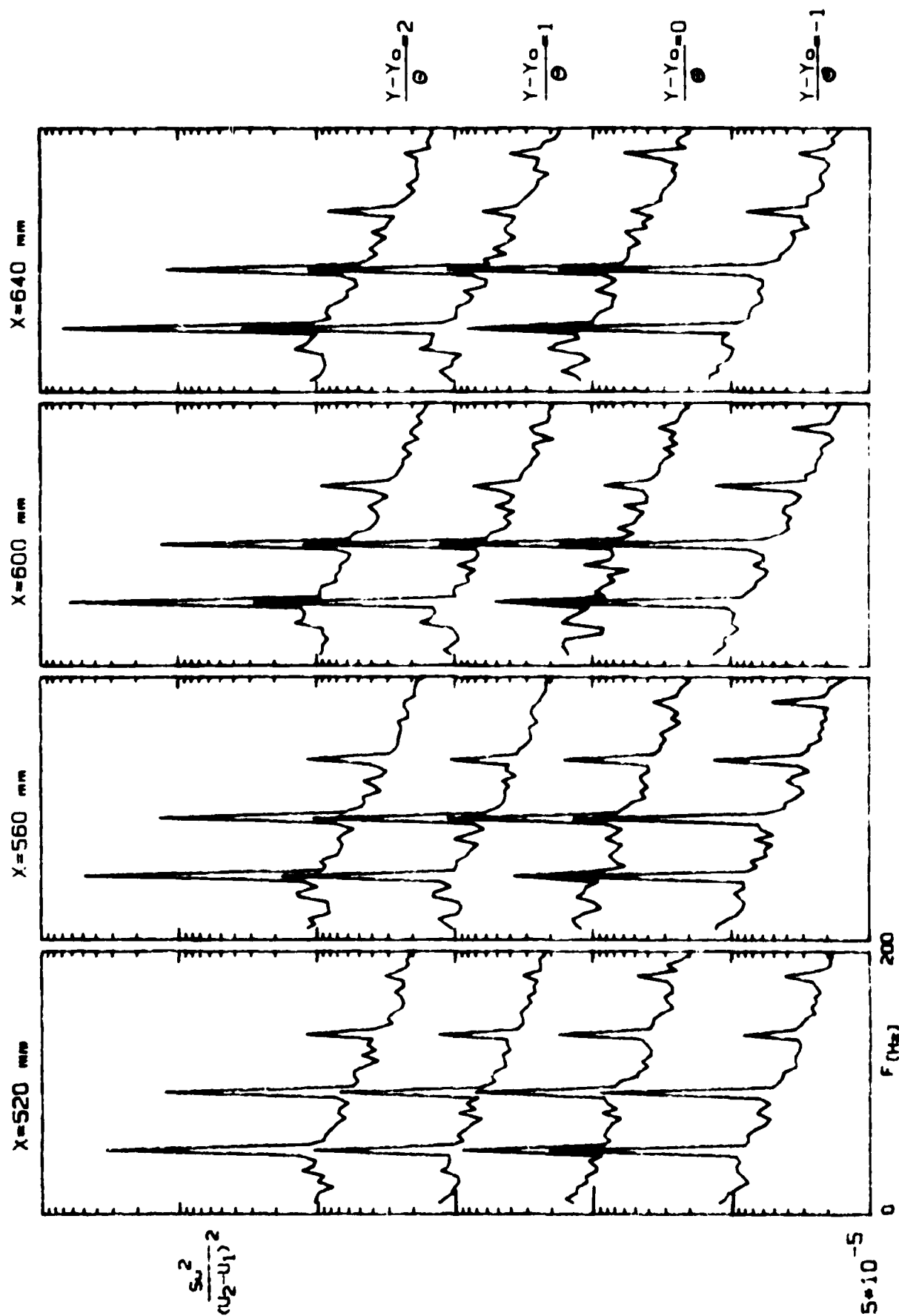


Fig. 5.3.10

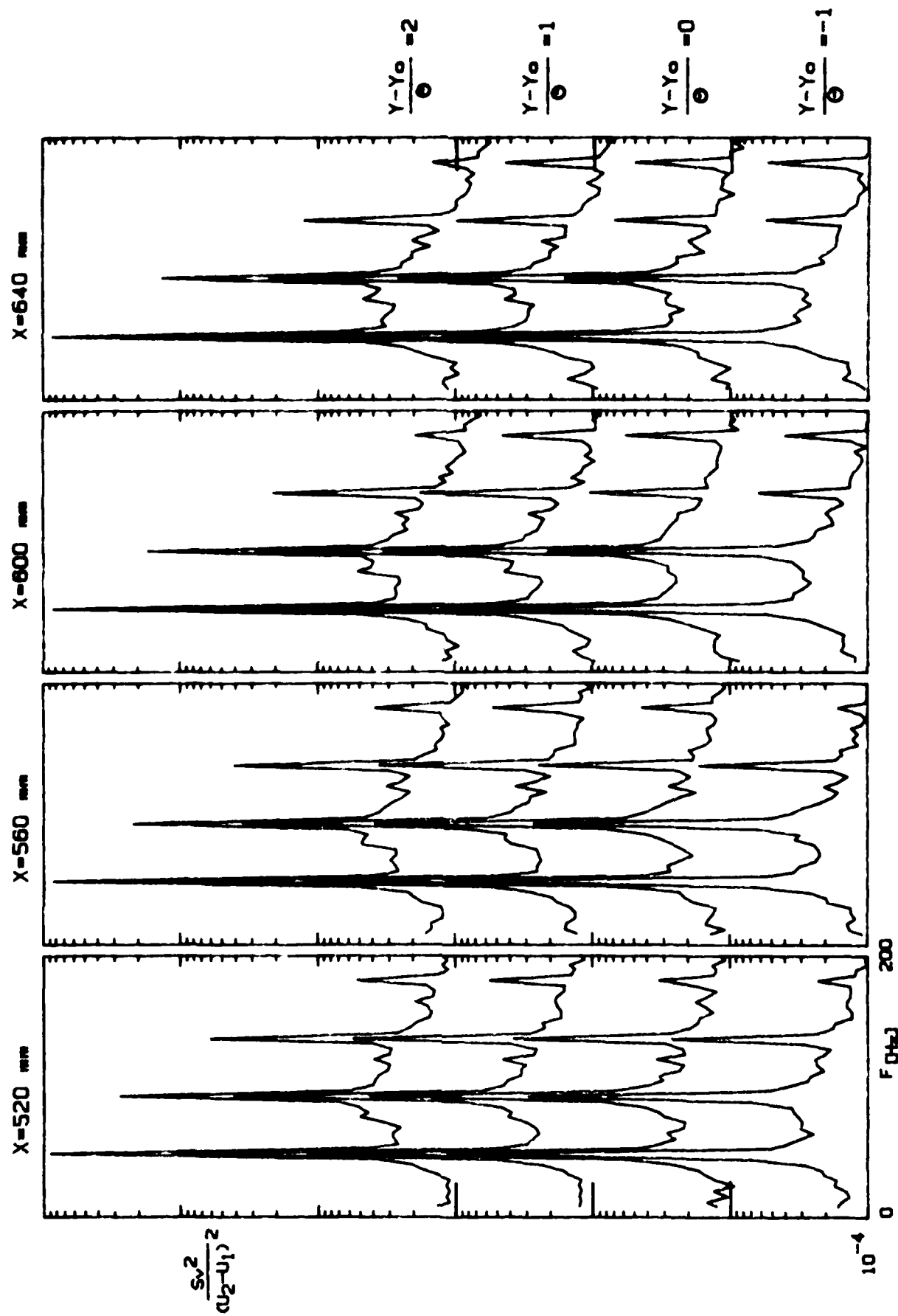


Fig. 5.3.11

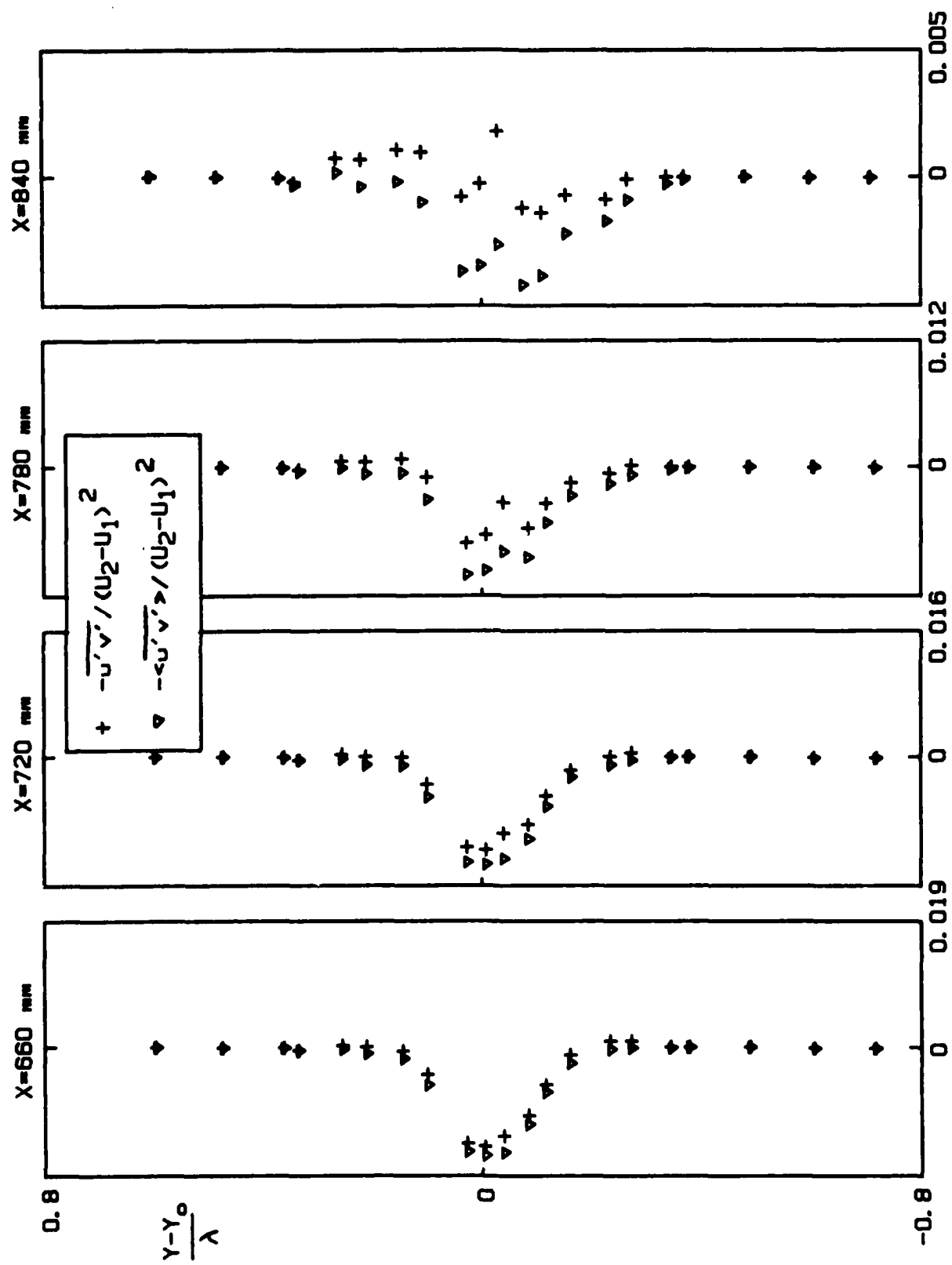


Fig. 5.3.12

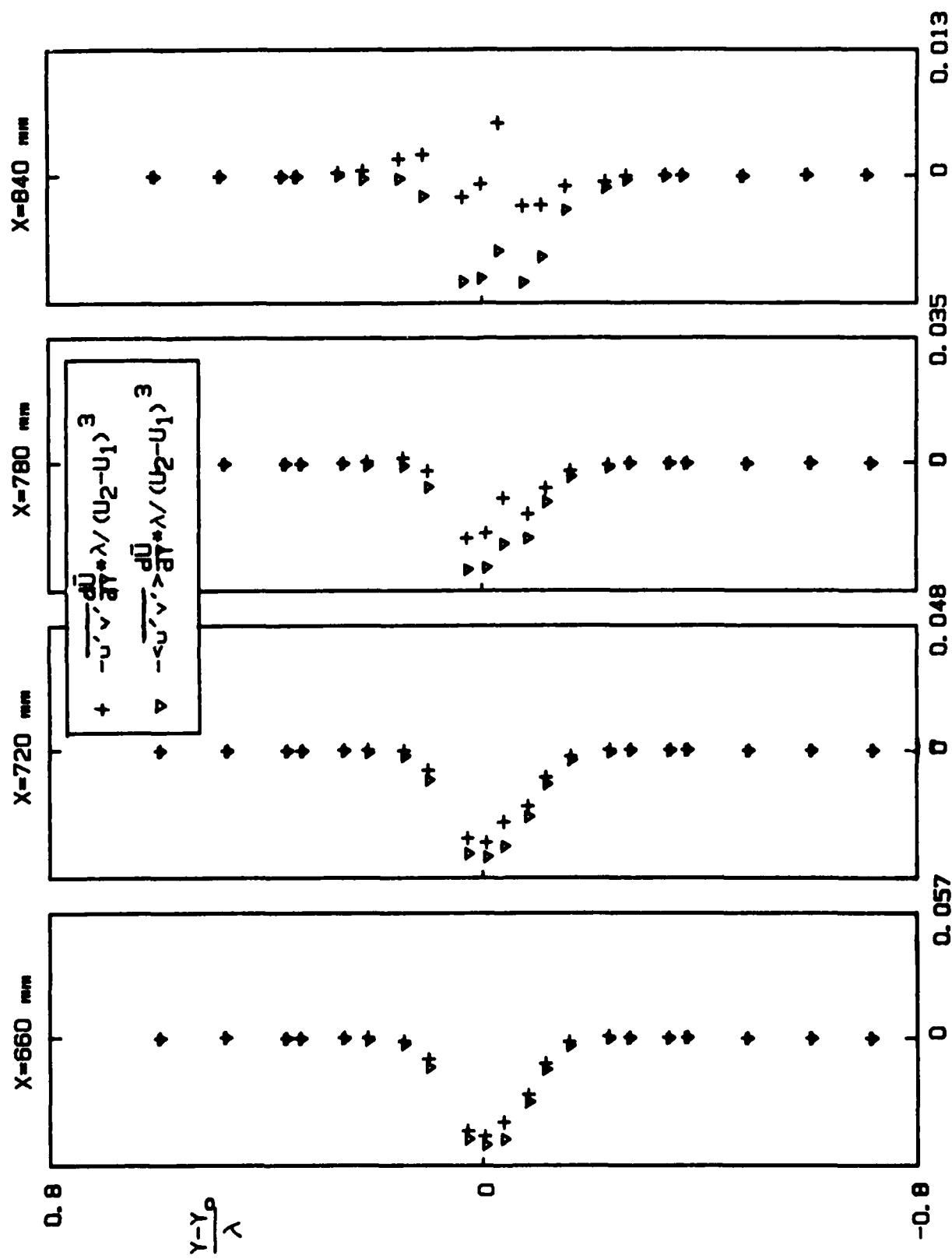


Fig. 5.3.13

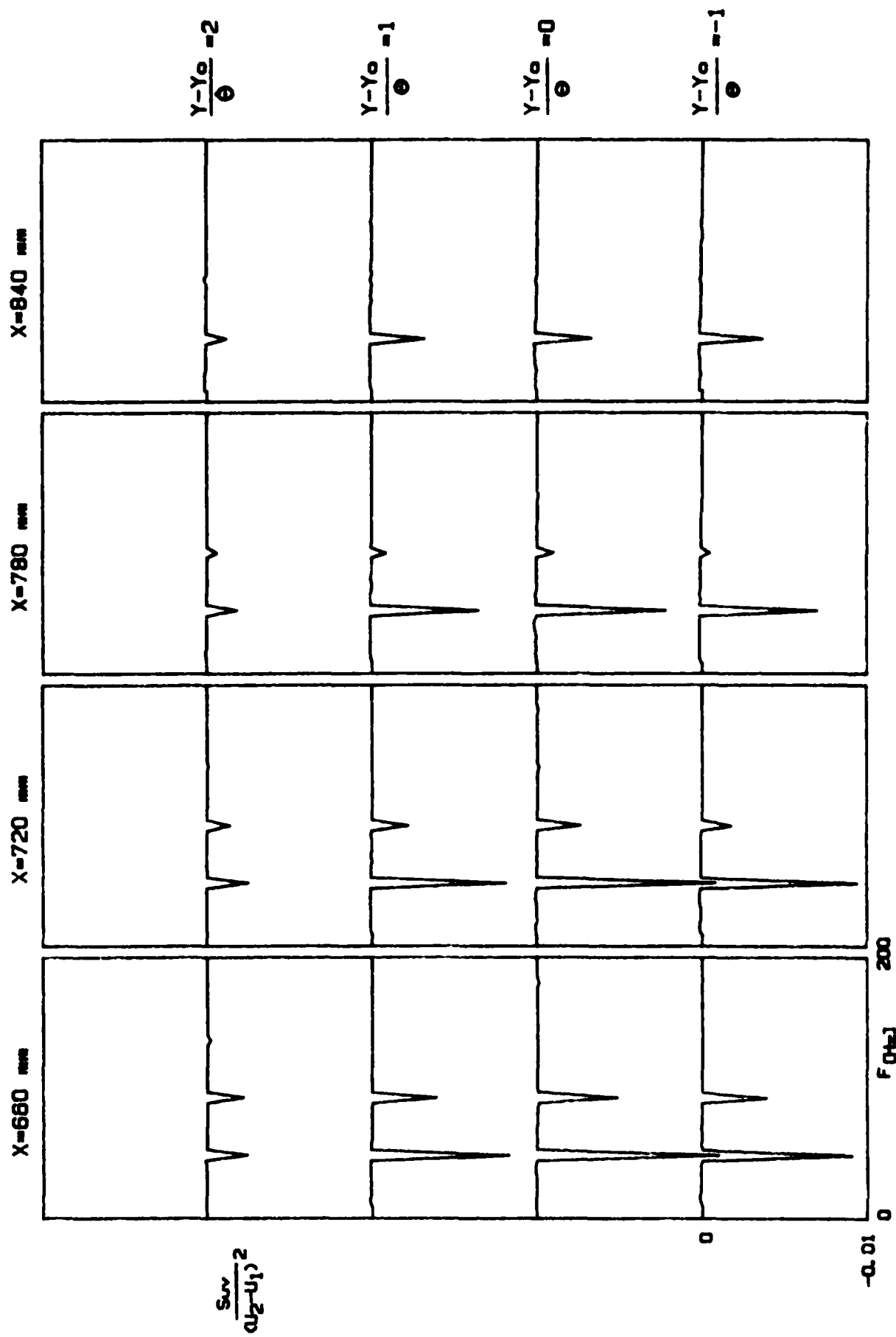


Fig. 5.3.14

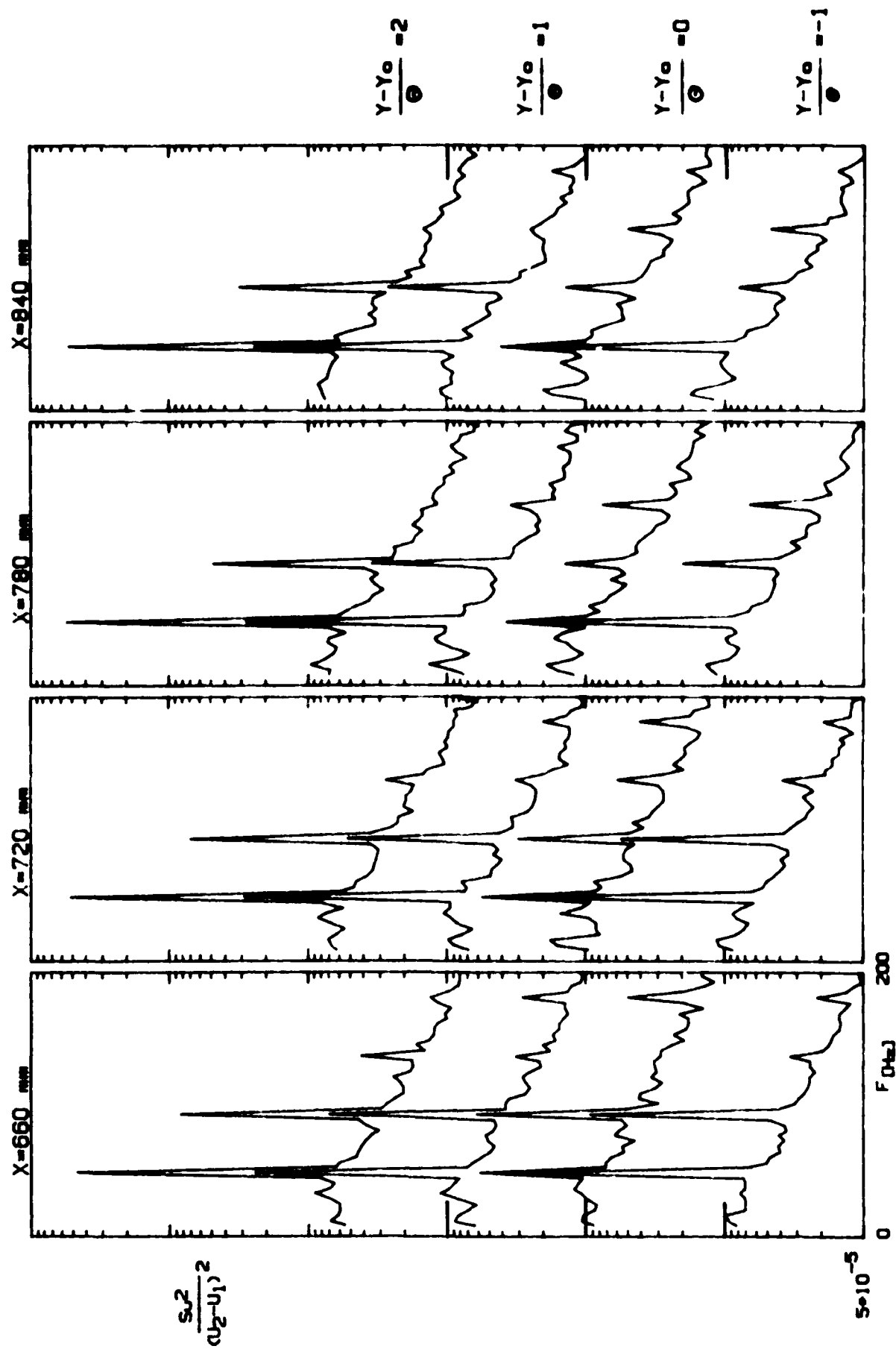


Fig. 5.3.15

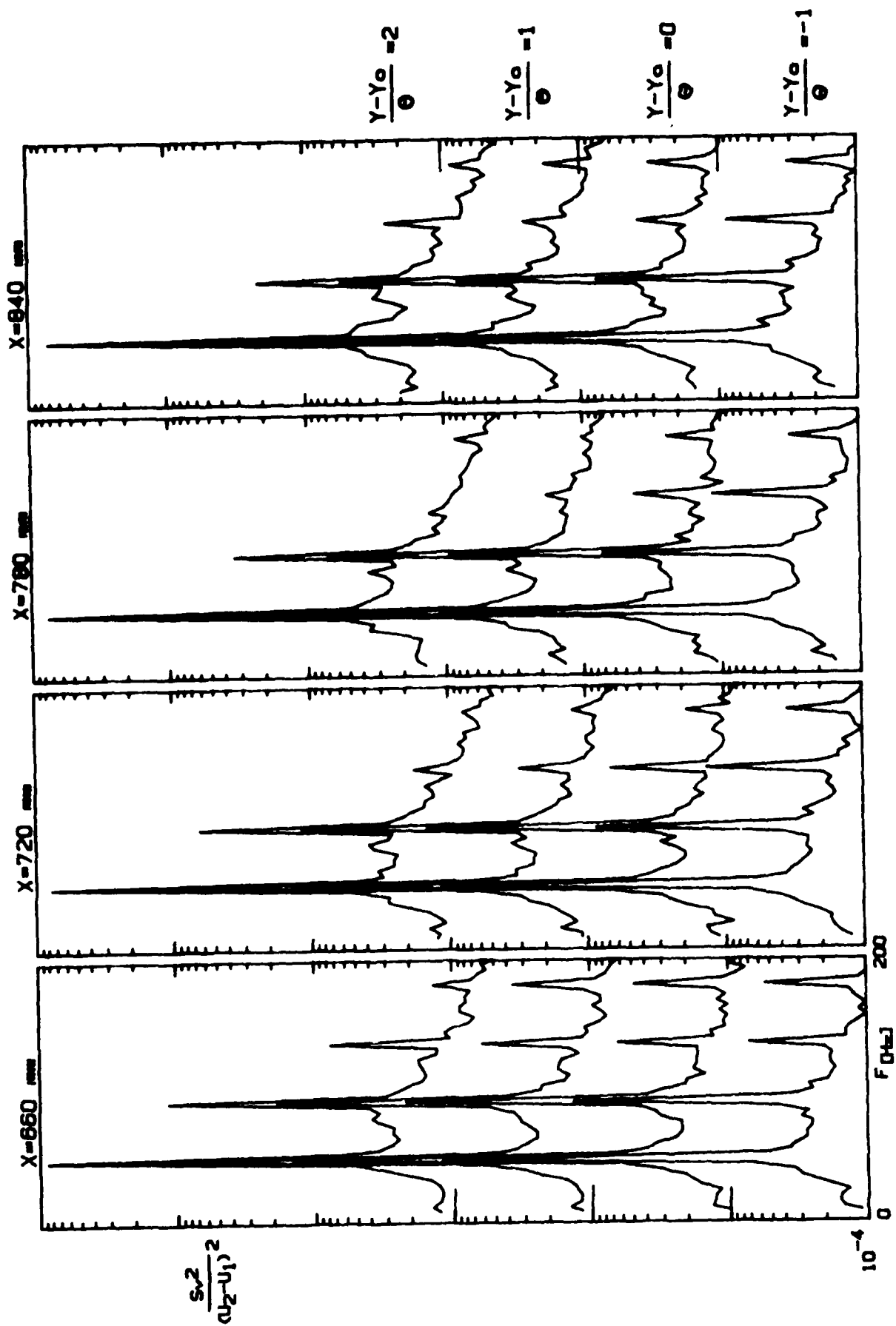


Fig. 5.3.16

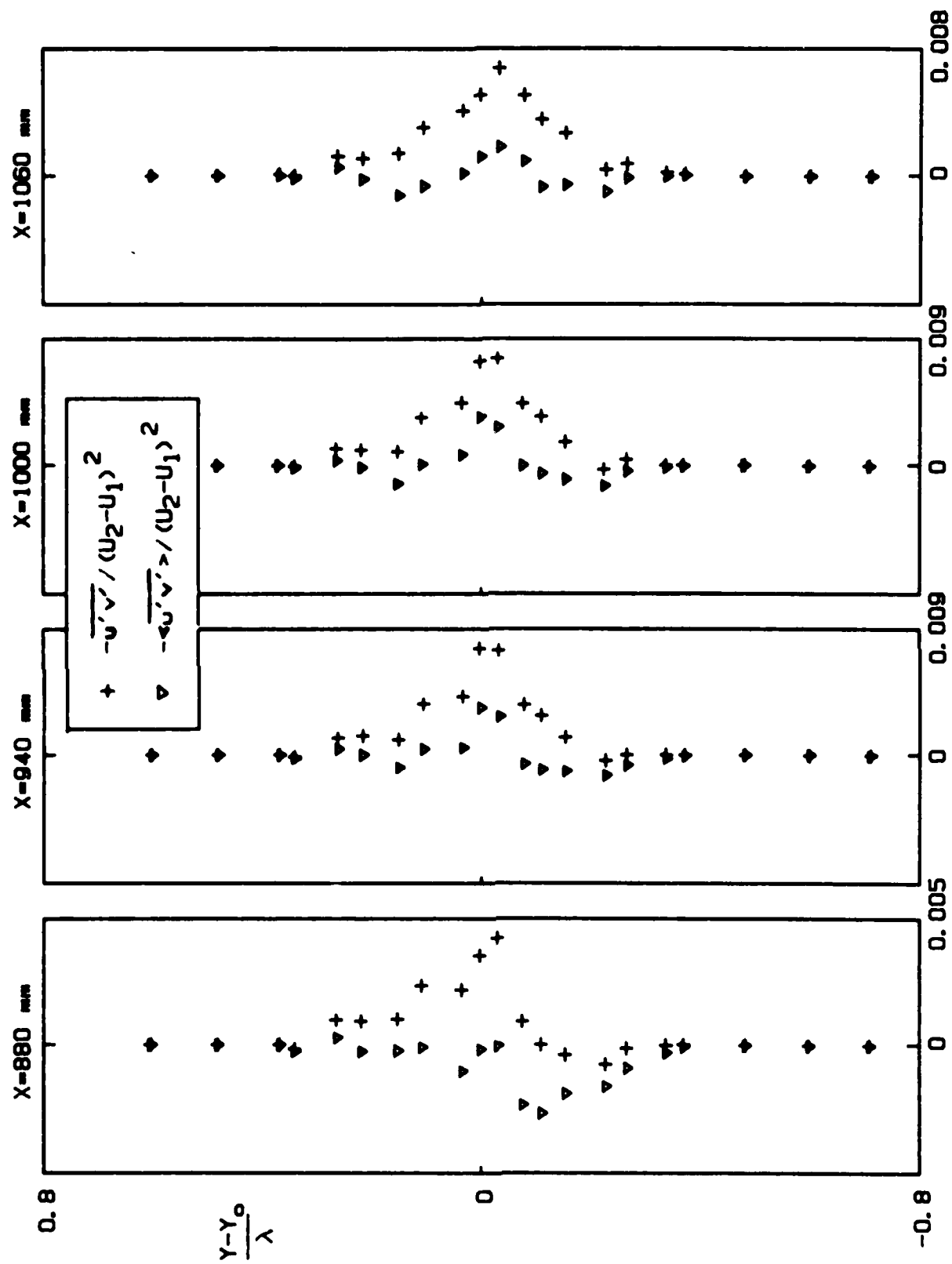


Fig. 5.3.17

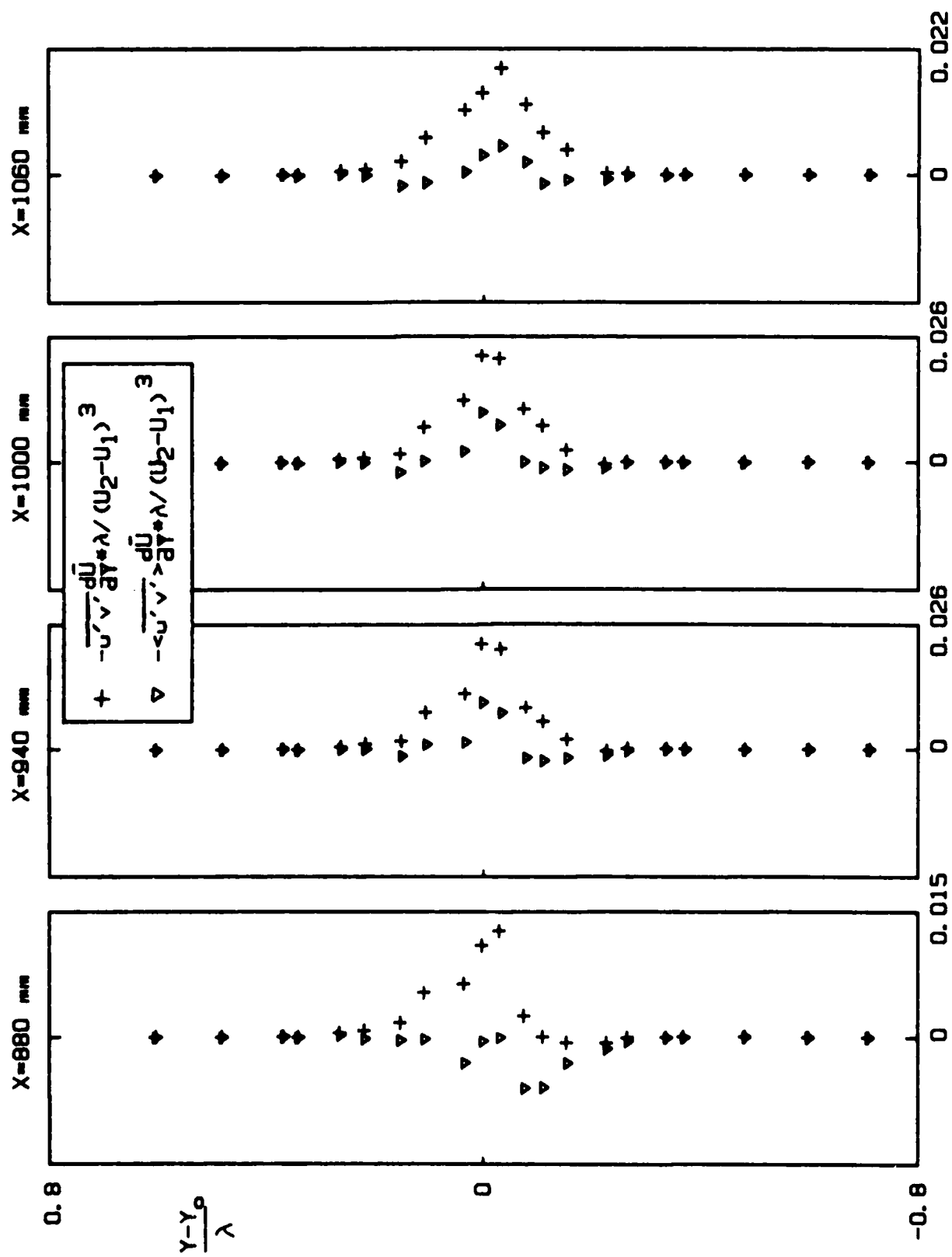


Fig. 5.3.18

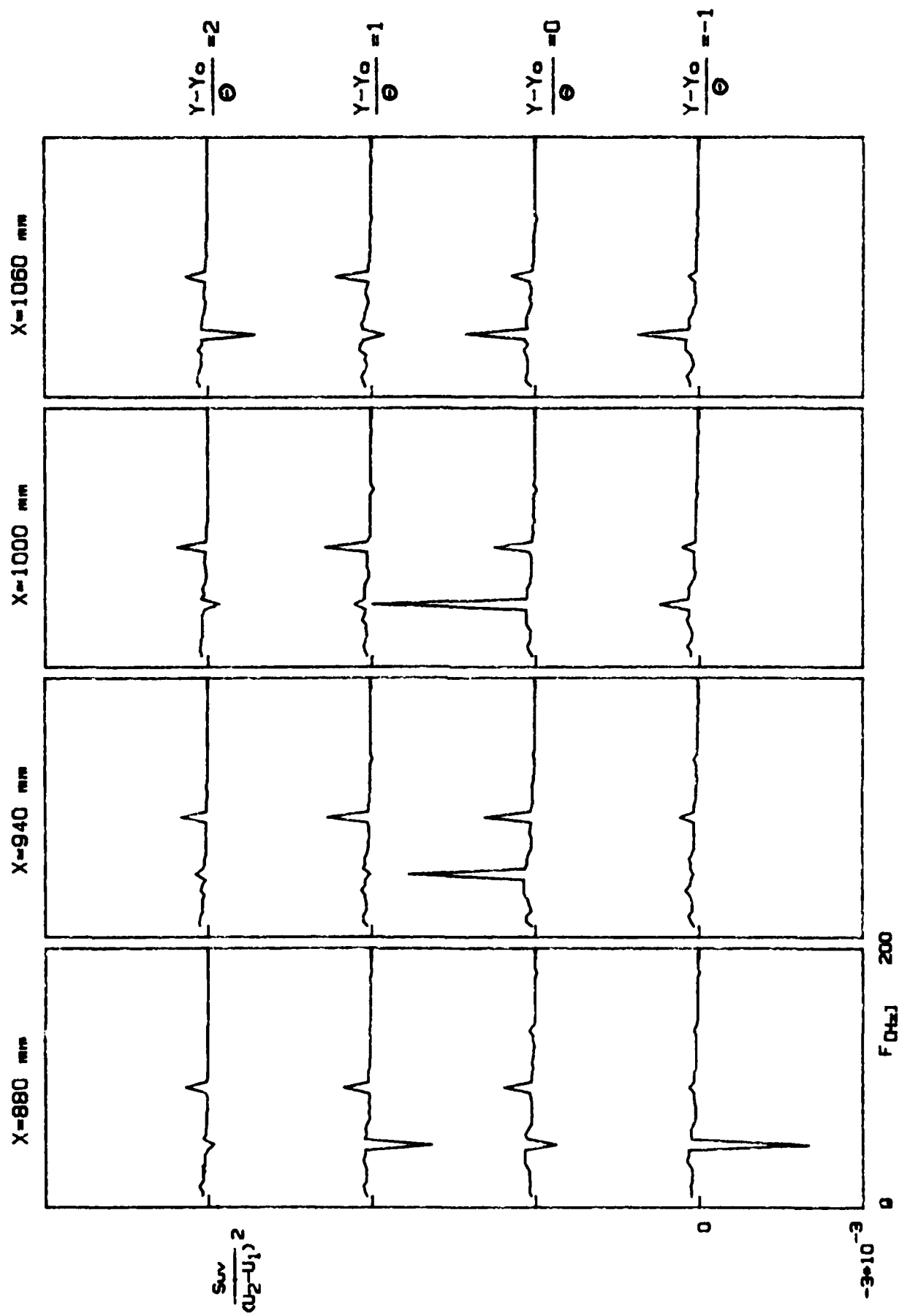


Fig. 5.3.19

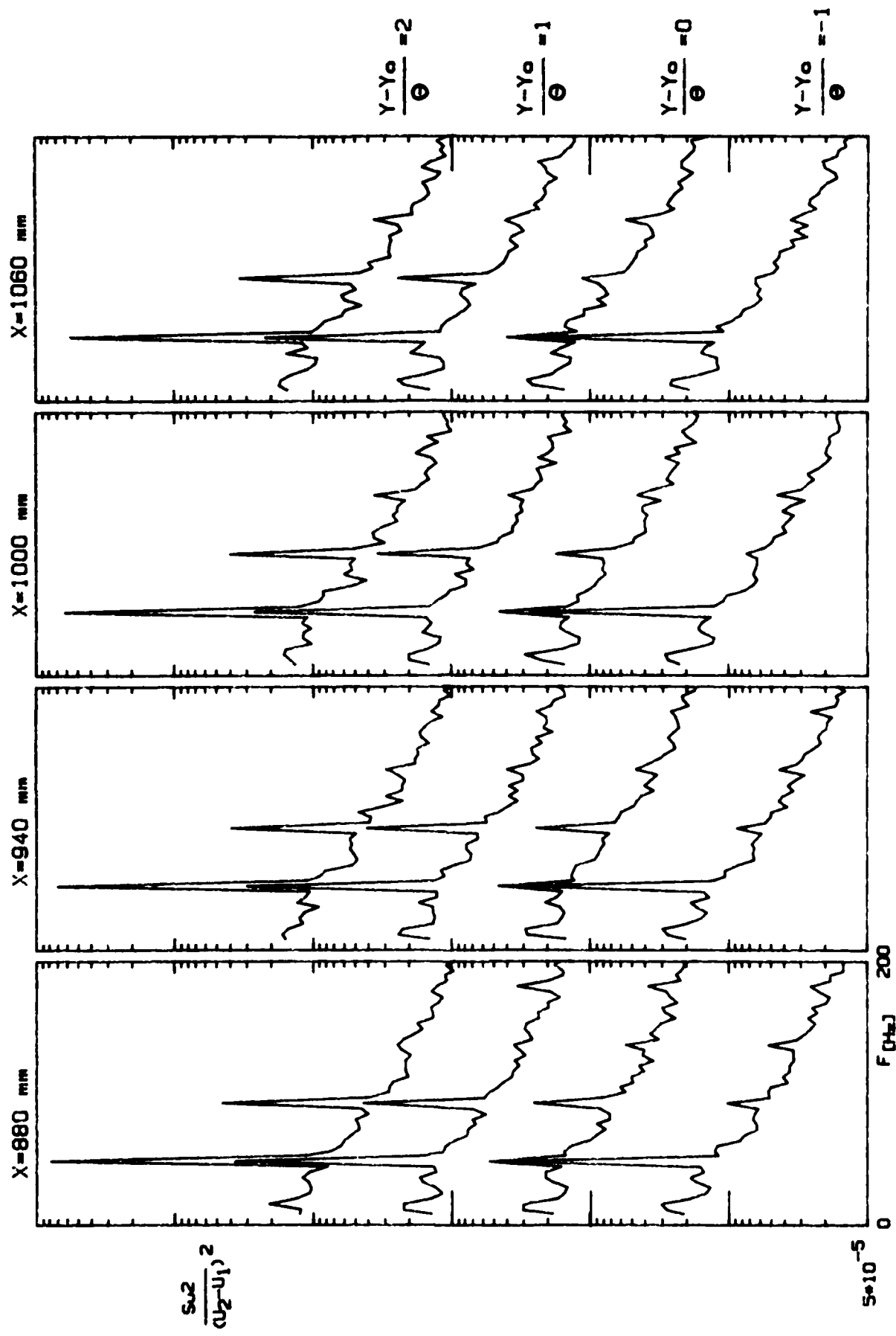


Fig. 5.3.20

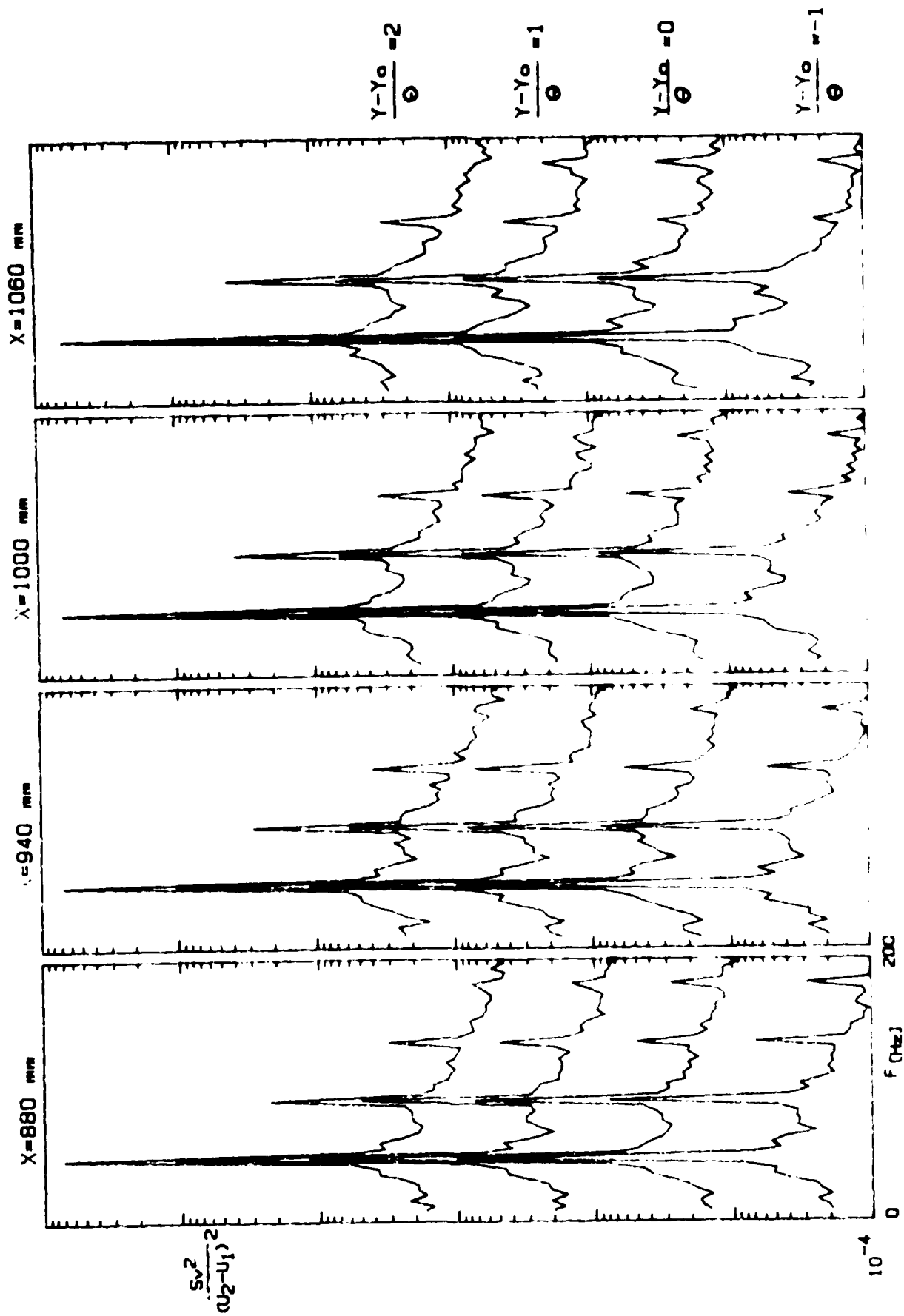


Fig. 5.3.21

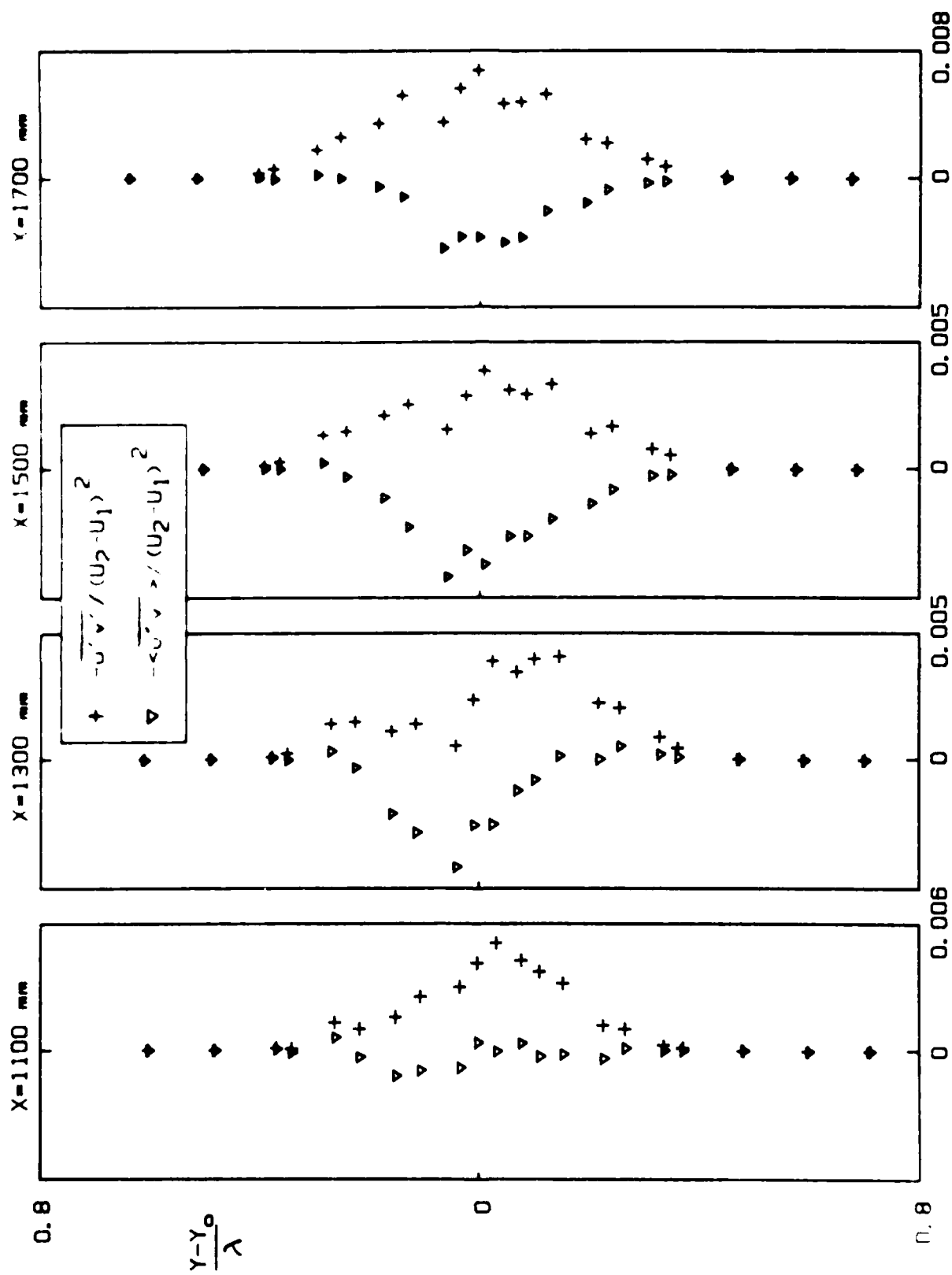


Fig. 5.3.22

AD-A179 717

A HIGHLY EXCITED TURBULENT MIXING LAYER(U) TEL-AVIV
UNIV (ISRAEL) DEPT OF FLUID MECHANICS AND HEAT TRANSFER
I WEISBROT ET AL. NOV 84 AE-84-2 AFOSR-TR-87-0546

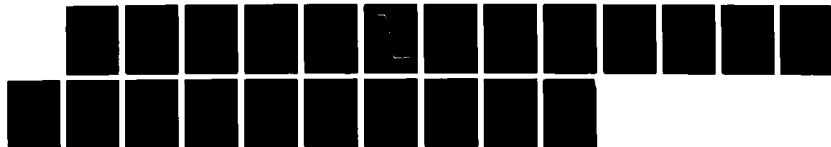
2/2

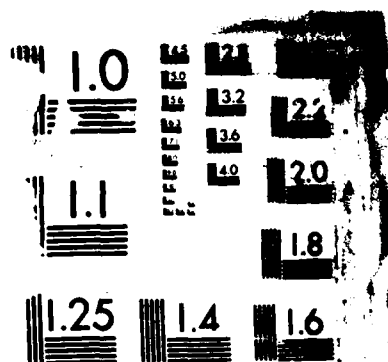
UNCLASSIFIED

AFOSR-82-0235

F/G 20/4

NL





MI

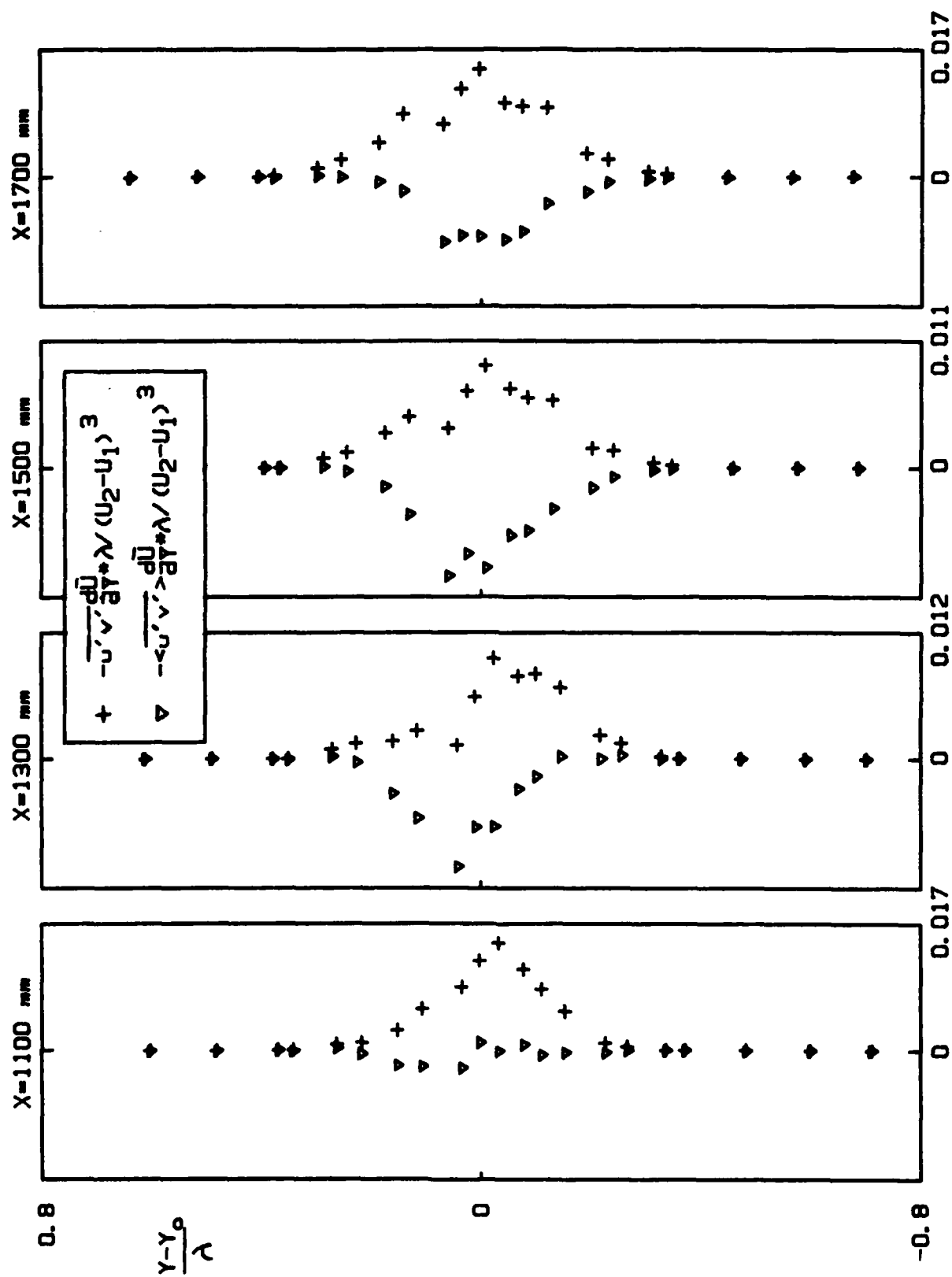


Fig. 5.3.23

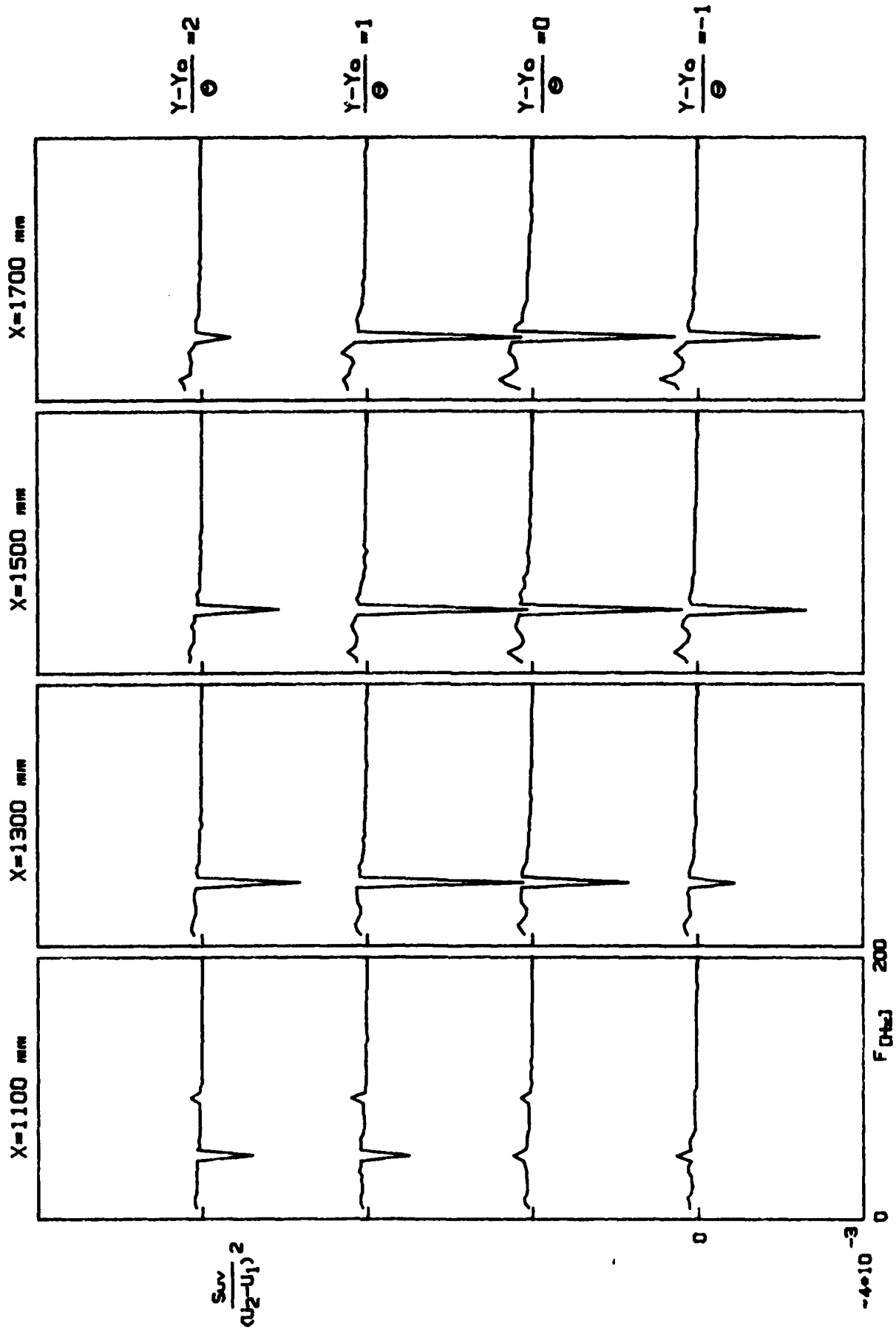


Fig. 5.3.24

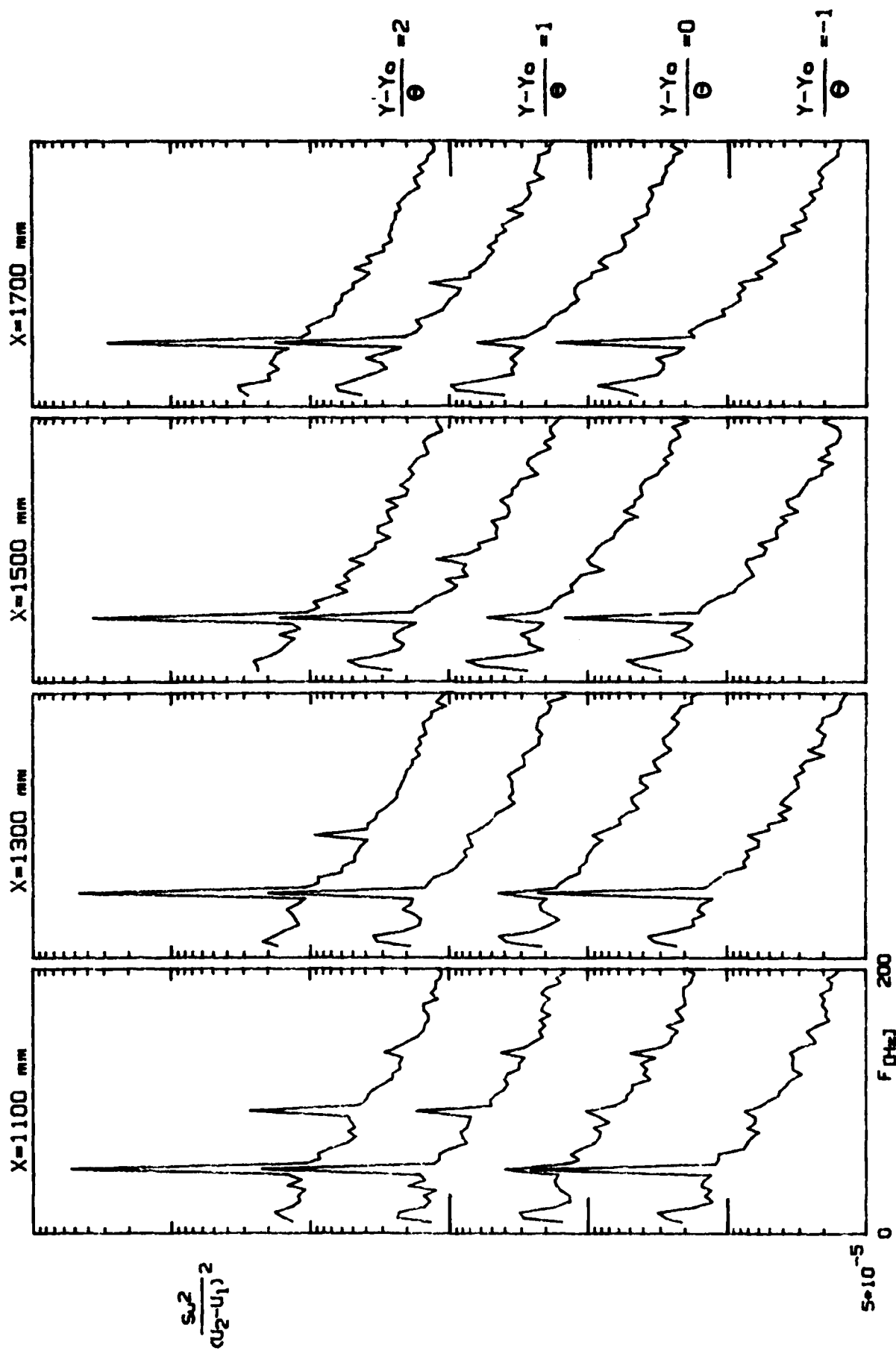


Fig. 5.3.25

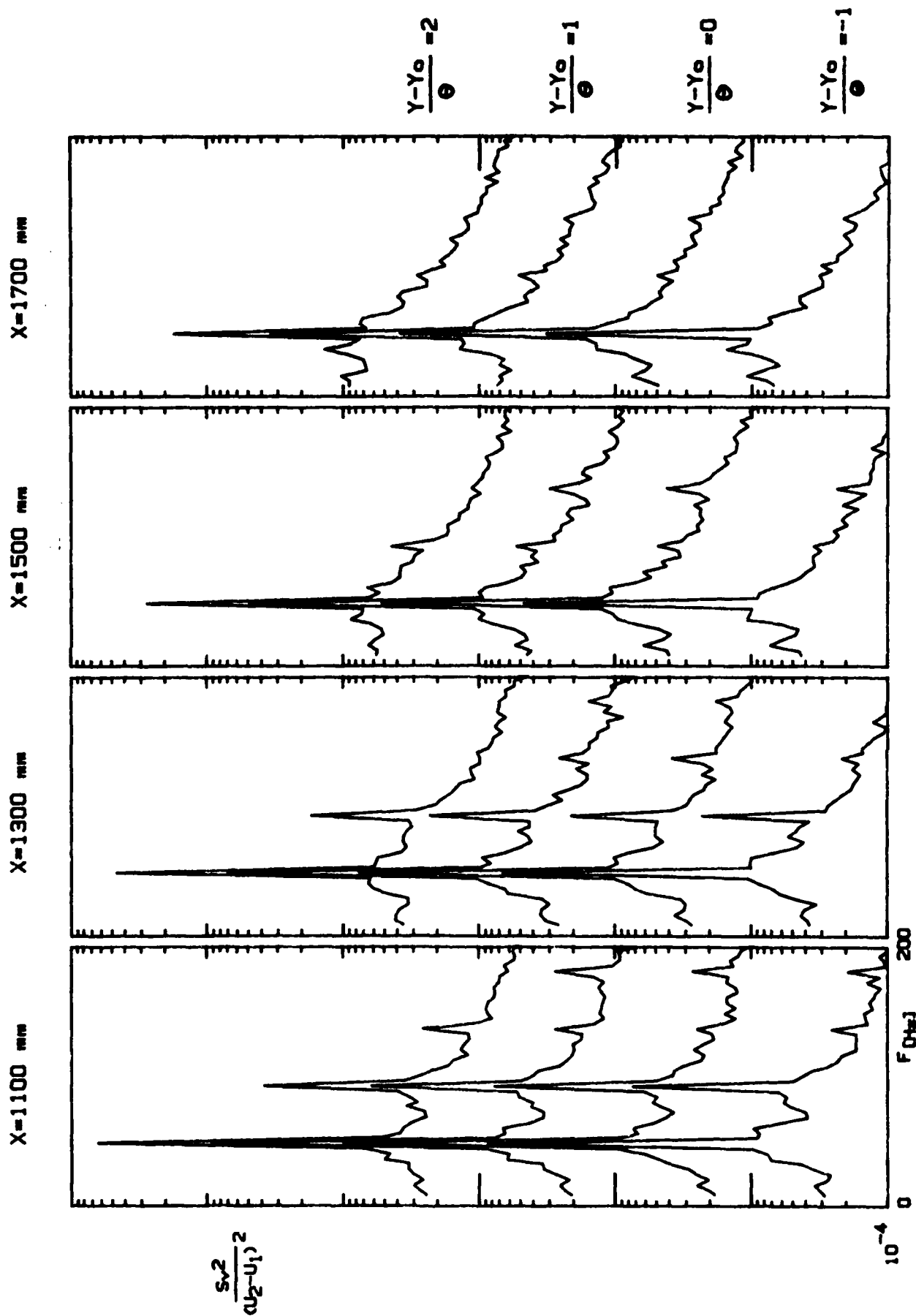


Fig. 5.3.26

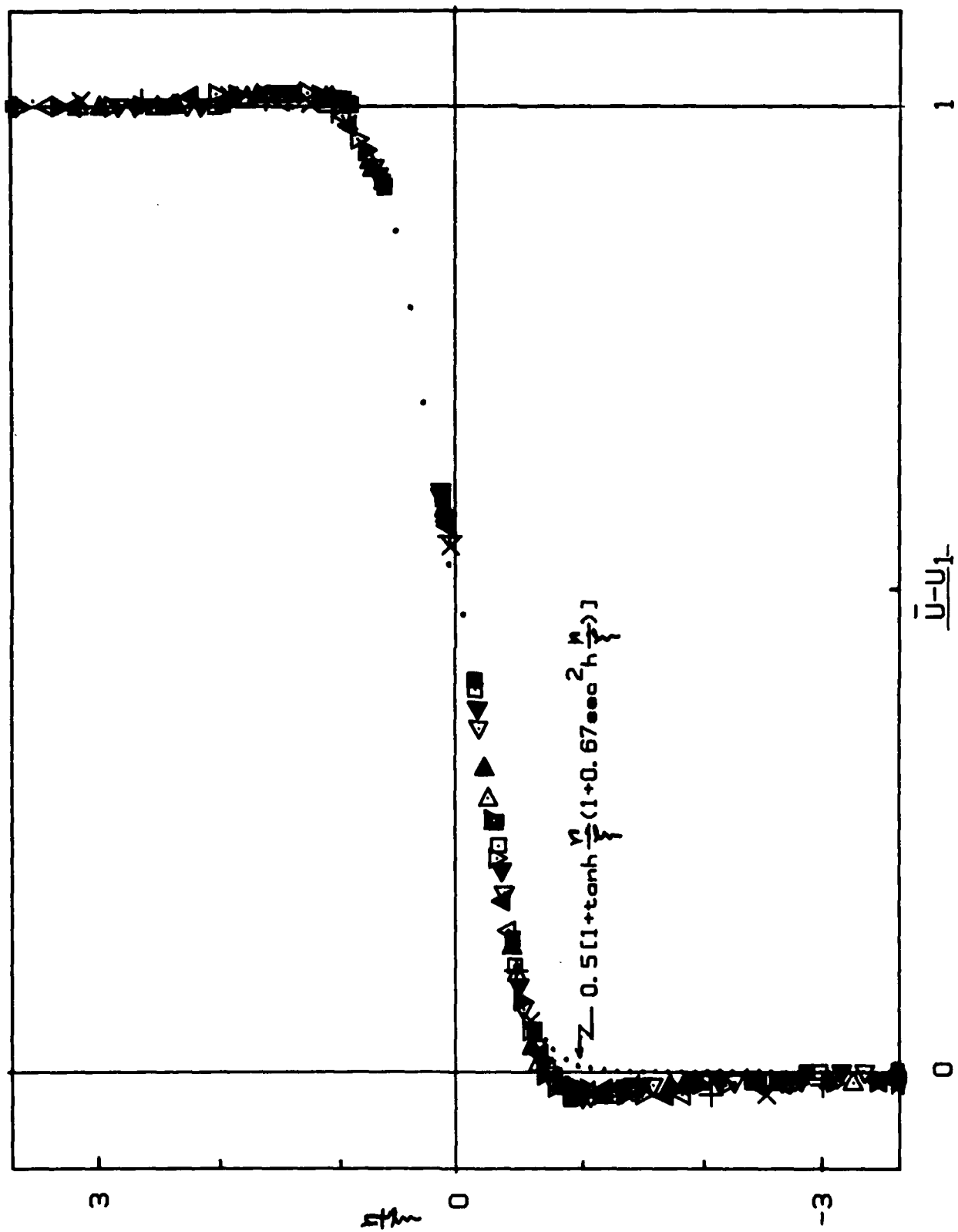
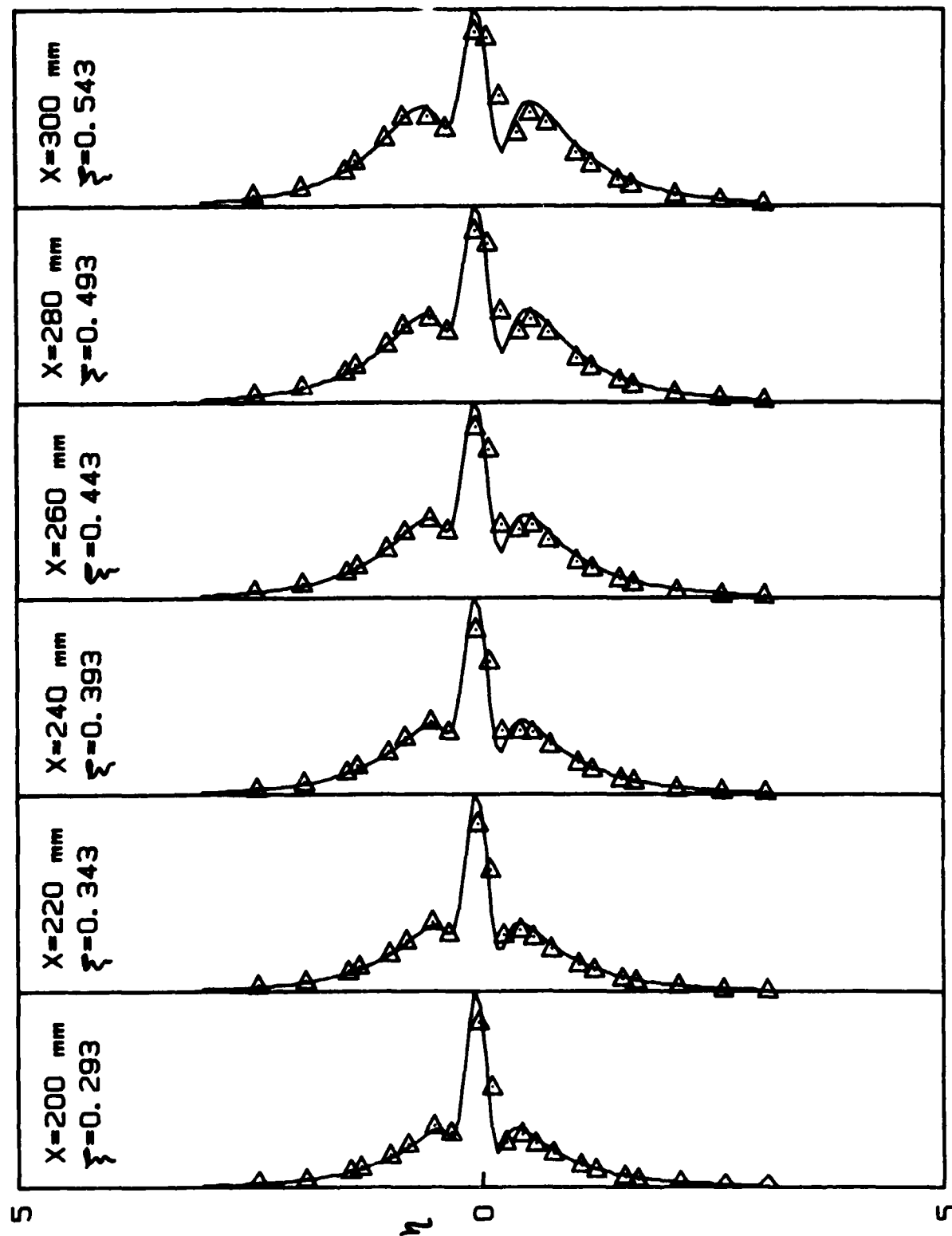
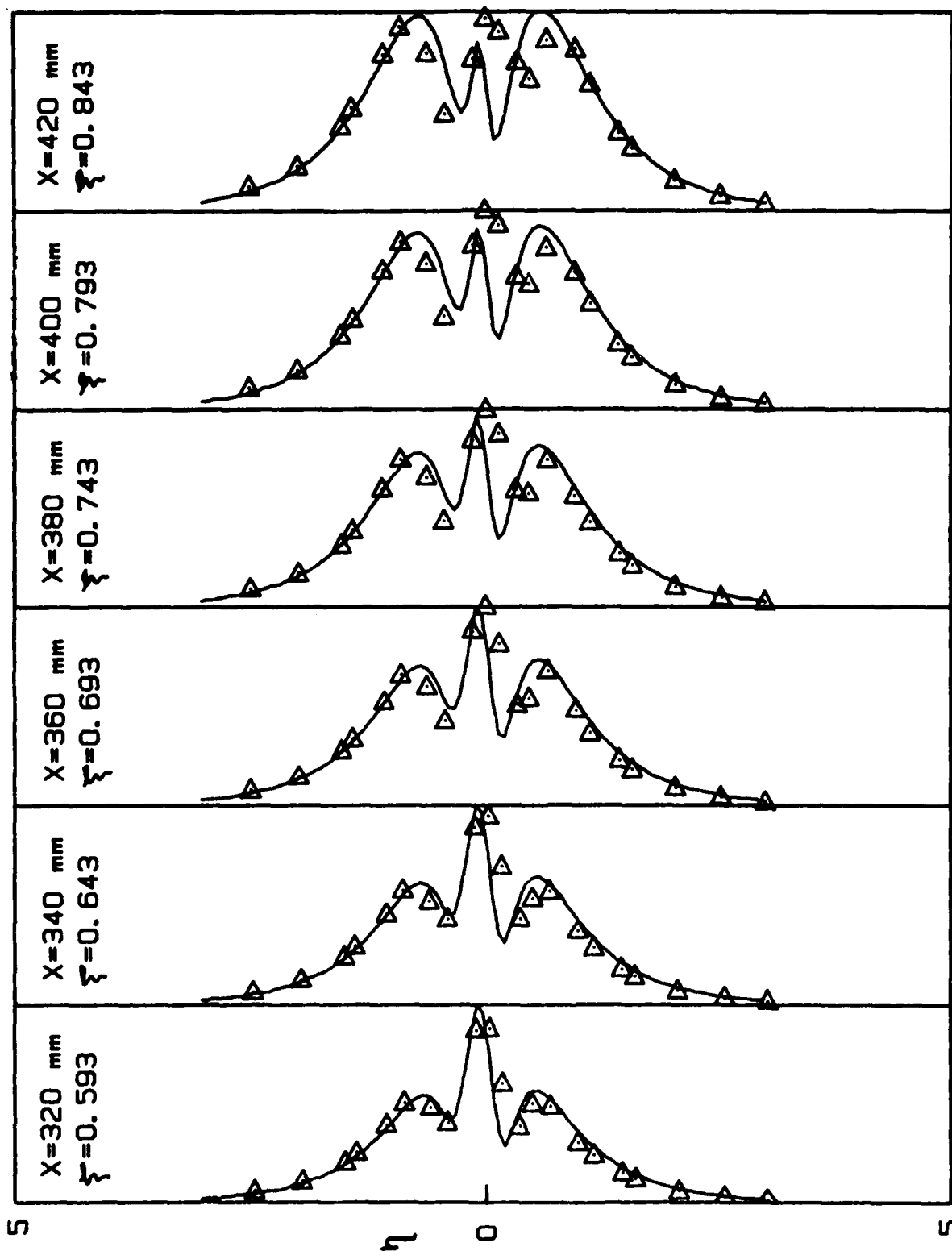


Fig. 6.1



NORMALIZED AMPLITUDES OF U

Fig. 6.2(a)



NORMALIZED AMPLITUDES OF U

Fig. 6.2(b)

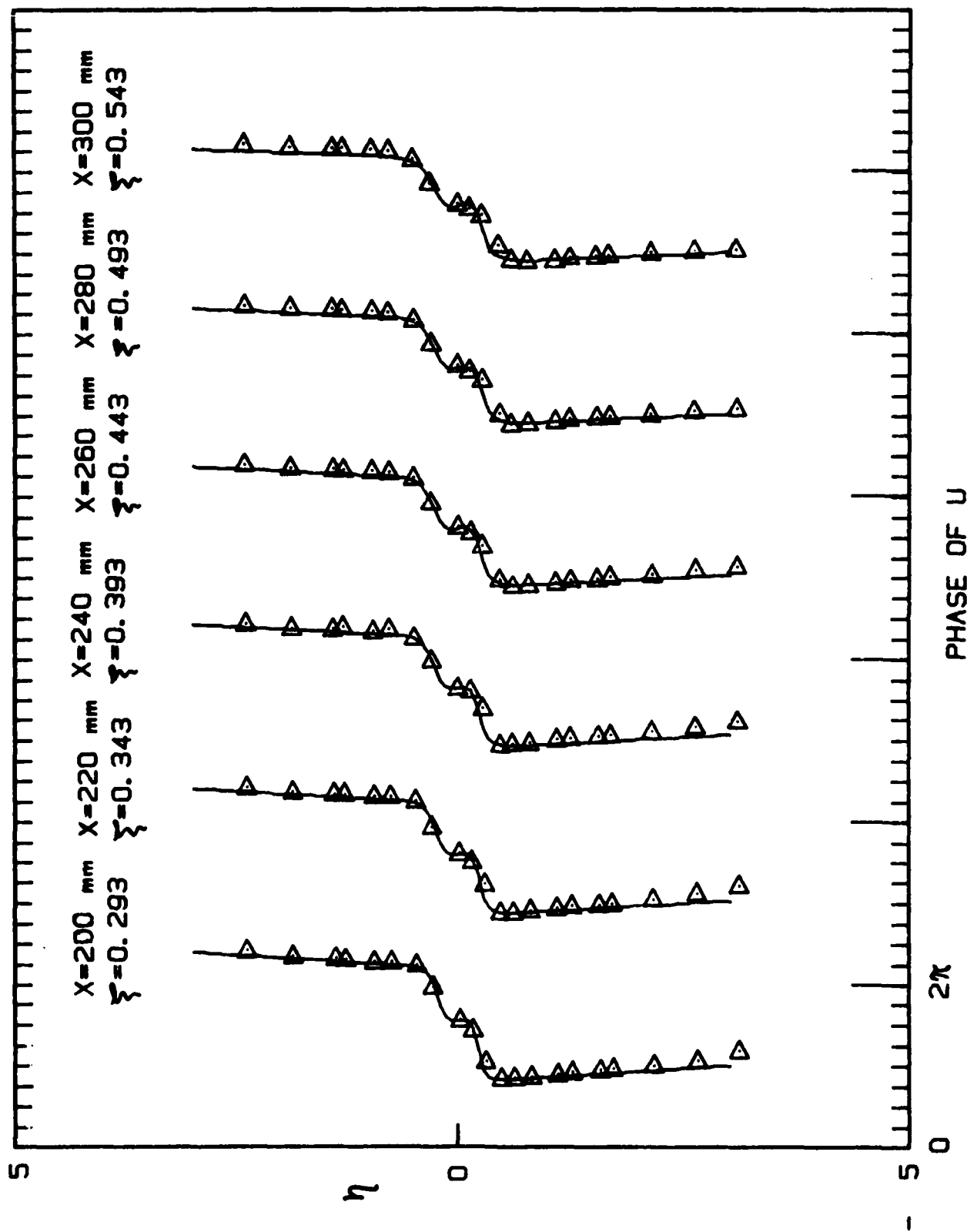


Fig. 6.3(a)

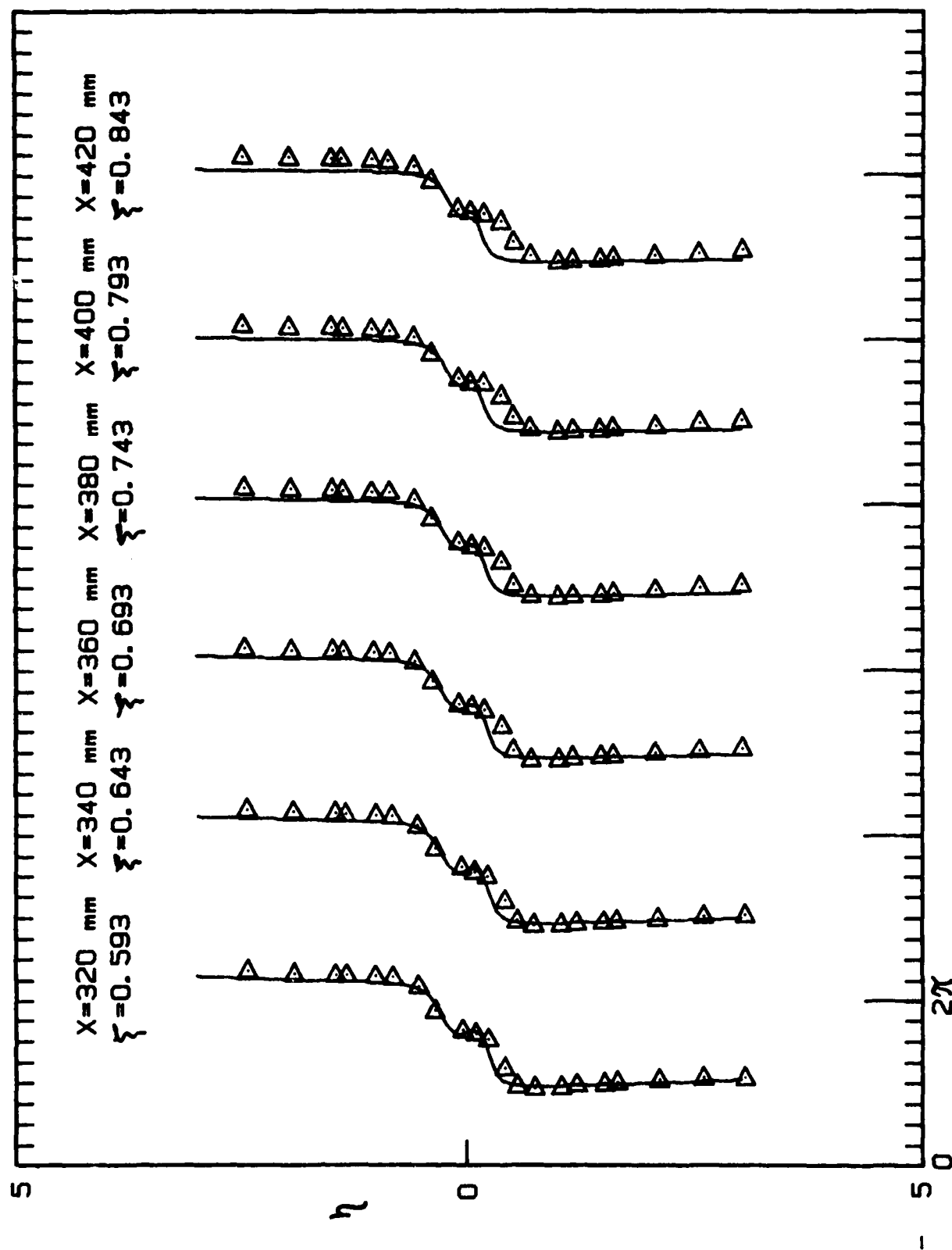
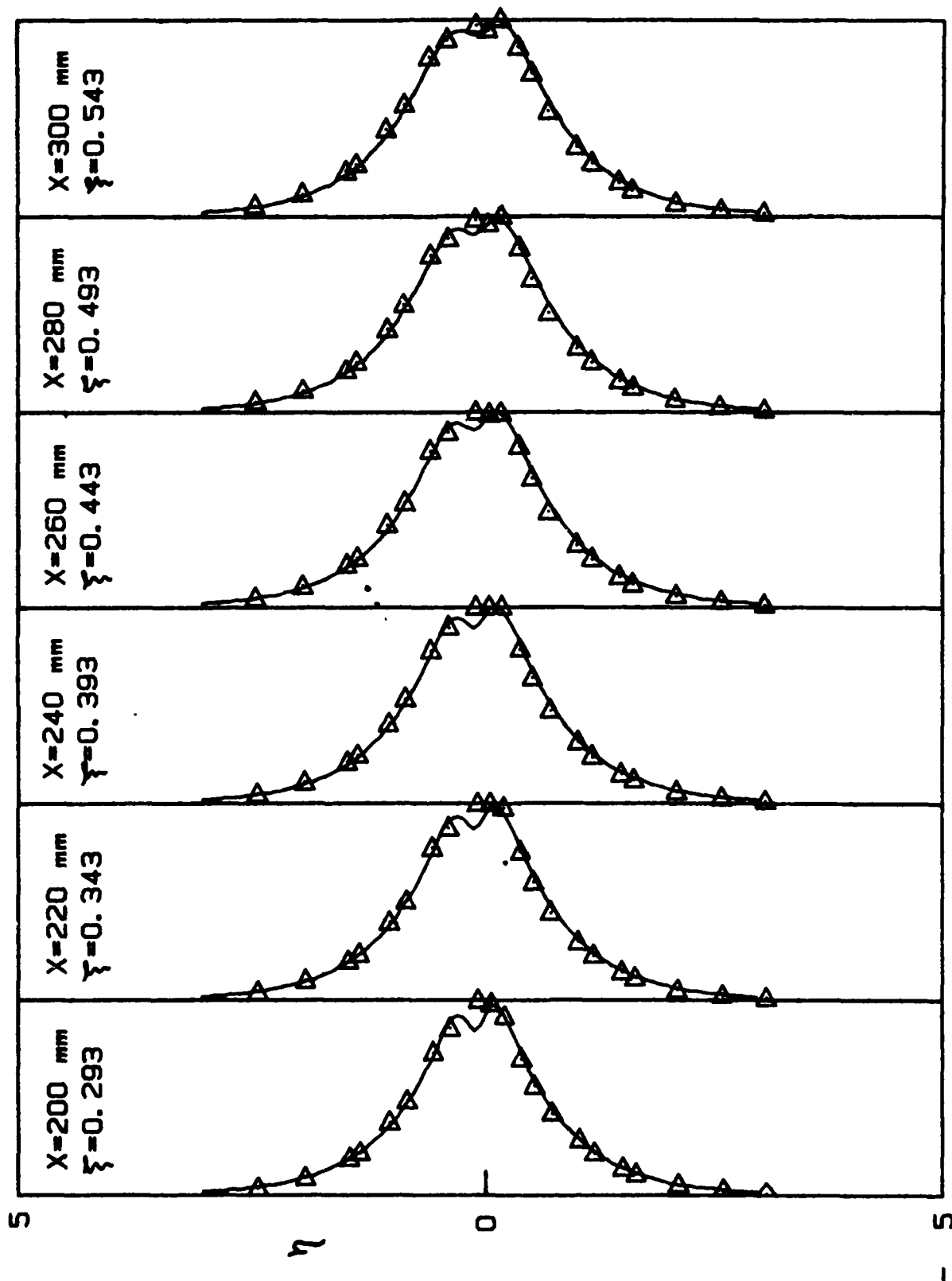
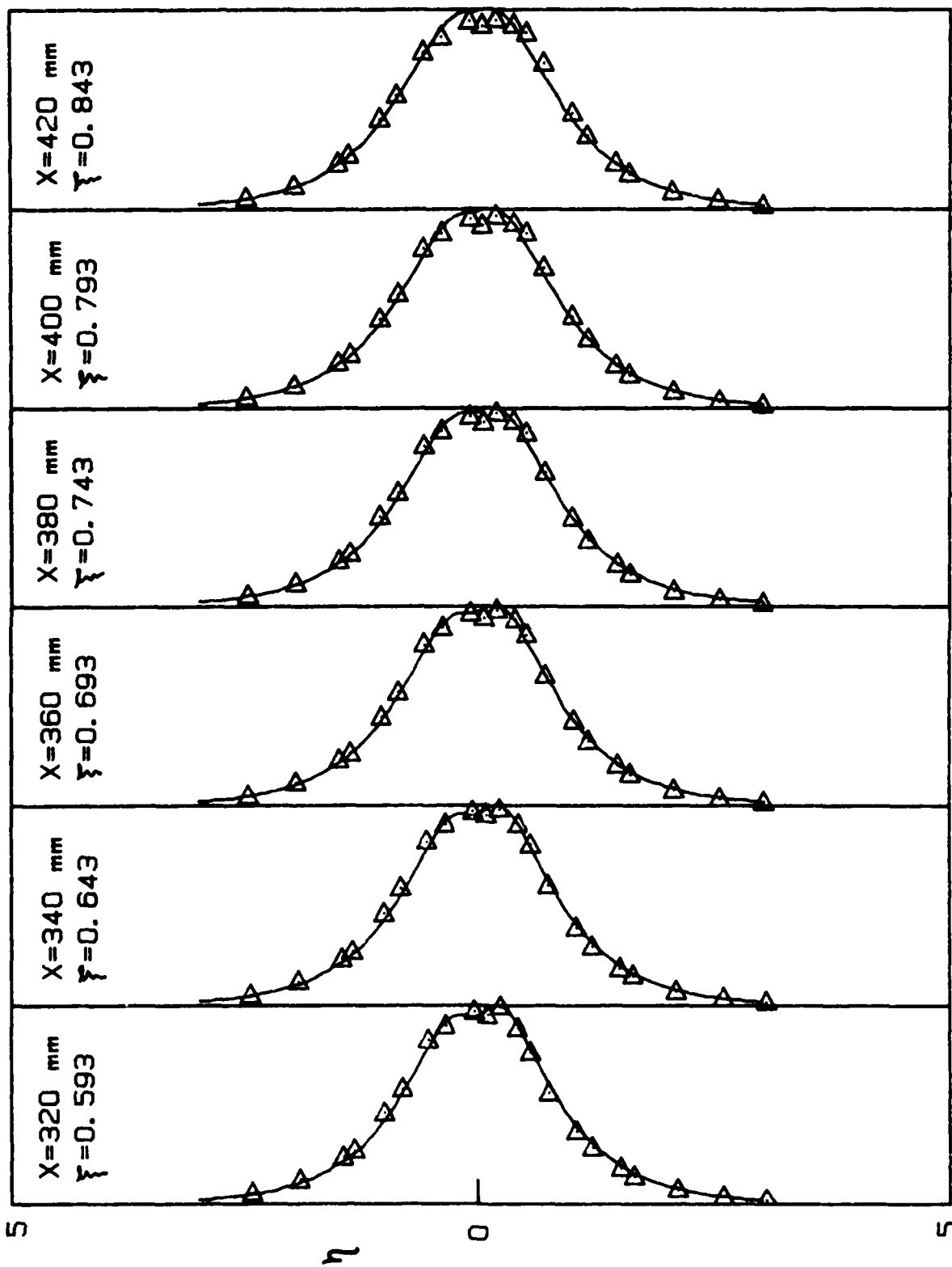


Fig. 6.3(b)



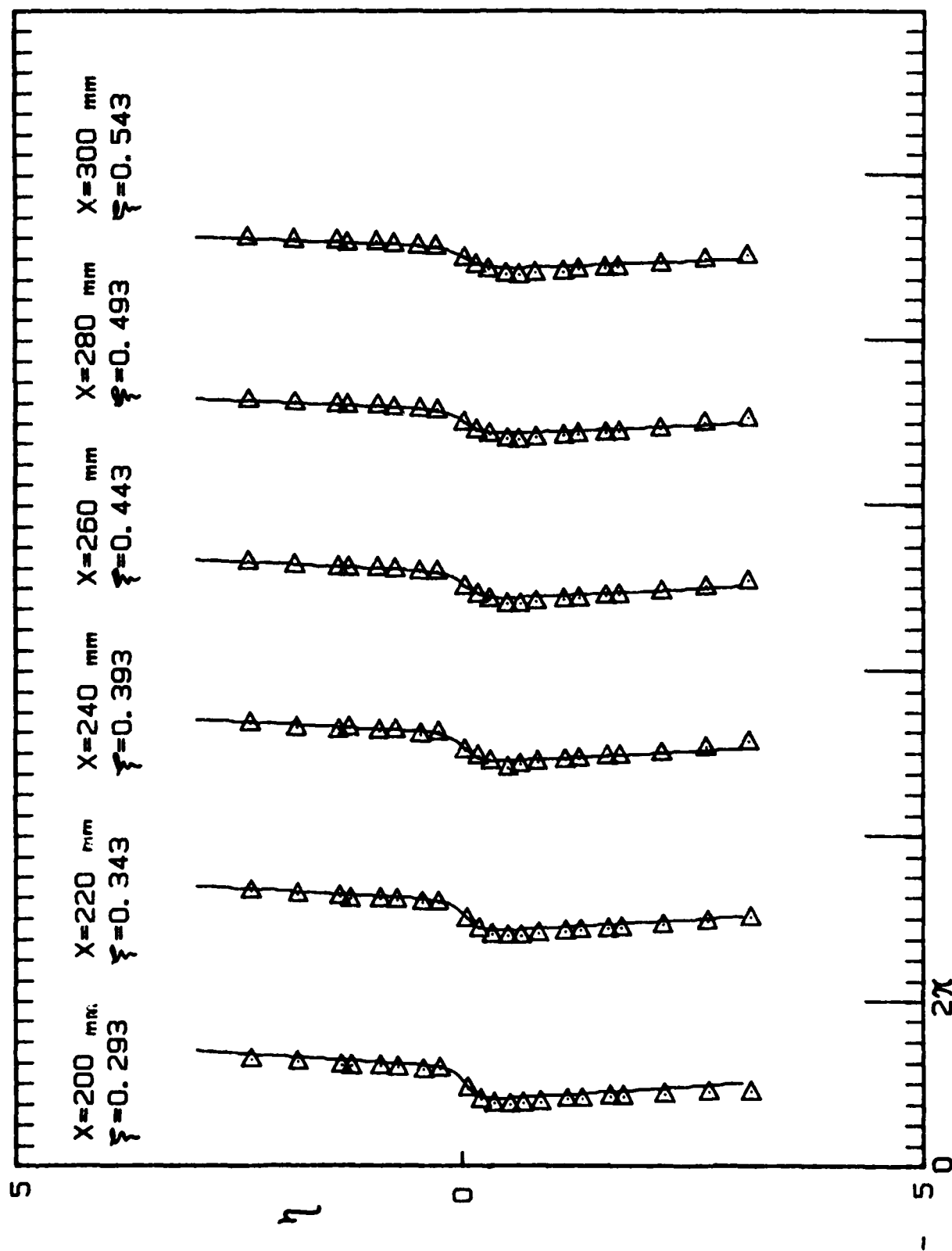
NORMALIZED AMPLITUDES OF V

Fig. 6.4(a)



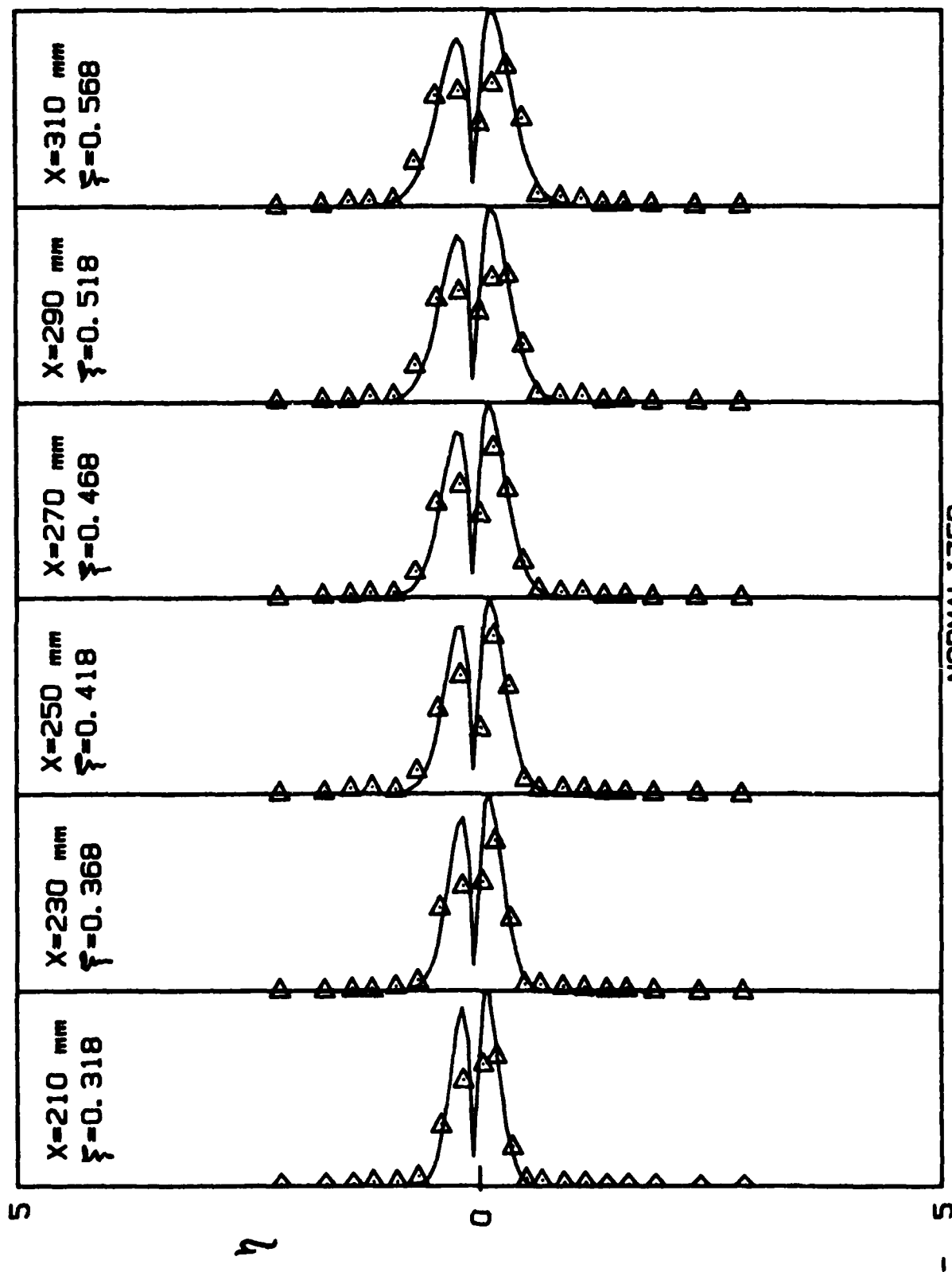
NORMALIZED AMPLITUDES OF V

Fig. 6.4(b)



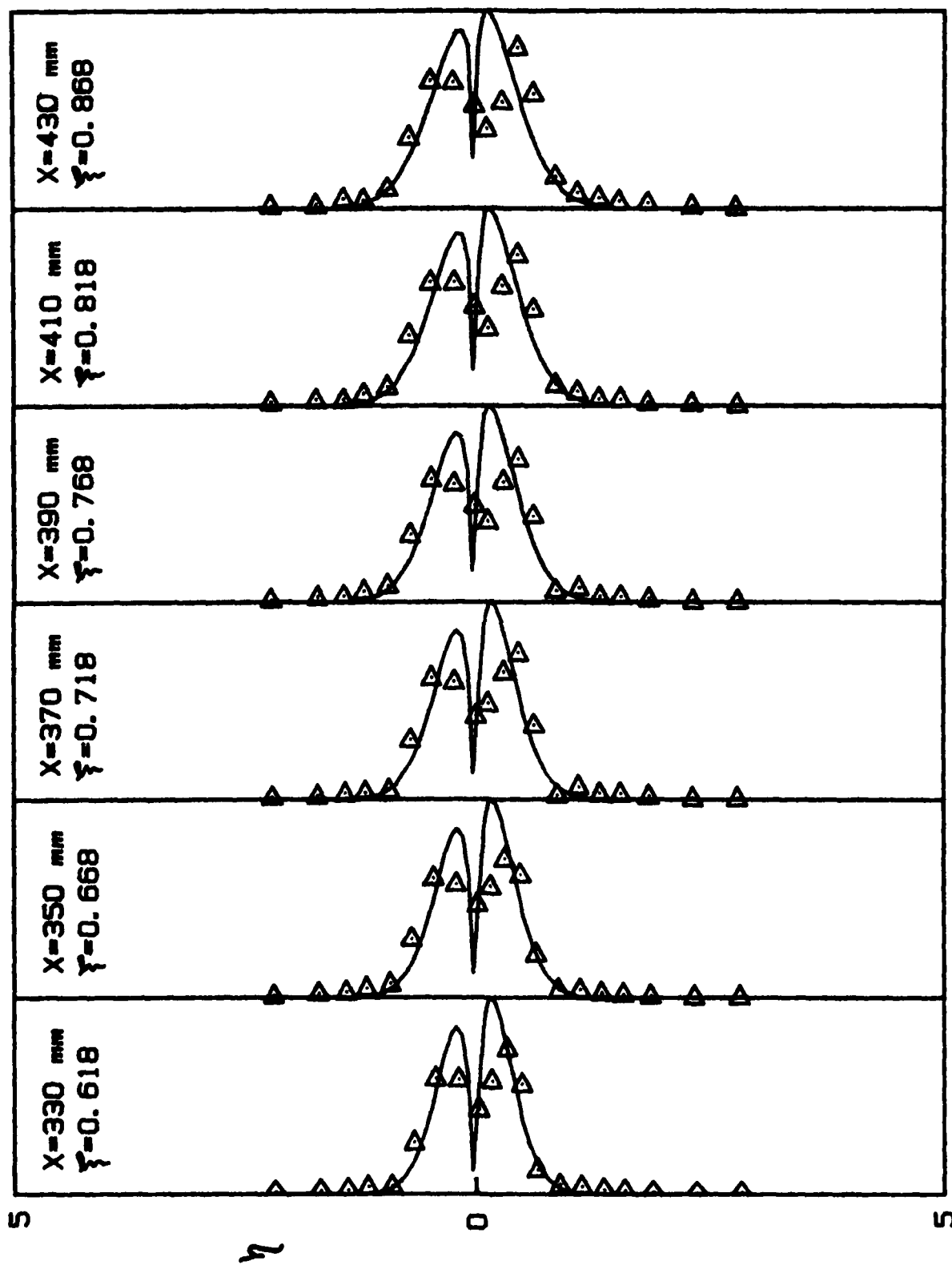
PHASE OF V

Fig. 6.5(a)



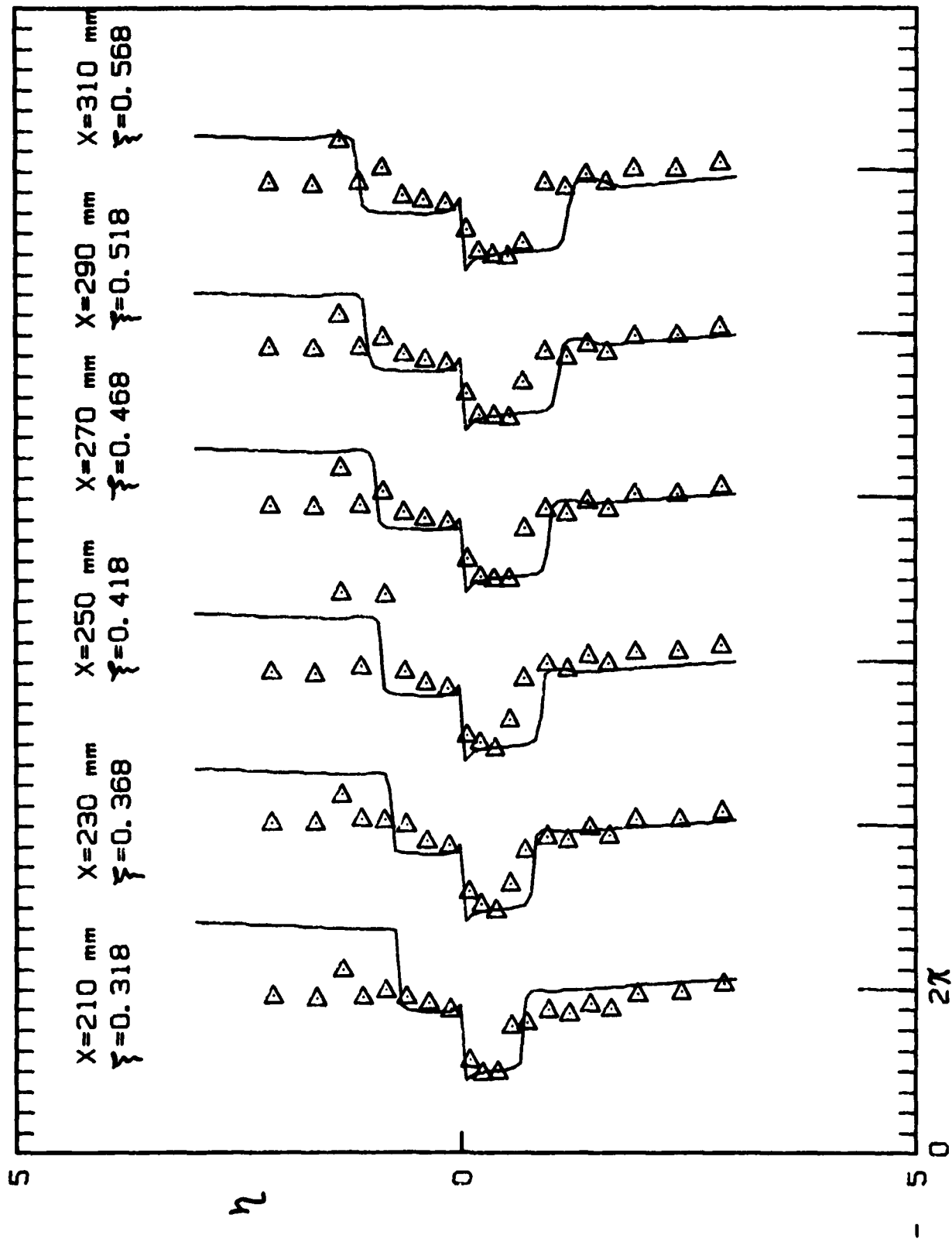
NORMALIZED
AMPLITUDES OF VORTICITY

Fig. 6.6(a)



NORMALIZED
AMPLITUDES OF VORTICITY

Fig. 6.6(b)



PHASE OF VORTICITY

Fig. 6.7(a)

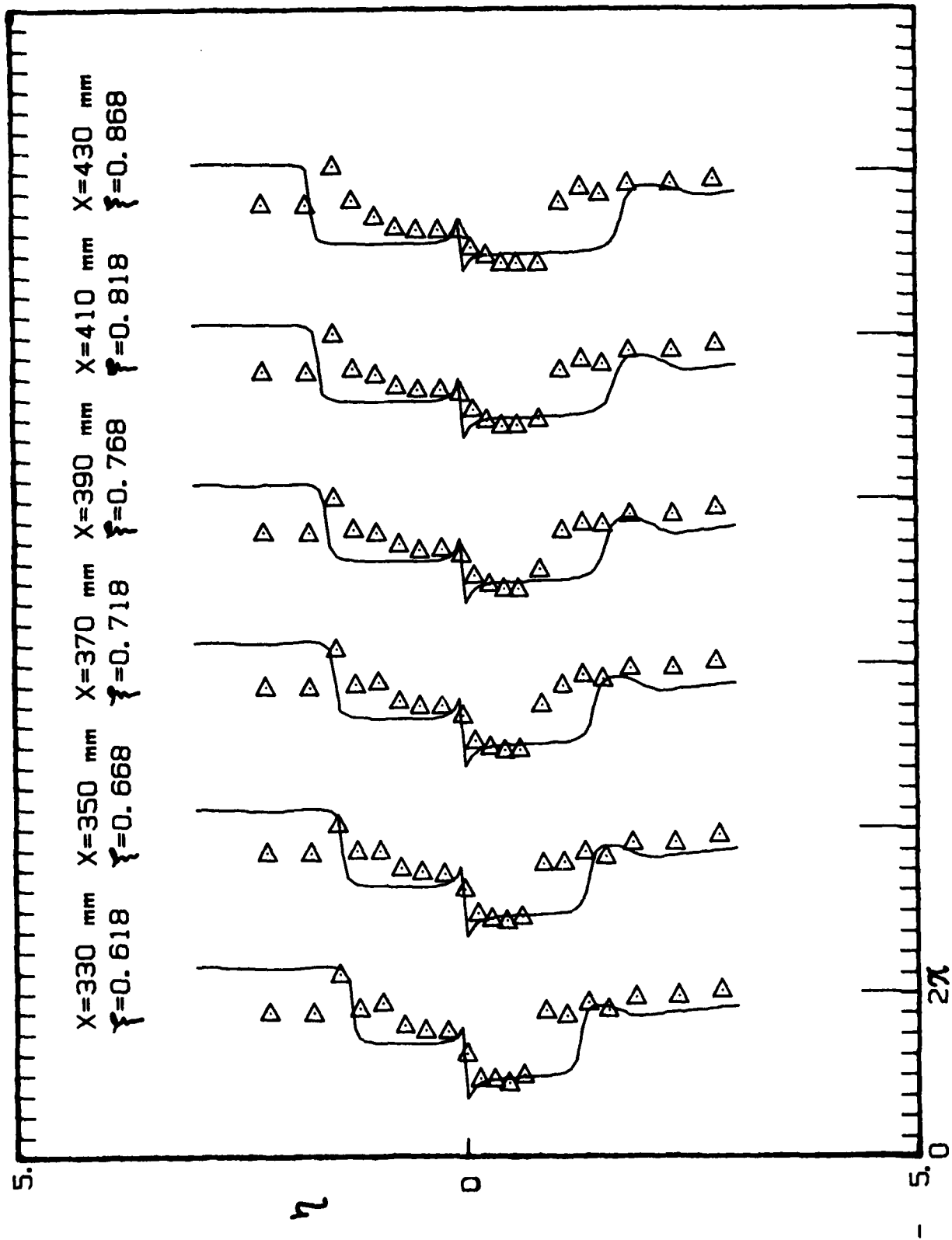
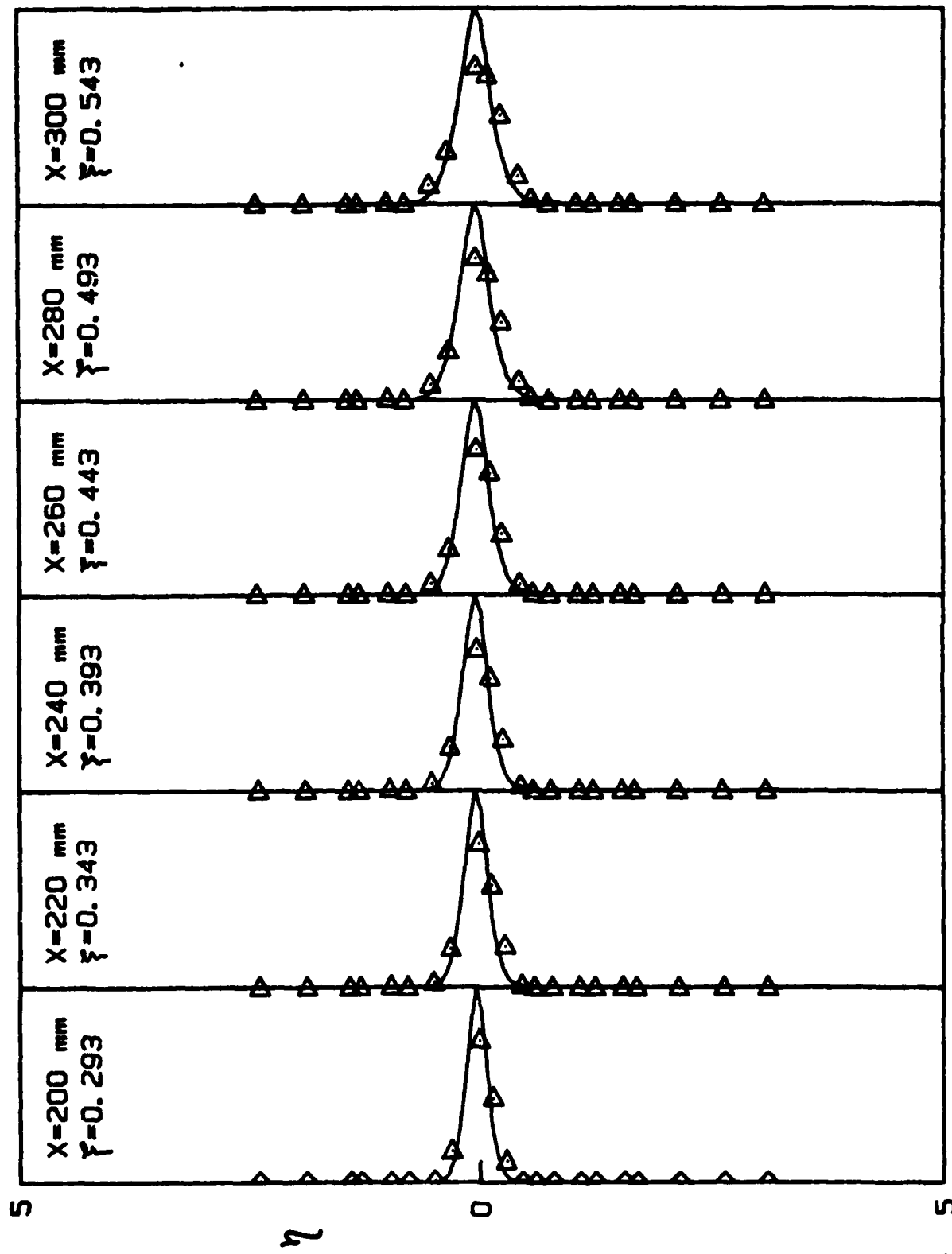
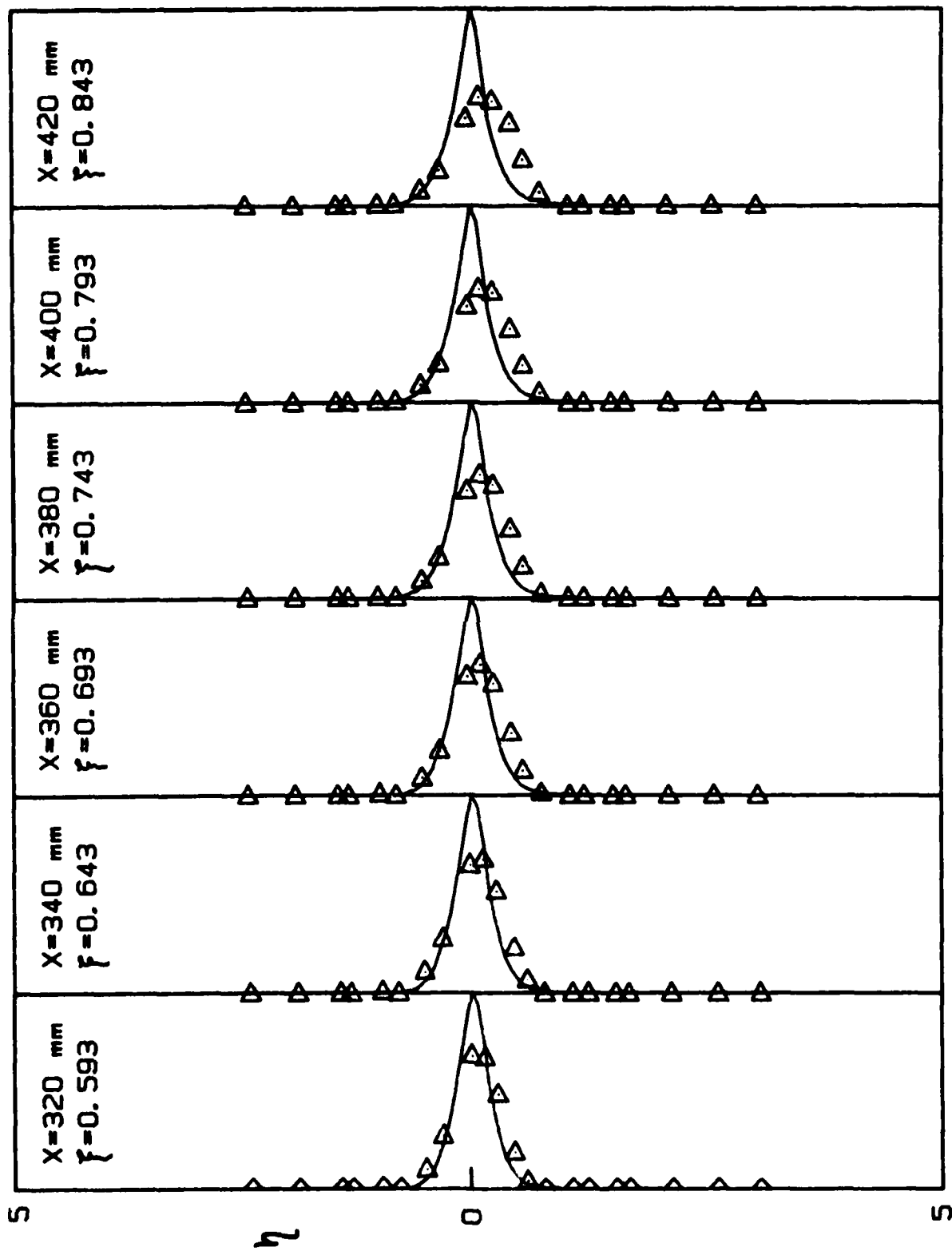


Fig. 6.7 (b)



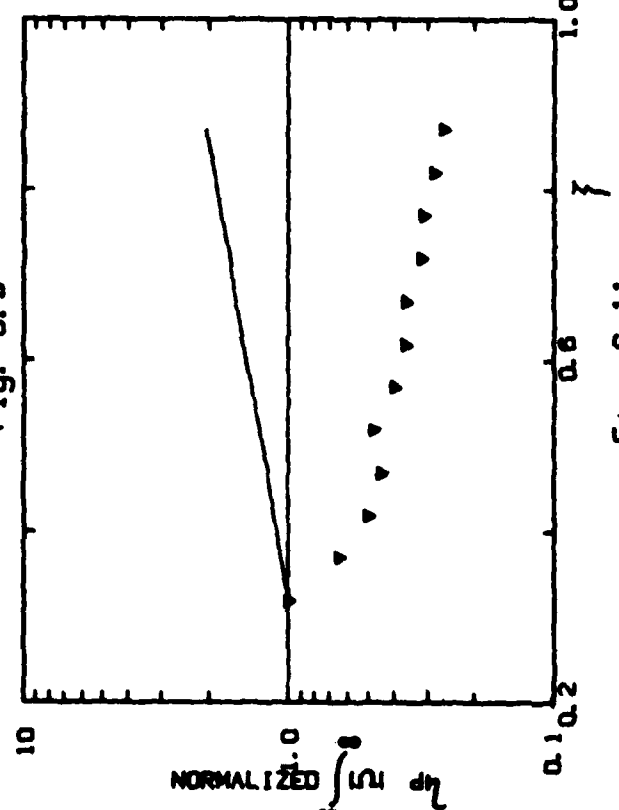
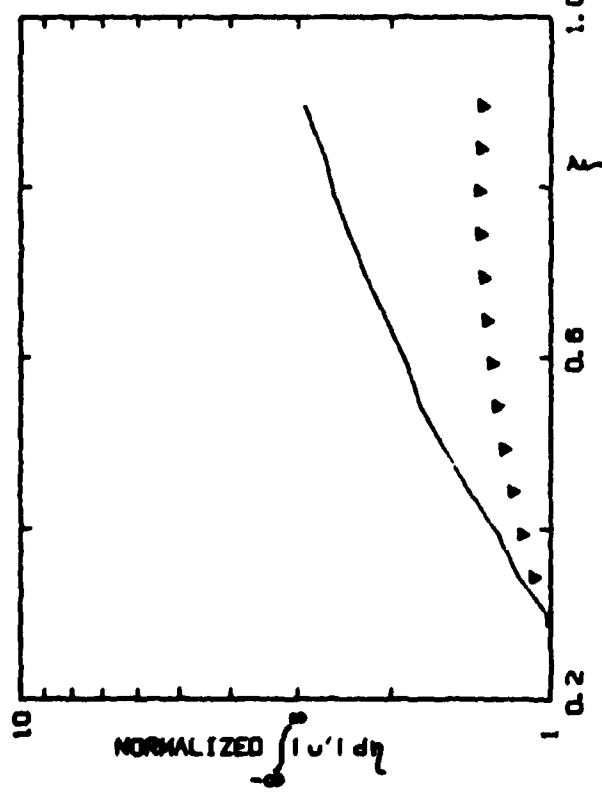
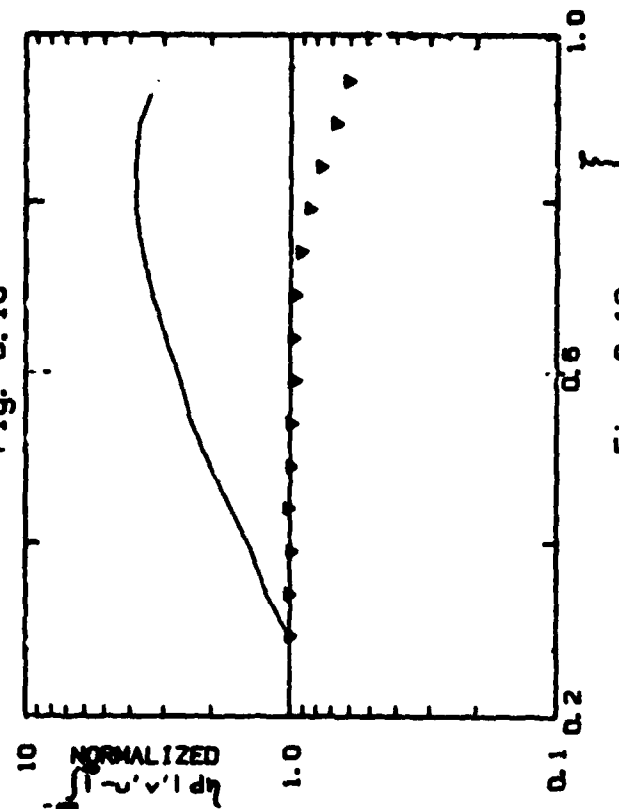
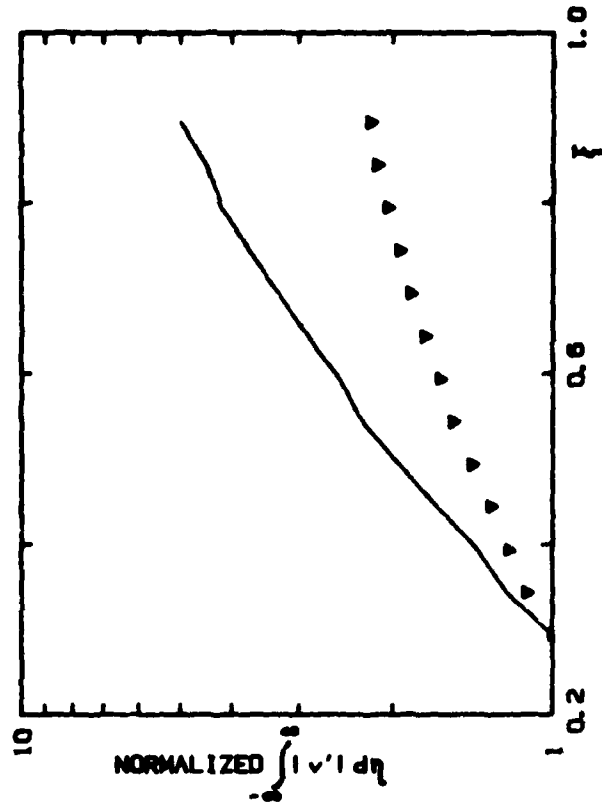
NORMALIZED AMPLITUDES
OF $-U'V'$ PRODUCT

Fig. 6.8(a)



NORMALIZED AMPLITUDES
OF $-U'V'$ PRODUCT

Fig. 6.8(b)



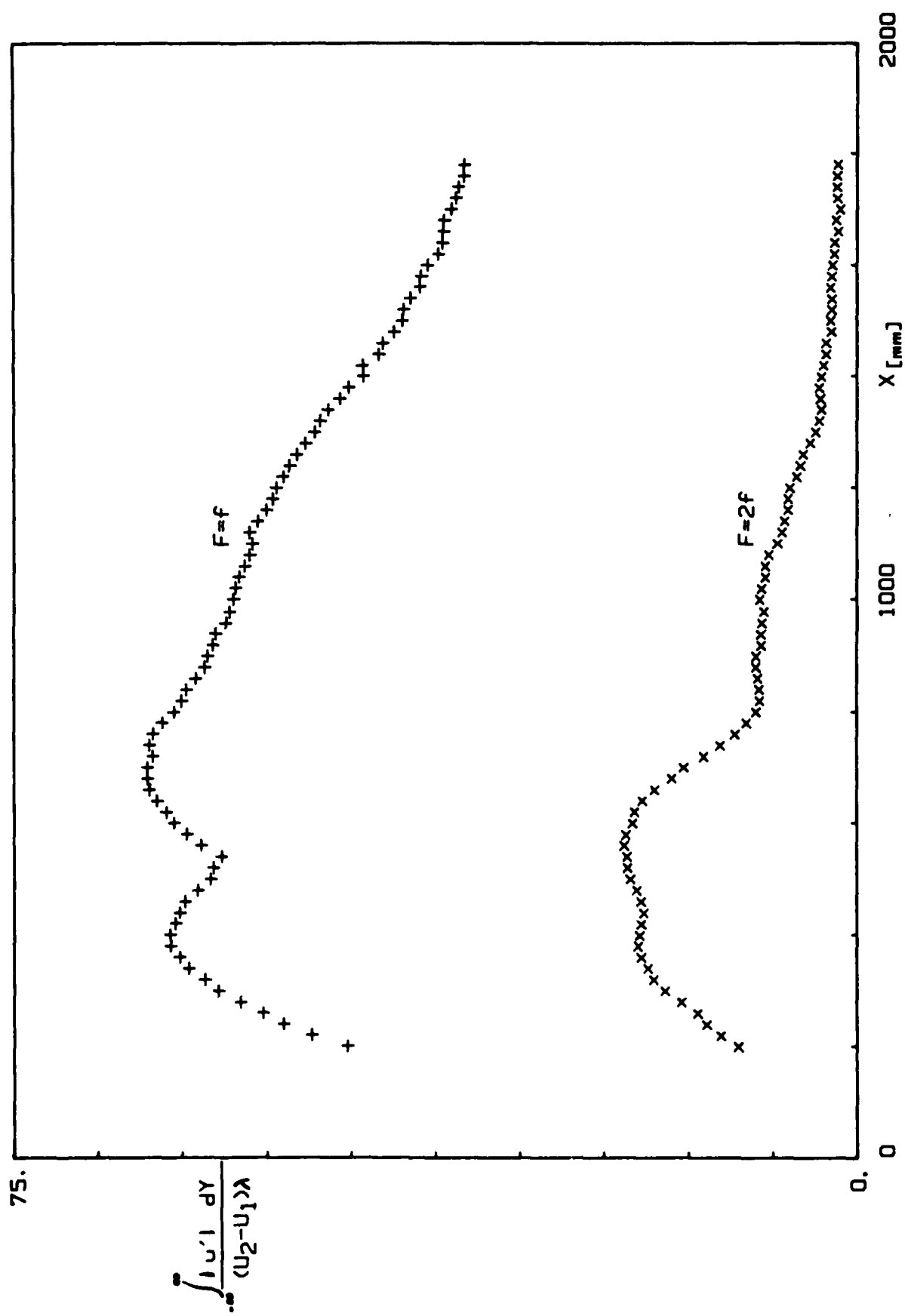


Fig. 6.13

END

5-87

DTIC